NOISE TRANSMISSION ALONG SHOCK-WAVES

by

Prasanna Amur Varadarajan

A dissertation submitted in partial fulfillment
of the requirements for the degree of
Doctor of Philosophy
(Aerospace Engineering)
in The University of Michigan
2011

Doctoral Committee:

Professor Philip L. Roe, Chair
Professor Bram van Leer
Professor Smadar Karni
Assistant Professor Krzysztof J. Fidkowski

To my parents, guru and all my Teachers

ACKNOWLEDGEMENTS

My deepest gratitude to my parents V.Varadarajan and Kumari Varadarajan, for their love and support throughout my life. Their motivation towards education has got me this far to complete my doctoral work. I am extremely thankful to my guru Usha Srinivasan in her conviction towards her work and help me shape as a sensible individual. I owe a lot to my brother, cousins and all my family members for their good wishes and support.

At University of Michigan, I am extremely grateful to my advisor Professor Phil Roe for his guidance throughout my work. I have enjoyed all the conversations I had with him for the past five years. His patience in letting me understand and explore things has helped me a lot. It is the amount of freedom he has given me in learning and making me really think has helped me shape up this work. It is a privilege to be his student. I would like to thank his wife Jacqueline Roe for her motherly affection and care she has shown towards me.

I have learned a lot from the courses offered by Professor van Leer and Professor Karni and I am thankful to them for being in my committee and helping me out with their valuable suggestions for my thesis work. Special thanks to Professor Fidkowski for serving in my committee and for his valuable inputs to my thesis. A note of thanks to all the teachers that I have had in my life who have motivated me to move forward. Special thanks to Dr Del Vecchio[1] of the Electrical department to have supported me with my research in the field of Bio-medical engineering during my Master's degree

[1]currently Associate professor at Department of Mechanical Engineering, MIT

as well in-between during my doctoral work. I would like to thank my undergraduate advisor Dr. Abdusamad Salih [2] at NIT, Trichy, India whose teaching has been a big motivation for me to continue my study in the subject of fluid dynamics.

I am thankful to Dr Sergio Pirozzoli of C.F.P.R group, Italy for sharing their DNS data with us and Dr Farhad Jaberi's group from Michigan state University for confirming and validating the results of the numerical Euler computations performed in this work.

In Michigan over the stay of five years I have acquired a number of wonderful friends whose company I would cherish for a long time. Many thanks to them and to my colleagues Daniel Zaide and Tim Eymann for their support. All my friends have celebrated the success of my doctoral degree as their own. I am greatly indebted to them all.

Finally, great appreciation to the Department of Aerospace Engineering, University of Michigan, CRASH and MACCAS for providing the financial support, without which this work would have been not possible.

[2]currently Assistant professor at Department of Aerospace Engineering, IIST, India

TABLE OF CONTENTS

LIST OF FIGURES

Figure

LIST OF APPENDICES

Appendix

LIST OF ABBREVIATIONS

SBLI Shock Boundary Layer Interaction

GSD Geometrical shock dynamics

C-E-C Compression-Expansion-Compression

E-C-E Expansion-Compression-Expansion

DNS Direct Numerical Simulation

rms root mean square

IVP Initial Value Problem

ABSTRACT

Noise Transmission along shock waves

by

Prasanna Amur Varadarajan

Chair: Philip L. Roe

Shocks at the inlet of scramjet engines are subject to perturbations from their interaction with turbulent boundary layer. DNS results for this interaction indicate the presence of discrete vortices that interact with the shock at its foot. These studies reveal that the vortices cause oscillations of the shock. In this work we examine the propagation of disturbances along a stationary oblique shock following interaction with a two-dimensional vortex. We study the decay of disturbances along a normal shock as measured from Euler computations and compare these with the predictions of Geometrical Shock Dynamics(GSD) for long range propagation. We have incorporated two improvements into the GSD model to tackle the shock-vortex interaction problem. The wave structure of the disturbance resembles N waves, the decay of which follows a power law profile. An extension of the GSD model to predict shock surface propagation in 3-D flows is presented along with the numerical implementation.

CHAPTER I

Background and Motivation

1.1 Introduction

Shock-waves are non-linear wavefronts that exist in supersonic flows. They are characterized by discontinuity in the flow variables. Geometrically in 1-D space, shocks represent point discontinuities whereas they are curves and surfaces in 2-D and 3-D space respectively. The propagation of a shock is non linear and depends on the flow variables upstream and downstream to it. In 2-D and 3-D flows the propagating shock fronts can be perturbed either from the geometry or from the disturbances in the fluid flow. Examples of the shock fronts being perturbed by geometry are the reflection of a planar shock wave from a corrugated surface and a parabolic surface(shock-wave Lithotripsy) or the diffraction of shock fronts over cylindrical and conical surfaces. Examples where the shock wave is perturbed from the disturbances in the flow field are because of their interaction with vortices or bubbles. Shock wave boundary layer interaction(SBLI) occurring for example in the inlets of Scram-jet engines is such flow field where the shock is subjected to perturbations from the vortical structures of the turbulent boundary layer. The perturbations of either kind will give disturbances along the shock which may travel larger distances.

The basic motivation for this work comes from the idea of attempting to study "shock trains"(figure 1.1). These are shocks that are repeatedly reflected between

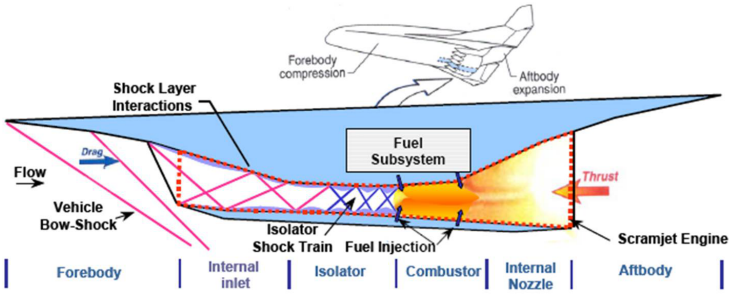

Figure 1.1: Representative Scramjet Engine

the walls of certain hypersonic propulsion inlets, and are subject to unexplained instabilities. We wish to explore the hypothesis that a turbulent boundary layer on one wall can transmit strong intermittencies to the opposite wall via the shockwave. To embark on the study we use

- the theory of geometrical shock dynamics(GSD) which helps in predicting shock propagation over large distances
- the study of shock-vortex interaction to understand the nature of disturbances that propagate along the shock

Brief details on each of them are being given below.

1.2 Geometrical shock dynamics(GSD)

The theory of GSD was formulated by Whitham [37] to study the propagation of shock-fronts moving into a stationary medium in 2-D flows without having to compute the flow field behind it. Borrowed from the idea of propagation of wavefronts from optics, shock waves can be viewed as wavefronts that propagate along their normals called as "rays" with the speed of propagation depending on the amplitude of the wave. The difference from optics is that shocks are non linear wavefronts

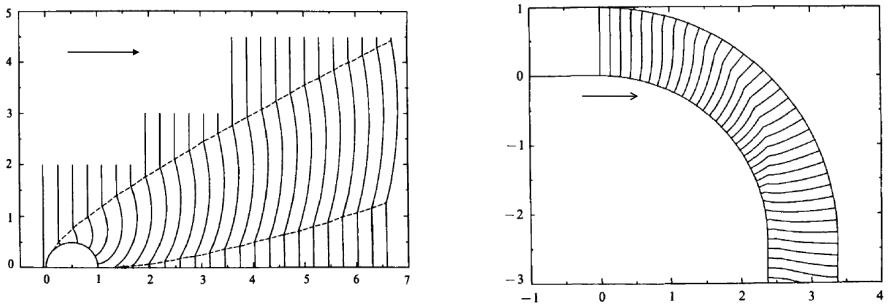

(a) Diffraction of a plane shock by a cylinder

(b) Shock propagation in a channel

Figure 1.2: GSD Shock propagation

that develop kinks along themselves as they propagate. The success of the theory lies in its ability to predict qualitatively shock wave propagation along the curved channels(figure1.2), propagation of shocks reflected from parabolic surfaces [34] and propagation of sinusoidal weak shocks [19] over large distances. Whitham extended the theory to capture shock-surfaces in 3-D flows[38] and to shock fronts propagating into a uniformly moving medium in [39].

Mathematically the propagation of shock-front gets reduced to a 2×2 system of nonlinear conservation laws governing an intrinsic representation of the shockwave, together with a pair of ordinary differential equations that map this solution into the physical plane. The propagation of a shock thus in 2-D space reduces to the solution of a 1-D problem and in 3-D space to a 2-D problem. The reduction in computer resources is enormous, and this allows problems to be attacked that would be otherwise infeasible. For instance in the study of shock-vortex interaction which forms the major part of this work, there is a reduction of 3 orders of magnitude in the computational time using the theory of of GSD as compared with the Euler equation computation. But before implementing GSD to study shock trains, it was found beneficial and necessary to reformulate the basic ideas of GSD.

1.3 Shock Boundary Layer Interaction(SBLI)

Shock Boundary layer interaction problem has been a fascinating subject of study for over 60 years because of their impact on vehicle performance in high speed flights. It is a perfect blend of a problem with the coupling of non linear phenomenon coming from both the presence of the shock and the compressible turbulent boundary layer. A general set up of the flow field for such an interaction is in the entry of a Scram-jet engine where the oblique shock gets reflected from the bottom surface of the engine inlet(figure 1.1). A good deal of experimentation and computational studies have been carried out to study the amplification of the turbulent boundary layer once it interacts with the shock foot and its control, the unsteadiness in the position of the foot of the λ shock and pulsating effects of the separation bubble near the foot of the λ shock. The downstream turbulence and the unsteady nature of the shock structure form the important aspects of study in SBLI. More comprehensive details about the progress and the development in SBLI in the last century can be found in [9].

DNS of an oblique shock interaction has been carried out by Pirozolli and Grasso [22] and a shock generated by a compression ramp has been studied by Wu and Martin [40] showing shock oscillations (refer figure 1.3). Simulations carried out by Pirazolli and Grasso [22] show that the boundary layer separation is highly unsteady. The separation point moves back and forth shedding vortices that interact with the shock(refer figure 1.4). The foot of the λ shock sometimes disappears and the reflected shock is changes in location and strength. Experiments consistent with this result are reported by Ganapathisubramani et. al.[3]. The description of the numerical DNS database for the reflected shock interaction is given by Pirozzoli and Bernardini [23].

In this study we would like to focus our attention on studying the change in the shock structure using the theory of GSD. The shock structure as observed from the simulations of Pirozolli and Grasso [22] show that perturbations coming from

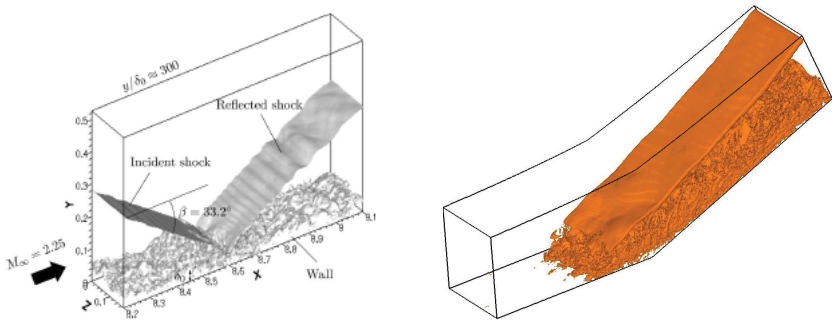

(a) Results of Pirozolli and Grasso [22] of a reflected oblique shock

(b) Results of Wu and Martin [40] along a compression ramp

Figure 1.3: Shock oscillations shown from DNS studies

the discrete vortices along the boundary layer get transferred along the reflected shock. The oscillations shown in figure 1.3(a) seem to decay in amplitude as well as frequency as we go along the shock. This could be because of the computational effects, appearing from the lower spatial resolution along the free stream away from the boundary layer. However, both effects are consistent with our computations. It seems that though the boundary layer is three-dimensional the perturbations on the shock is two-dimensional. The parametric details and animation of shock oscillations are given for a flow over a compression ramp by Wu and Martin in [40] in the online version of the paper. The reason for the unsteadiness of the shock structure and the separation bubble is still not clear. There are correlations showing the dependance of low frequency shock oscillations with respect to the dynamics of the separation bubble downstream[30], though some of the experiments support the claim of shock oscillations related to the turbulent structures in the incoming boundary layer. Possibly both are correct there is a tendency for perturbations in the shock reflection case to be transverse to the flow, but parallel to the flow in the ramp compression case. Recent proposal from Wu and Martin [40] suggest that the shock motions could be related to some feedback loop between the separation bubble, the separated shear layer and the separation bubble.

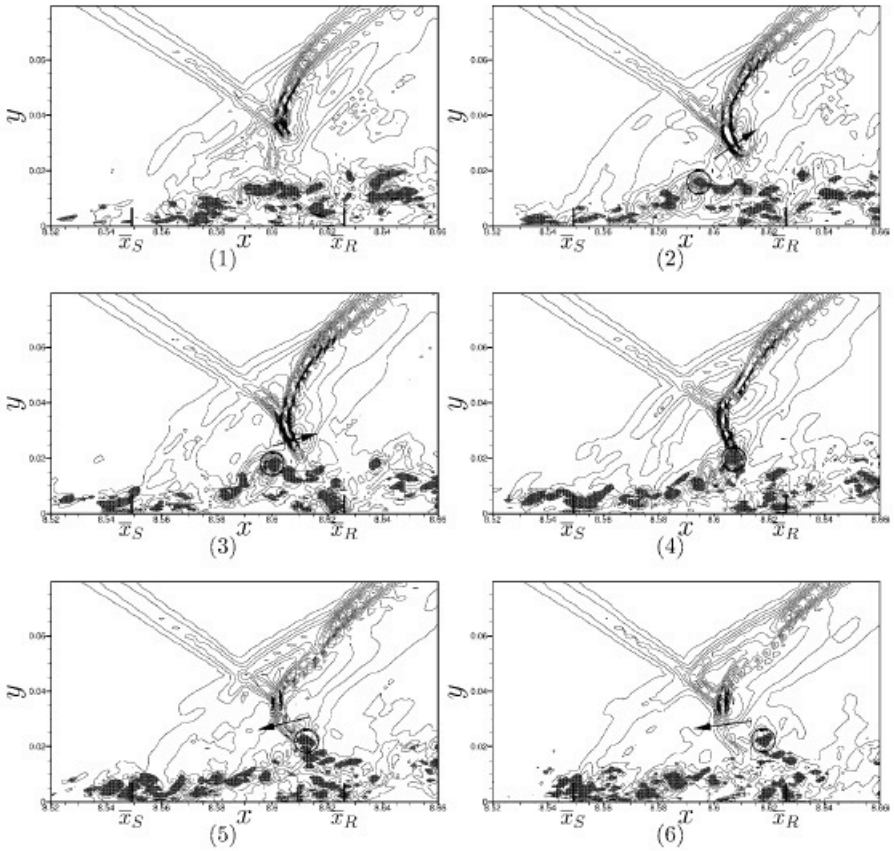

Figure 1.4: DNS results of Pirozolli and Grasso [22] showing vortices interacting with the pulsating shock at different time intervals

In the shock-trains at the inlets of scramjet engines the turbulent boundary layer along the side walls will also play a dominant role in sending disturbances along the shock but DNS computation of the full complication is not feasible.

To understand the shock oscillations in the reflection case a first step would be to understand the nature of disturbances which would propagate along the shock because of shock-vortex interaction. Both experimental and numerical investigations of 2-D vortex with a normal shock have been carried out to understand the acoustic field generated behind the shock once the vortex passes through it and the changes in vortex properties. Theoretical studies have been carried out by Ribner [27] and Ting [33]. Ribner [27] shows the decay of pressure disturbance from the vortex after interaction to follow t^{-1}. Numerical studies of shock vortex interaction using 2D - Euler computations has been carried out by Grasso and Pirozolli [13] and Ellzey and Henneke [10] to characterize the shock and vortex deformations and relating to sound generation. Finite difference computation of Navier-Stokes equations in a similar set up has been done by Inoue and Hattori [15]. Numerical study of shock-vortex interaction using 3-D Euler equations has been carried out by [1] to study the breakdown of vortices while interacting with an oblique shock.

The 2-D shock upon the interaction with the vortex undergoes both diffraction and reflection consisting of either a regular reflection or Mach reflection depending on the shock and vortex strengths, both of which are observed in experimental and numerical studies. The cases of shock deformation with both regular reflection and Mach reflection is enlisted in their works. These perturbation along the shock close to the point of interaction has been studied thoroughly but the long range propagation which forms the focus of this work.

1.4 Thesis outline

Before embarking on the outline of the thesis, our major contribution from this work is listed as follows

- We have presented the novel idea of implementing the theory of GSD to study the oscillations along the shock with its interaction with the turbulent boundary layer
- Have reformulated the theory of GSD in a simplified manner retaining its geometrical nature and its extension for the shock propagation into a uniformly propagating medium in 2-D flows
- Have identified the nature of waves that propagate along the shock upon its interaction with a vortex in 2-D flows using both GSD as well as Euler computations
- Have extended the theory of GSD to capture shock propagation in 3-D flows with the numerical implementation

In chapter II we introduce the formulation of GSD to 2-D shocks in a detailed manner. We will begin with our simple geometrical interpretation of the governing equations along with a Godunov type solver for numerically solving the system of equations. A simpler version retaining the geometrical formulation is proposed for the case of shock propagation into a moving medium. This is computationally efficient, and then shock-vortex interaction problem is modeled.

To validate our modeling of GSD and to study in greater detail the nature of shock-vortex interaction, while still emphasizing the dynamics along the shock, some numerical experiments of 2-D shock-vortex interaction using the Euler equations are performed and discussed in chapter III. Although the interaction between shocks and vortices in SBLI involves oblique shocks we study almost exclusively normal

shocks. This is because the interaction of a single vortex with an oblique shock is easily derived from the solution of a normal shock by a simple translation(section 2.8.1). The experiments are carried out for a set of shock and vortex strengths. The characteristic nature of wave disturbances and their decay rates are measured and analyzed.

Having validated the model of GSD for shock-vortex interaction in 2-D flows and from its success to predict the complex physics, the 3-D extension of GSD is formulated in chapter IV. A numerical scheme is proposed and its implementation is discussed for a couple of 3-D test cases.

Chapter V will draw conclusion to the thesis briefing the outcome of the shock-vortex studies and will discuss the possible extension of the current work especially to the numerical aspects of 3-D GSD model and in the study of shock trains.

CHAPTER II

GSD - Shock propagation in 2D

2.1 Brief History of Geometrical shock dynamics(GSD)

The original formulation of GSD was done by Whitham[37] which deals with a shockwave that propagates into a uniform stationary flow in two dimensions. The idea comes from the theory of optics for the propagation of a wavefront along rays which are orthogonal to the fronts and from the study of propagation of a shock down a tube of slowly varying cross sectional area. An initial extension of the shock propagation into a uniformly moving medium was done by Chisnell [8] which was incorrect, a correct formulation was again given by Whitham[39]. The theory is summarized in [36] by Whitham. Comparisons with experimental results by finite difference numerical computations for 2D shocks was done by Henshaw [34]. An extension for describing the shock dynamics in 3D flows was done by Whitham [38]. Schwendenman [31] solved the 3-D equations by a finite difference method similar to that of steady supersonic potential flow. He used the theory to analyze the stability of converging cylindrical and spherical shocks.

Maslov [17] studied the convergence of Whitham's procedure for propagation of a weak shock under isentropic conditions. Prasad[25] derived the geometrical relations of non linear wave propagation in the conservation form known as kinematical conservation laws and when applied to the shock front he follows a similar procedure to

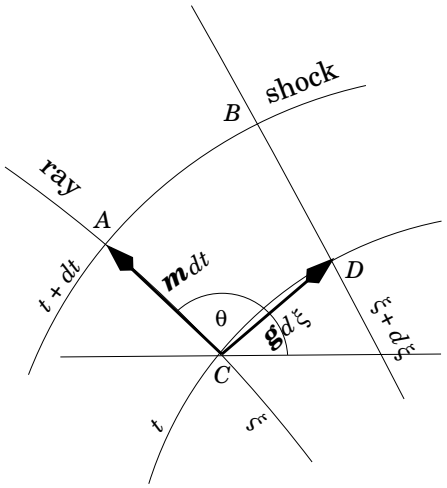

Figure 2.1: Part of the net of shock locations and rays.

that of Maslov. The standard solutions of conservation laws, with simple waves and shock-shock collision along with the jump conditions and interesting interpretations are found in [4]. Best[5, 6] performed a similar analysis to that of Maslov removing the restriction of isentropic flow and extended the theory for studying underwater explosion which produce non-uniform flow conditions behind the shock. The detailed derivation of the geometrical shock dynamic equations and the approximations involved in the area Mach relations are illustrated in the following sections.

2.2 Geometrical shock dynamics(GSD) - Governing equations

Following the procedure of Whitham[37] we employ a computational net in the plane $\mathbf{x} = (x, y)$ consisting of curves $t = const$ which represent successive shock locations, and introduce the set of orthogonal curves which we call "rays". Each ray defines a level line for a function $\xi(x, y)$ and the physical distance between rays $\xi, \xi + d\xi$ along a shock curve is taken to be $g\ d\xi$ where g is a metric. The physical distance between two shock curves $t, t + dt$ along a ray is taken to be $m\ dt$, so that m is the speed with which the shock front propagates normal to itself. If we define

the length and time scales to be in the ratio a_0 with a_0 representing the sound speed in the stationary flow into which the shock is moving, then $m(\xi, t)$ will be the shock propagation Mach number. We define $\theta(\xi, t)$ to be the direction of the shock normal with respect to a fixed coordinate.These are purely geometrical relationships among the quantities defined, and these are variously derived in the cited references.

A brief derivation that extends conveniently to three dimensions is to consider the mapping $\mathbf{x}(\xi, t)$ from the computational net to the physical plane, and to define vectors

$$\mathbf{g} = \partial_\xi \mathbf{x}, \qquad \mathbf{m} = \partial_t \mathbf{x}. \tag{2.1}$$

Then, assuming that $\partial^2_{\xi t}\mathbf{x} = \partial^2_{t\xi}\mathbf{x}$ we have the equation in conservation form

$$\partial_t \mathbf{g} + \partial_\xi(-\mathbf{m}) = 0 \tag{2.2}$$

To close these equations a relationship between $\mathbf{m}$ and $\mathbf{g}$ is needed. By definition we take $\mathbf{m}$ perpendicular to $\mathbf{g}$ and assume for now that a suitable scalar function $m(g)$ is available relating the magnitudes[1]. If this is so then we have a pair of conservation laws with conserved variables $\mathbf{g}$ and flux functions $-\mathbf{m}$ given by

$$\mathbf{g} = \begin{pmatrix} g\cos\theta \\ g\sin\theta \end{pmatrix}, \qquad -\mathbf{m} = \begin{pmatrix} m(g)\sin\theta \\ -m(g)\cos\theta \end{pmatrix} \tag{2.3}$$

Note (m_1, m_2 and g_1, g_2 represent the components of $\mathbf{m}$ and $\mathbf{g}$ respectively)

$$m_1 = -m(\sqrt{g_1^2 + g_2^2})\frac{g_2}{\sqrt{g_1^2 + g_2^2}}, \qquad m_2 = m(\sqrt{g_1^2 + g_2^2})\frac{g_1}{\sqrt{g_1^2 + g_2^2}}$$

or in a simple from

$$gm_1 = -m(g)g_2, \qquad gm_2 = m(g)g_1$$

[1]Taking m to be a constant recovers Huyghen's principle, which is purely geometric.

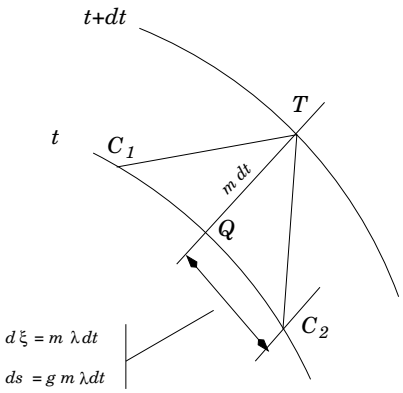

Figure 2.2: The point T on the shockwave has a domain of dependence defined by the pair of characteristics TC_1, TC_2.

from which we can derive the Jacobian matrix of the system

$$\mathbf{A} = \partial_{\mathbf{g}}\mathbf{m} = \frac{1}{g^3}\begin{bmatrix} gm'g_1g_2 - mg_1g_2 & gm'g_2^2 + mg_1^2 \\ -gm'g_1^2 - mg_2^2 & -gm'g_1g_2 + mg_1g_2 \end{bmatrix} \tag{2.4}$$

The eigenvalues of this matrix give the wavespeeds of the system to be

$$\lambda = \partial_t \xi = \pm\sqrt{-\frac{mm'}{g}} \tag{2.5}$$

and the Riemann invariants to be

$$d\theta \pm g\lambda dm = 0 \tag{2.6}$$

where $g\lambda = \frac{ds}{dt}$ represents the wave speed in the physical space. The equation 2.2 can also be written in the non-conservation form as

$$g\partial_t\theta - \partial_\xi m = 0, \qquad \partial_t g + m\partial_\xi\theta = 0 \tag{2.7}$$

These results give all of the machinery needed to employ modern methods for the numerical solution of conservation laws, and this has been done, for example in [25].

However, there are some special features of GSD that can be used to simplify matters.

2.3 Numerical aspects of Geometrical shock dynamics(GSD)

For differential equations such as 2.2 there is a corresponding integral law

$$\oint (\mathbf{g}\, d\xi + \mathbf{m}\, dt) = 0 \tag{2.8}$$

that must be valid for non-smooth solutions if a shock-capturing methodology is to be applied. Here, the integral is just $\oint d\mathbf{x} = 0$, which is clearly valid even if $\mathbf{m}$ and/or $\mathbf{g}$ should be discontinuous. Applied to an element of the computational mesh, it is simply that

$$(\mathbf{x}_A - \mathbf{x}_B) - (\mathbf{x}_C - \mathbf{x}_D) = (\mathbf{x}_A - \mathbf{x}_C) - (\mathbf{x}_B - \mathbf{x}_D), \tag{2.9}$$

This is therefore the correct discrete version of the differential equations. The nucleus of a numerical method then lies in observing that if the segment of shockwave CD is given, then constructing the ray elements CA, DB will yield the next shock segment(refer figure2.1). The geometric vectors such as AB that represent the shock segments are the conserved variables; the vectors such as CA that represent ray elements are the fluxes.

With this interpretation a "Riemann problem", required for the application of modern high-resolution schemes, is defined by giving two consecutive shock segments, say PQ, QR(refer figure2.3), and the part of the Riemann solution that is required is simply the ray element QT that extends from their intersection.

A variety of "numerical flux functions", which are essentially constructions of this ray, have been proposed for the general problem. One possibility (Godunov's method) is to solve the problem exactly using combinations of shocks and simple waves, but this is relatively expensive for GSD if the function $g(m)$ is complicated. Here we draw on another simple observation that seems to have been overlooked in this context.

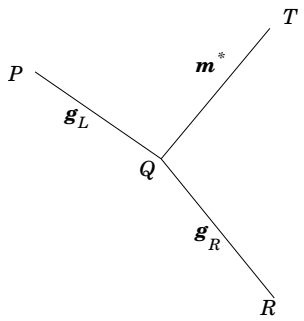

Figure 2.3: The Riemann problem for GSD consists of finding the ray that emerges from two adjacent shock segments.

The generic "viscosity form" of a numerical flux for a conservation law $\partial_t \mathbf{u} + \partial_x \mathbf{F} = 0$ is

$$\mathbf{F}^*(\mathbf{u}_L, \mathbf{u}_R) = \tfrac{1}{2}(\mathbf{F}_L + \mathbf{F}_R) - \tfrac{1}{2}\mathbf{Q}(\mathbf{u}_L, \mathbf{u}_R)(\mathbf{u}_R - \mathbf{u}_L)$$

where $\mathbf{Q}$ is the "viscosity matrix". For an upwind scheme this is taken to be

$$\mathbf{Q} = |\mathbf{A}| = \mathbf{R}|\mathbf{\Lambda}|\mathbf{L}$$

where $\mathbf{A}$ is the absolute value of the Jacobian matrix $\mathbf{A} = \partial\mathbf{F}/\partial\mathbf{u}$ whose singular value decomposition is $\mathbf{A} = \mathbf{R}\mathbf{\Lambda}\mathbf{L}$. For a linearized solver, $\mathbf{Q}$ is evaluated at some local mean state. Upwind schemes based on Riemann solvers are sometimes held to be expensive because they involve logical operations, but one case to which that certainly does not apply is when all of the wavespeeds have the same absolute value $|\lambda_i| = \lambda^*, \forall i$. In that case, which applies here, $|\mathbf{\Lambda}| = \lambda^*\mathbf{I}$, and hence, since $\mathbf{RL} = \mathbf{I}$ we have $\mathbf{Q} = \lambda^*\mathbf{I} = (\det(\mathbf{A}))^{1/n}\mathbf{I}$ if there are n unknowns. After some algebra to evaluate $\det \mathbf{A}$ we arrive in the present case at the very simple flux formula.

$$\mathbf{m}^*(\mathbf{g}_L, \mathbf{g}_R) = \tfrac{1}{2}(\mathbf{m}_L + \mathbf{m}_R) - \tfrac{1}{2}\sqrt{\frac{m}{gg'}}(\mathbf{g}_R - \mathbf{g}_L) \tag{2.10}$$

This is exactly the same formula that would be obtained from Rusanov's method[14] or the two-wave Riemann solver of Harten, Lax and van Leer[2], with the indicated

choice of estimated wave-speed. Although those flux formulas both have a reputation for dissipation in the context of gas dynamics, no such objection applies here; there is no stationary contact wave and an optimal upwind dissipation is imposed on each moving wave. For sufficiently simple functions $g(m)$ the Riemann problem can be solved exactly, but we find that the simple flux given in (2.10) gives very similar results. The coefficient $\sqrt{\frac{m}{gg'}}$, should be evaluated as the greater of the values in the left and right cells. Second-order accuracy can be achieved in the usual way by replacing the states L, R with non-linearly limited interpolations.

A Hancock type predictor corrector scheme is used with double min-mod limiter for the the reconstruction of θ and m in the cells, for second order accurate computation of GSD for all the results shown in this chapter.

2.4 The A-M Relationship

2.4.1 The original proposal

Next, we open the issue of the "correct" relationship between m and g. In a way, it is obvious that there cannot be a correct relationship, since then GSD would be a self-contained theory that would eliminate any need to solve the Euler equations. Whitham [37] originally proposed an analogy that the portion of the shock that is bounded between two rays separated by a distance $g(t)$ propagates in the same way as a shock propagating down a duct of slowly-varying area $A(x)$, say. This is governed to a good approximation by the equation

$$f(m)\frac{dm}{dt} = \frac{m}{A}\frac{dA}{dx} = \frac{1}{A}\frac{dA}{dt}$$

where

$$f(m) = \frac{m}{m^2-1}\left(1 + \frac{2}{\gamma+1}\frac{1-\mu^2}{\mu}\right)\left(1 + 2\mu + \frac{1}{m^2}\right)$$

with

$$\mu^2 = \frac{(\gamma-1)m^2+2}{2\gamma m^2-(\gamma-1)}$$

leading to the result that

$$\ln\frac{A}{A_0} = \int_{m_0}^{m} f(M)dM = G(m) - G(m_0)$$

or, in the present context, that

$$\ln\frac{g}{g_0} = G(m) - G(m_0)$$

Unlikely though it may seem, the function $G(m)$ can be evaluated in closed form, but actually varies quite slowly with m and can be simply approximated in limiting cases of strong shocks and weak shocks. The derivation is given in Appendix A following the works of Best [5].

2.4.2 A modification

One drawback to this relationship is that it makes a rather poor prediction of the speed with which information propagates along the shock. Since one object of our intended application is to study exactly this, we will investigate what modifications would be needed to remedy this. In fact, it turns out that a simple modification to the A-M formula will remove it completely. Consider the set up shown in figure 2.4, with a standing normal shock. The upstream condition is given with fluid velocity u_0, Mach number m and the post shock fluid velocity is u_{post}, sound velocity is a_{post} and with Mach number m_{post}. It is easily shown from the geometry of the true characteristics that the exact value of wave-speed along the shock (the distance OA and OB) is

$$\frac{g(m)d\xi}{dt} = a_{post}\sqrt{1-m_{post}^2} \tag{2.11}$$

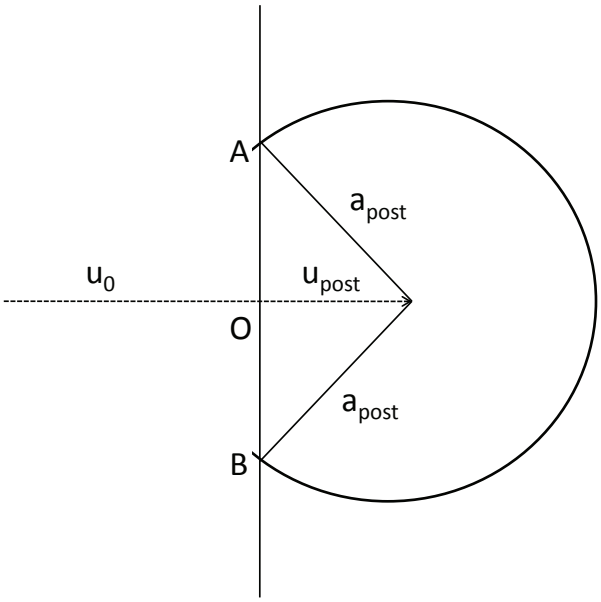

Figure 2.4: The propagation of disturbance along the normal stationary shock

Inserting results from the Rankine-Hugoniot conditions and considering the speed of sound to be unity upstream gives

$$\frac{g'}{g} = -\frac{(\gamma+1)m^3}{((\gamma-1)m^2+2)(m^2-1)}$$

which integrates to give

$$g(m) = \frac{(2+m^2(\gamma-1))^{\frac{1}{1-\gamma}}}{\sqrt{m^2-1}} \tag{2.12}$$

The plots of the variation of the Area-Mach relations with Mach number and the wave speeds in the physical space along the shock and the wave speed in the $\xi - t$ space is shown in figure 2.5. The relations are tabulated in 2.1. The detailed derivation of the Area Mach relation by Whitham is listed in the Appendix A. We have used the relation of Prasad's model which is derived for a non linear wave front(the modified equations being listed in the Appendix B for the shock front) just for the sake of simplicity of the relation and for some numerical comparison. As stated

earlier its not possible to get the exact details of the shock and each relation has its own disadvantages. Clearly from the plot of the wave-speeds indicated in figure 2.5 for low Mach numbers the shock speed predicted by Whitham's relation is almost half of the actual propagation wave speed.

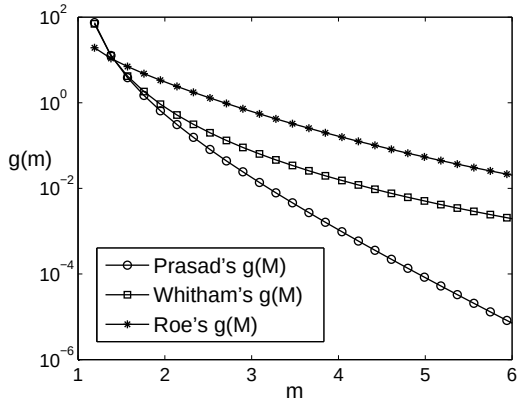

(a) Semi-log plot of Variation of Area Mach models with m

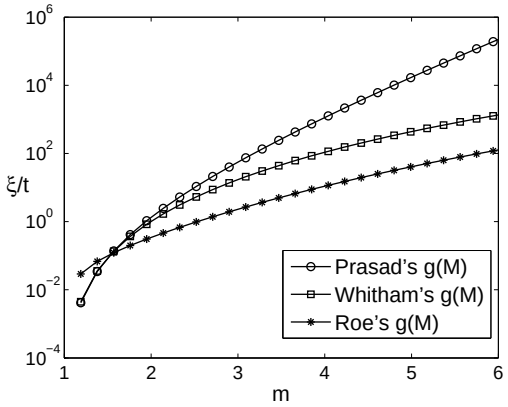

(b) Semi-log plot of Wave-speeds in the $\xi - t$ plane

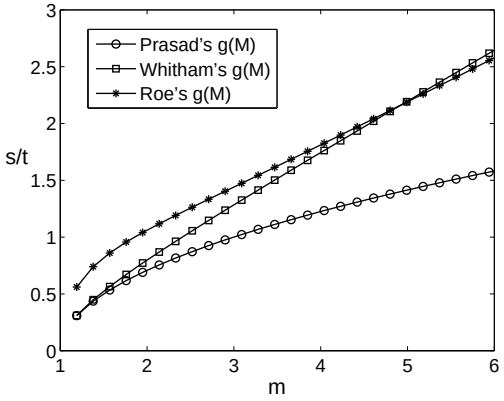

(c) Wave-speeds in the x-y space along the shock

Figure 2.5: Area Mach relations and wave-speeds in both the $\xi - t$ plane and x-y space as a function of m

2.4.2.1 Controversial aspects of GSD

Of course, one may also challenge the analogy between an unconfined flow and a confined one. Maslov[17] wrote the isentropic Euler equations in a local coordinate system aligned with the shockwave. He derived an infinite hierarchy of governing

Table 2.1: Area Mach relations and the wavespeeds

A-M models	g(m)	$\frac{ds}{dt}=\frac{g(m)d\xi}{dt}$
Whitham	$\frac{dg}{dm} = \frac{-gm\alpha(m)}{m^2-1}$	$\sqrt{\frac{m^2-1}{\alpha(m)}}$
Prasad	$(m-1)^{-2}e^{(-2(m-1))}$	$\sqrt{\frac{m-1}{2}}$
Roe	$\frac{(2+m^2(\gamma-1))^{\frac{1}{1-\gamma}}}{\sqrt{m^2-1}}$	$\sqrt{\frac{(m^2-1)(2+m^2(\gamma-1))}{(\gamma+1)m^2}}$
with	$\alpha(m) = (1+\frac{2(1-\mu^2)}{(\gamma+1)\mu})(1+2\mu+\frac{1}{m^2})$	$\mu^2 = \frac{(\gamma-1)m^2+2}{2\gamma m^2-(\gamma-1)}$
and	$\frac{ds}{dt}$ is the wave speed in the physical space	

equations, with each member of the hierarchy involving the derivative behind the shock at one order higher. The sequence of equations can be truncated by making some assumption about the next member of the sequence (although no assumptions about later members are needed). Srinivasan and Prasad[32] interpreted this as indicating a defect in Whithams procedure, and proposed to augment it by including a gradient behind the shock as a further unknown and proposed a 3×3 system of equations to incorporate it(the equations are listed in the Appendix B). Although correct in principle, because it represents the effects of waves that catch up with the shockwave from behind, this does not bring about much practical advantage because data for this gradient is difficult to provide. Best[5, 6] performed an analysis similar to that of Maslov, but was able to conduct it more simply and to remove the restriction to isentropic flow. In [6], he established that to lowest order the confined and unconfined problems were indeed identical, and found essentially the same error term as presented on an empirical basis in Whitham's book[36]. It is the product of two factors, one of which is small when the flow behind the shock is close to uniform, and the other is small if the shock is weak. Since our objective in this paper is merely to provide qualitative results, we do not feel that we can do better than to follow Whitham's model, although we do work with a quite different form of it in the three-dimensional and moving-medium cases. However, we will investigate how the results are affected by alternative $A-M$ relationships. To see the difference

between Whitham's $A - M$ model and our model we have considered the solution for 3 different problems to see the impact of the area models on the solution. No quantitative comparisons with Euler computations are made for these cases but only the differences between the models are indicated. The qualitative comparison and the validity of GSD is made for the case of shock-vortex interaction model with the Euler computations.

2.5 Test problems for illustration

2.5.1 Shock-diffraction problem - Simple wave solution

First we shall consider the case of a shock propagating along an expansion corner. In GSD it is given by a simple wave solution in the $\xi - t$ plane. The problem setup is described in figure 2.5. This case has been extensively studied in Whitham [37]. The solution to the Riemann problem for this simple wave can be given by integrating the left running invariants as

$$d\theta - g\lambda dm = 0, \quad \theta_w = \int_{m_0}^{m_w} (\frac{dm}{g\lambda}) \tag{2.13}$$

Prasad's model can be integrated easily as

$$\theta_w = 2\sqrt{2}(\sqrt{m_w - 1} - \sqrt{m_o - 1}) \tag{2.14}$$

and with Roe's model

$$\theta_w = \left[\frac{1}{2\sqrt{\gamma - 1}} \ln(\frac{3 - \gamma + 2m^2(\gamma - 1)}{\sqrt{\gamma - 1}} + \sqrt{(\gamma - 1)m^4 + (3 - \gamma)m^2 - 2)}\right]_{m_o}^{m_w} \tag{2.15}$$

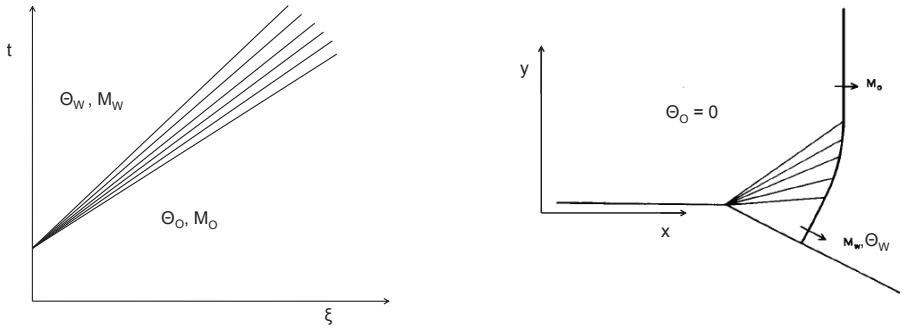

(a) $\xi - t$ plane (b) $x - y$ space

Figure 2.6: Shock diffraction problem setup

For the Whitham's model the closed form integration is complicated. The closed form expression is obtained in the limits of weak and strong shocks [37] as follows

$$\theta_w = 2\sqrt{2}(\sqrt{m_w - 1} - \sqrt{m_o - 1}), \quad m \to 1 \tag{2.16}$$

$$\theta_w = 2.2526 \ln \frac{m_w}{m_o}, \quad m \to \infty \tag{2.17}$$

It should be noted that in the weak shock limit the result of Whitham's model and Prasad's model are identical, however, they are both in error by a factor of one-half.

To compare the variation of these models for the simple wave solution we can look at the plot of the variation of $\frac{d\theta}{dm}$ with m. This is nothing but the inverse of the wave-speed in physical space(refer equation 2.13 with $g\lambda$ representing the wavespeed in physical space). From the comparison with the models, for higher Mach number both the variation of Whitham's model and Roe's model which is exact in this respect are almost the same. In the case of lower Mach numbers the difference is that Whitham's model computes lesser wave-speed of propagation along the shock. To see the difference in the Area-Mach models the variation of the diffraction angle with the change in strength for two different initial shock strengths are plotted in figure 2.7, and for lower shock-strength the behavior of Whitham's model and Prasad's model

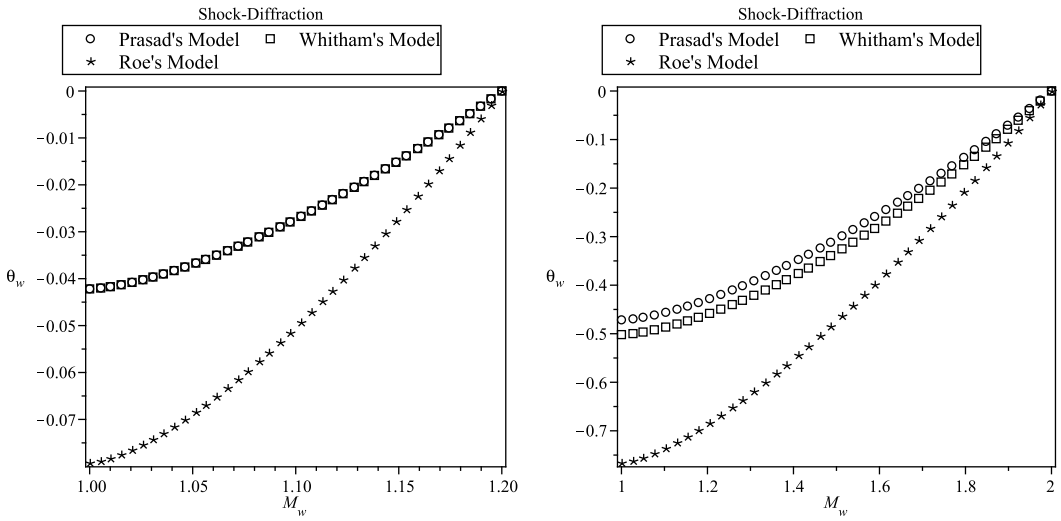

(a) Initial shock strength of $m_o = 1.2$ (b) Initial shock strength of $m_o = 2.0$

Figure 2.7: Variation of wall Mach number m_w with the change in diffraction angle θ_w for two different initial shock strengths.

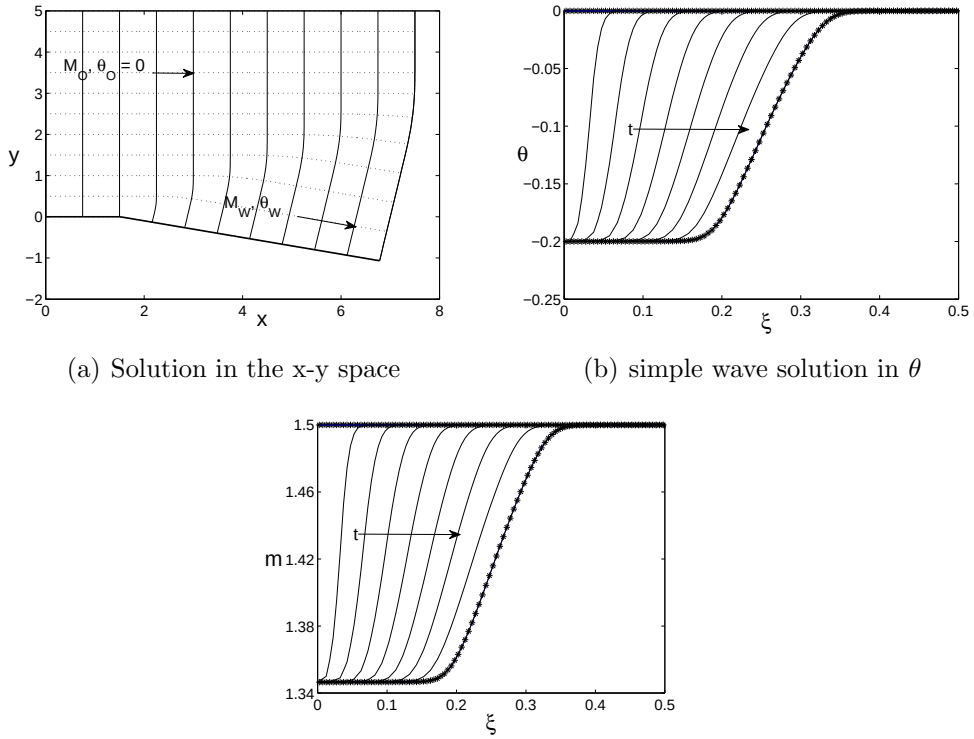

(a) Solution in the x-y space

(b) simple wave solution in θ

(c) simple wave solution of m

Figure 2.8: Shock-diffraction problem solution using Roe's model for shock strength of $M_O = 1.5$ and θ_W = -0.2 rad. The dotted line represents the rays in fig2.8(a). The solution is plotted at intermediate time intervals

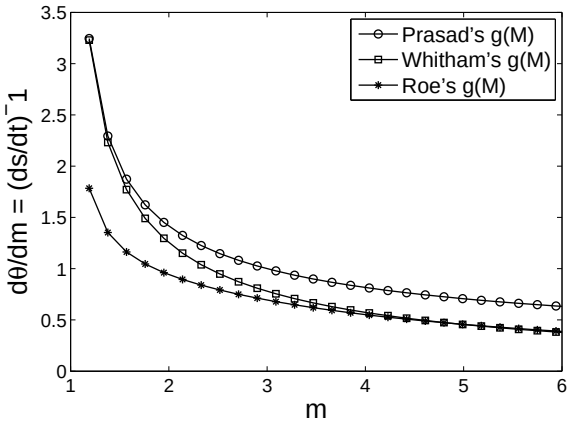

Figure 2.9: Relation between the change in θ with the change in strength of the shock

is the same which could be seen from the analytical results as well. We can say that while using Roe's model requires a higher diffraction angle is required to bring the wall Mach number to unity.

2.5.2 Shock-shock problem - propagation of a shock over a compression ramp

In this case of a shock moving over a ramp there is a formation of kink along the shock. This is also known as shock-on-shock. The problem setup is given in the figure 2.12. The shock-shock jump relations can be obtained from the conservation form of the GSD equations giving a relation between the angle of the compression ramp and the Mach strength of the shock closer to the wall. There are quantitative differences between the solutions depending on the relation for g. The relations across the shock-shock can be given from the jump relations

$$s_s = \frac{[-\mathbf{m}]}{[\mathbf{g}]} \tag{2.18}$$

where s_s represents the speed of the shock-shock(the speed of propagation of the kink along the shock)in $\xi - t$ plane. With $\theta_O = 0$ the above relation can be simplified to

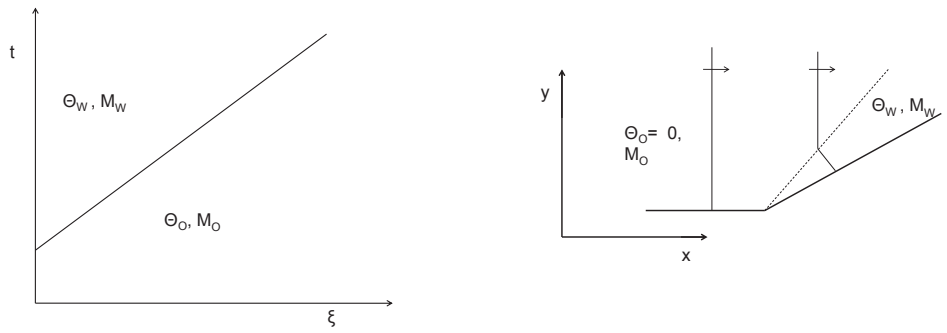

(a) $\xi - t$ plane (b) $x - y$ space

Figure 2.10: Shock-shock problem setup. The dotted line representing the direction of propagation of the kink in the x-y space.

give

$$\cos\theta_w = \frac{m_w g_w + m_o g_o}{m_w g_o + m_o g_w} \tag{2.19}$$

Plots of the variation of ramp angle to that of the wall Mach number are plotted in figure 2.11 for two different initial shock strengths. As seen earlier there is no difference between the Prasad's model and Whitham's model for weaker shock strengths. For a given ramp angle we see that Roe's model gives a higher compression than that obtained using Prasad's model for both the initial shock strengths. We can observe the quantitative differences based on the choice of the Area-Mach models. The angle θ_W in all the plots are plotted in radians.

2.6 Extension of Geometrical shock dynamics(GSD) for a shock propagating into a moving medium

2.6.1 Governing equations

Before moving into the study of other problems using GSD we shall first visit the topic of shock propagation into a uniformly moving medium. This is simply a Galilean transformation of the original problem, but the first attempt to do this [8]

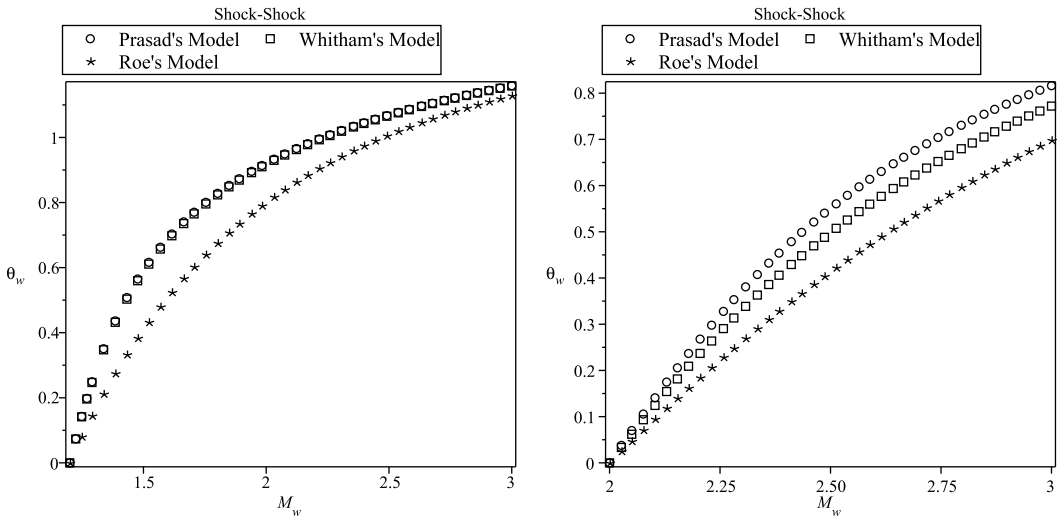

(a) Initial shock strength of $m_o = 1.2$ (b) Initial shock strength of $m_o = 2.0$

Figure 2.11: Variation of wall Mach number m_w with the change in the ramp angle θ_w for two different initial shock strengths.

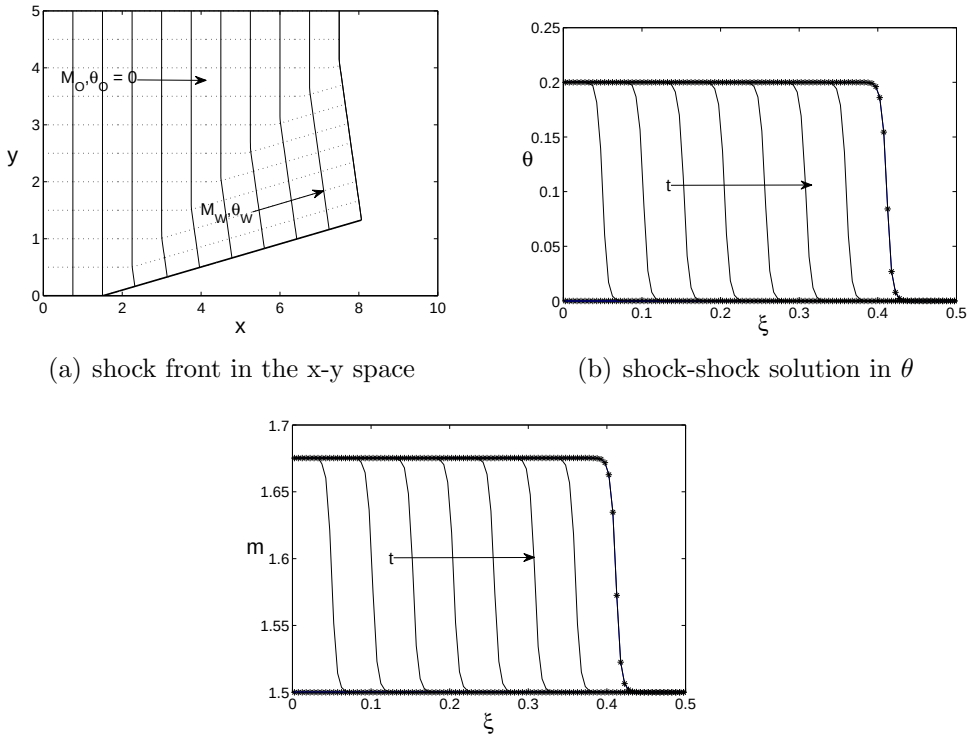

(a) shock front in the x-y space

(b) shock-shock solution in θ

(c) shock-shock solution in m

Figure 2.12: Shock-shock problem solution using Roe's model for shock strength of $M_O = 1.5$ and $\theta_W = 0.2$ rad . The dotted line represents the rays in fig2.12(a). The solution is plotted at intermediate time intervals

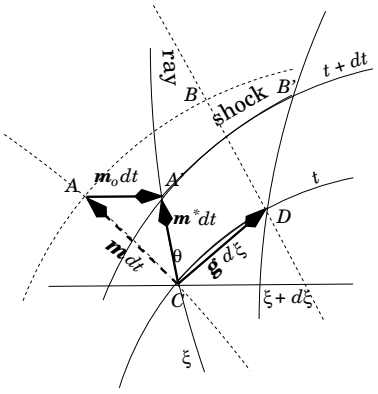

Figure 2.13: Transformation of the computational net for a moving medium. The elements of the shock front are unchanged. The points A, B are displaced to A', B'.

was actually incorrect. The correct treatment was provided by Whitham[39] replacing the "conservation-law plus mapping" arguments by an approach that is completely equivalent but more analytical. The solution was defined in the form of $\alpha(x, y)$ such that the level line $\alpha(x, y) = a_0 t$ represents the shock location at time t (here a_0 is the sound speed in the undisturbed medium.) This function obeys a second-order scalar differential equation having a similar structure to the one describing potential flow.

In this framework, Whitham described the extension to a non-stationary medium as involving "nontrivial details". The idea works well enough if the uniform speed of the medium is small compared with the propagation speed of the shock, but becomes very cumbersome if the speeds are comparable. In that case, one cannot predict in what direction the shock will move, and indeed it may frequently repass a particular location. The function $\alpha(x, t)$ then becomes multi-valued, and its numerical computation becomes tricky. Also the numerical computation is expensive as it involves solving the problem in 2-D space, we no longer have a reduction in dimensionality. By contrast, we propose here the formulation that solves the GSD equations in the ray coordinates retaining its 1-D nature and then constructs the shock fronts directly in the physical plane, the extension of which is trivial in implementation, as well as in principle.

Suppose that the medium into which the shock propagates is itself moving in the positive x-direction with speed $m_0 a_0$. Then an observer moving with this speed would see the original problem, and could compute it as above. To obtain the same results, a stationary observer simply has to add vectors $(m_0 dt, 0)$ to the ray elements in figure 2.13. The problem can be formulated as

$$\partial_t \mathbf{x} = m_o \mathbf{e}_x + \mathbf{m}, \qquad \partial_\xi \mathbf{x} = \mathbf{g} \tag{2.20}$$

which leads to the identical conservation laws as in the stationary case. The conservation laws just indicate that the sum of the vectors enclosing adjacent ray elements and the shock patches at consecutive times add up to zero. Simply adding the term $m_o \mathbf{e}_x$ allows the geometrical interpretation to be retained and avoids all of the disadvantages listed above. This is the same case with the shock front propagating into a uniformly moving medium.

$$\partial_t \mathbf{g} - \partial_\xi \mathbf{m} = 0 \tag{2.21}$$

Nor is the calculation of the function $m(g)$ in any way affected, and if the solution is written as $\mathbf{m}(\xi, t), \mathbf{g}(\xi, t)$ then it is unchanged. All that does change with regard to the governing equations is that the mapping into the physical plane is now given by (2.20)[2]. Because of this m is no longer the rate of advance of the shockwave normal to itself. That velocity is now given by $m \sin\phi$ where ϕ is the angle between the shock-front and the ray, ie

$$\sin\phi = \frac{CA' \cdot CD}{|CA'| \cdot CD|} = \frac{m_0 \sin\theta}{(m^2 + 2mm_0 \cos\theta + m_0^2)^{\frac{1}{2}}} \tag{2.22}$$

This agrees with the result found in [39] by a very different and much lengthier argument. Note that we can have $\phi = 0$, in which case the shock is stationary,

[2]It does not matter which of the two equations is used for the mapping; conservation guarantees that they will yield the same results.

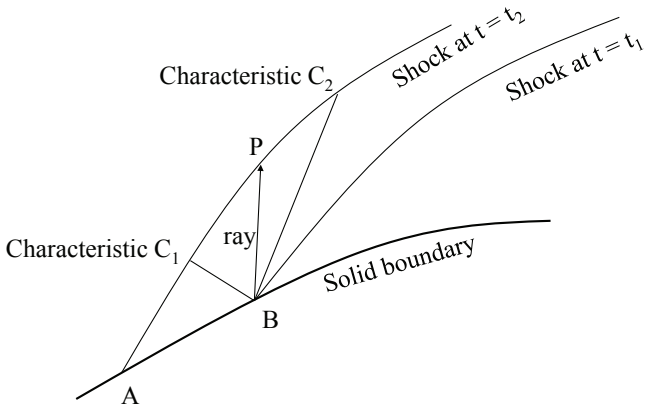

Figure 2.14: A shockwave moving from B to A along a solid surface.

and the rays move along it, or $\phi < 0$ when the shock is swept along with the flow. The case of $\phi = 0$ is a simple a stationary oblique shock. In this case the rays get convected along the shock with the tangential velocity across the shock, so the rays can be viewed as fictitious dyes on the shock which for the case of an oblique shock gets convected along the shock.

Boundary conditions for a moving medium

Although pure initial value problems are sufficient for our purposes in this thesis, we briefly discuss boundary conditions for GSD in the interest of completeness. For the previous cases considered we have non reflecting boundary conditions. With the freestream moving with a uniform velocity there can be an important change in the boundary conditions. For example, in the reflected shock problem an oblique wave originates at a more-or-less fixed point in x, y. At this point, new rays are created because the boundary is no longer given by $\xi = constant$, as the shock no longer lies at right angles to the boundary. Therefore boundary conditions must be supplied. In this case of a standing oblique shock the rays are generated at the rate of the

tangential velocity along the shock and the boundary conditions are trivial for this case as there are no waves generated, the only information for this case is that of the introduction of new rays at each time step of computation.

Suppose that at a certain time the shock springs from a point B on a solid surface as shown in figure 2.14, and makes an angle ϵ with it. After an interval dt the shock has moved to a location A on the surface, and the ray originating at B now meets the shock at P. The characteristics carrying information from B meet the shock in C_1, C_2. If the distance PC_1 is less than PA then it will be necessary to specify two boundary conditions for the shock at B, otherwise just one. Using the GSD relations to find the distance PC_1, we find that two conditions are needed if

$$\sqrt{\frac{-m'g}{m}} \geq \cos\phi + \sin\phi\cot\epsilon \tag{2.23}$$

If the shock is moving to the right, then no boundary conditions are required if $PC_2 \leq PA$, which translates to

$$\sqrt{\frac{-m'g}{m}} \leq \cos\phi - \sin\phi\cot\epsilon \tag{2.24}$$

For intermediate cases, one boundary condition is needed.

2.7 Propagation of a sinusoidal shock

The previous two illustrations can be seen as more of a boundary value problem where the shock is perturbed by the change in the geometry or the direction in which it is traveling along the boundary. Our next illustration is an initial value problem with periodic boundary conditions. It models the reflection of a plane shock off a corrugated surface. Schematic setup is shown in figure 2.15. Experimental and theoretical studies were carried out by Briscoe and Kovitz [7]. The propagation of a

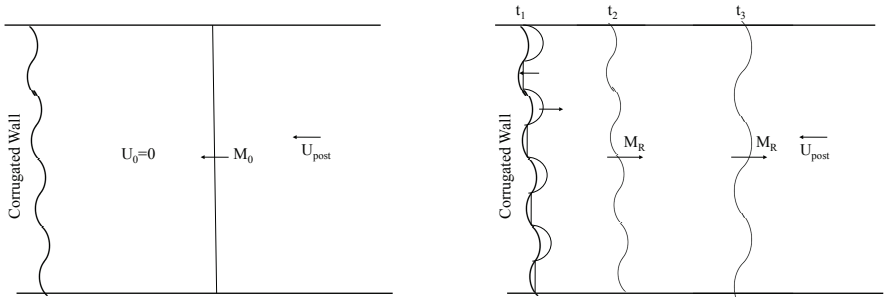

(a) Plane shock of strength M_0 before reflection

(b) After reflection from the surface with strength M_R

Figure 2.15: Schematic setup of a planar shock after reflection from corrugated surface with strength

simple sinusoidal shock as an initial value problem using GSD has been performed by Prasad [19] to study the corrugational stability of shock waves.

For mathematical convenience we have considered a periodic disturbance in both the strength and shape of the shock. In the real situation of shock being reflected from a corrugated surface the shock-wave would move into a medium which is not stationary, the extension of GSD theory to the moving medium is discussed in the previous section and as can be deduced, it is nothing more than a mere translation of the shock with the upstream velocity and the solution only changes in the $x - y$ space retaining the same solution to the Riemann problem in the $\xi - t$ space. In [19] both the structure of having an initial sinusoidal as well as shapes with other curvatures has been studied, for a larger range decay of the disturbances. Here only the case of a sinusoidal shock front moving into a stationary medium is presented. Periodic boundary conditions are considered on either side of the domain to replicate the shock propagation along a closed channel.

The perturbations along the shock front tend to decay but the maximum and minimum strength of the shock doesn't decay monotonically. Kinks or shock-shocks form along the shock-front and this accounts for the spikes in the distribution of the maximum and the minimum Mach number along the shock, as shown in figure

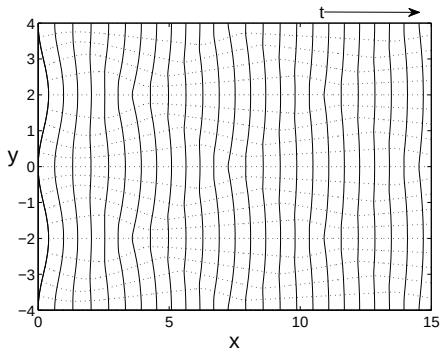

(a) $x - y$ space

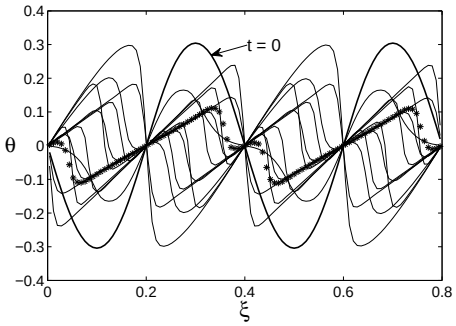

(b) variation of the ray angle in ξ with time

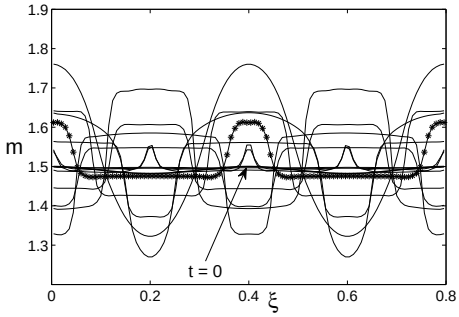

(c) variation of the strength of the shock along ξ with time

Figure 2.16: Propagation of a sinusoidal wavefront using Roe's A-M relation. Dotted lines in 2.16(a) indicate rays. The lines with * in 2.16(b) and 2.16(c) shows the solution at final computational time

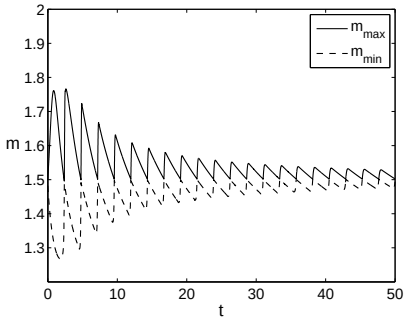

(a) Maximum and minimum strength of the shock at each time interval along the shock

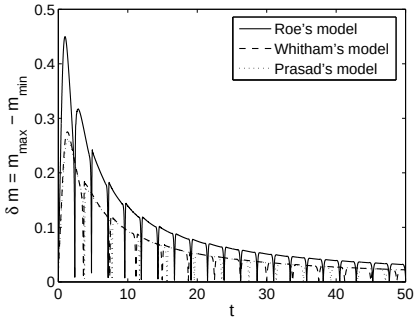

(b) Mach strength change along the shock

Figure 2.17: Changes in maximum and minimum shock strength over time

2.17(a).

This shows that the disturbances that propagate along the shock give rise to shock-shocks which will keep interacting with the other shock-expansion waves and would take a larger time for decay, rather than a monotone decay in the amplitude of the perturbation. This behavior is observed irrespective of the nature of the Area-Mach model, though there are a few quantitative differences observed. Roe's Area Mach model has been considered for the case shown in figure 2.16. At large times we see that the shock wave tends to become planar, with perturbations decaying out indicating the stability of the shock-front. The rays tend to converge as well as diverge showing both shock wave focussing and diffraction.

To see a difference between the Area-Mach models the difference between the maximum and minimum shock strength with time is plotted in the figure 2.17(b). The peaks of the variation in Mach strength are close for both Prasad's model and for Whitham's model. This is because g(m) is similar for these models at low Mach numbers. The differences are greater for Roe's model. Qualitatively all the models are in agreement.

2.8 Modeling of shock-vortex interaction

2.8.1 Note on Oblique shock-vortex interaction

Having defined the details of the boundary conditions that need to be incorporated to the case where there is a problem of ray generation we shall deal with the case of an oblique shock interacting with a vortex. The setup of an oblique shock-vortex interaction is what we would like to analyze as that would closely represent the discrete vortices interacting with the foot of the λ-shock in SBLI. The case of a single vortex passing through either a normal shock or an oblique shock is merely a translation along the shock. Along the oblique shock the disturbance gets convected with the

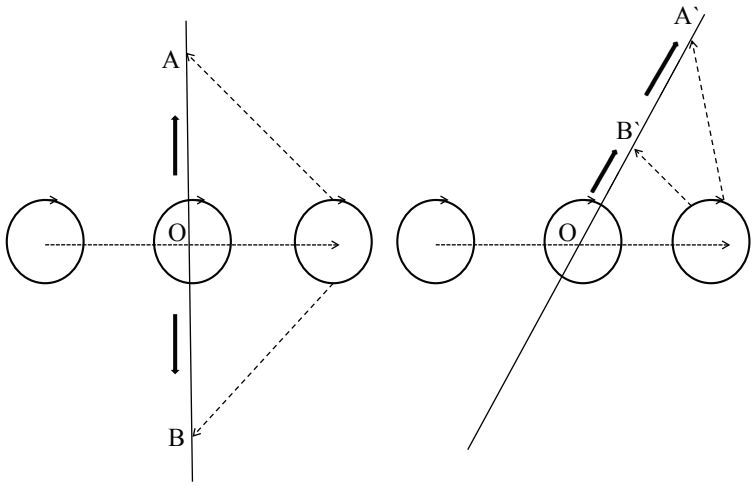

Figure 2.18: Schematic setup of a normal shock-vortex interaction and an oblique shock-vortex interaction

tangential component of the free-stream velocity.

The schematic representation is shown in figure 2.18. The vortex after interacting with the shock is distorted to an ellipse, although It is depicted as a circle for the case of simplicity in the figure 2.18.

For a normal shock the disturbances travel along OA and OB with the same speed from the point of interaction O. This speed is given by (as discussed in the section 2.4.2)

$$\frac{g(m)d\xi}{dt} = a_{post}\sqrt{1 - m_{post}^2} \tag{2.25}$$

As shown in the figure 2.18, if the post-shock Mach number is supersonic which occurs for an oblique shock, both the disturbances travel along same direction from the point of interaction. In the oblique shock the disturbance at OA' travels with a faster speed with addition of tangential velocity and the other disturbance OB' travels at a lesser speed, the difference between the propagation speed of disturbance and the tangential velocity across the shock.

If multiple vortices pass through an oblique shock at the same point in space,

the resulting waves can overtake each other, although large amplifications cannot be generated in this way. For the case of simplicity as well as having non reflecting boundary conditions without any ray generation, we shall only consider the case of a normal shock interacting with a single vortex passing through it for most of the thesis.

2.8.2 Normal shock-vortex interaction

Consider a stationary shock with a flow coming from right to left and then a vortex rotating counterclockwise interacting with the shock. In this set up the upper half of the vortex pushes the shock downstream and the bottom half pushes it upstream. To model the shock vortex interaction exactly, getting the details of the perturbation along the shock once the vortex has passed through is difficult because the interaction is non-linear. If the interaction had been linear the change in the shock strength would be smooth producing a sinusoidal disturbance of one period in Mach strength along the shock, but with the interaction being completely non linear the symmetry in pushing and pulling of the shock does not occur [13]. Thus a shock-vortex problem translates to an initial value problem in the Mach number distribution along a shock in GSD.

The numerical details of the problem setup are as follows. Consider a standing normal shock along y axis(L units in both positive and negative axis)with 50 ray cells per unit length. The initial condition is given by

$$\begin{aligned} m(\xi,0) &= m_o(1-\delta m \sin\frac{\pi(L\xi)}{2r_v}), \quad |\xi| < \frac{2r_v}{L} \\ &= m_o, \quad |\xi| >= \frac{2r_v}{L} \\ y(\xi,0) &= L\xi \\ x(\xi,0) &= 0 \end{aligned} \tag{2.26}$$

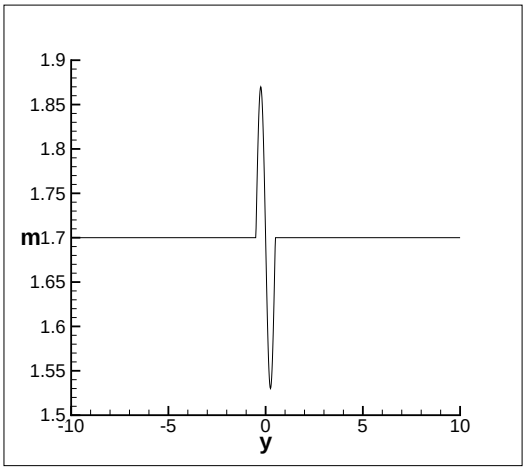

(a) Initial m distribution along the normal shock front

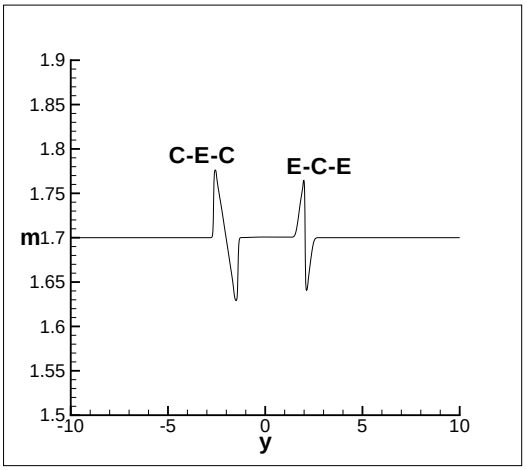

(b) m distribution along the shock after t = 2.2 units

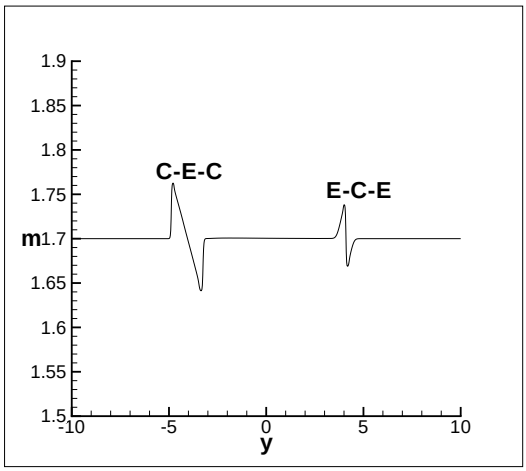

(c) m distribution along the shock after t = 4.4 units

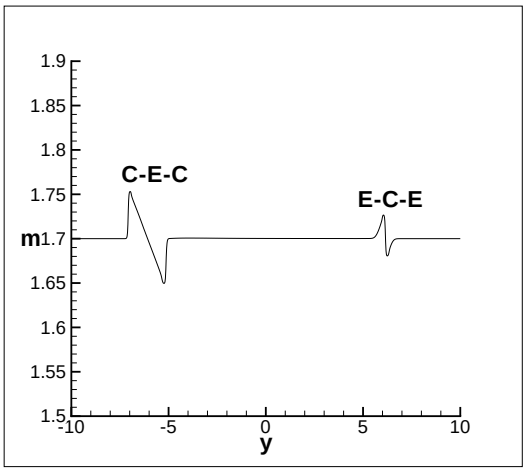

(d) m distribution along the shock after t = 6.6 units

Figure 2.19: GSD results : At early times using Roe's Area model for a sinusoidal perturbation in Mach number for a planar shock of strength 1.7

with m_o the strength of the unperturbed shock, δm the amplitude of the perturbation in Mach strength, 2L the total length of shock considered in the domain and r_v a reference length. The initial condition in Mach number distributions is shown in 2.19(a). Time-steps are chosen such that CFL condition is maintained within the limits of 0.3 to 0.5. The propagation of the disturbance along the shock for 10% perturbation in initial Mach strength of 1.7 is shown in figure 2.19.

We observe a set of waves going along both the directions along the shock from the point of interaction. The two waves are of different nature. Left going waves(the

waves going along negative y direction) resemble the classical N waves which decay like $t^{-\frac{1}{2}}$ for scalar problems. We will call them Compression-Expansion-Compression(C-E-C) wave as they are wave structure with two shocks eroded by a single expansion wave. The other wave which moves towards the right(the positive y direction) is of different nature with two expansion waves eroding a single shock wave. We will call the waves of this type as E-C-E waves denoting an expansion-compression-expansion wave structure. These waves have a more complicated behavior than the C-E-C waves. This is illustrated in Appendix C by solving analytically the problem for the inviscid Burger's equation.For E-C-E waves there is an initial decay of t^{-1} but unless the initial data is symmetrical, one wave decays completely to zero. The remaining wave then decays at $t^{-\frac{1}{2}}$(figure 2.22(b)).

In the case of GSD even with the initially symmetrical data we can see the asymmetry in the nature of the waves as well as their structure. Remarkably similar behavior will be observed from the Euler computations of shock vortex interaction in the next chapter.

The maximum and the minimum amplitude of each disturbance is plotted against the non dimensional distance from the point of interaction in figure 2.20 for four different initial perturbations. The distance is scaled with the radius of the vortex core. The amplitude difference in Mach number is converted to the disturbance in pressure with p^* representing the downstream pressure of the undisturbed shock front. Each plot includes trend lines indicating decay rates of $t^{-\frac{1}{2}}$ and t^{-2}. Since we are looking at self similar wave solutions, the decay rates are plotted against distance but are described in terms of power law decay of time through out this work.

The C-E-C waves all reach the asymptotic decay of $t^{-\frac{1}{2}}$ except for the weakest disturbance which has probably not reached the asymptotic regime. The behavior of the E-C-E wave follows the pattern described earlier. There is an initial rapid decay of t^{-1} and then for the strongest disturbance the minimum value falls towards zero,

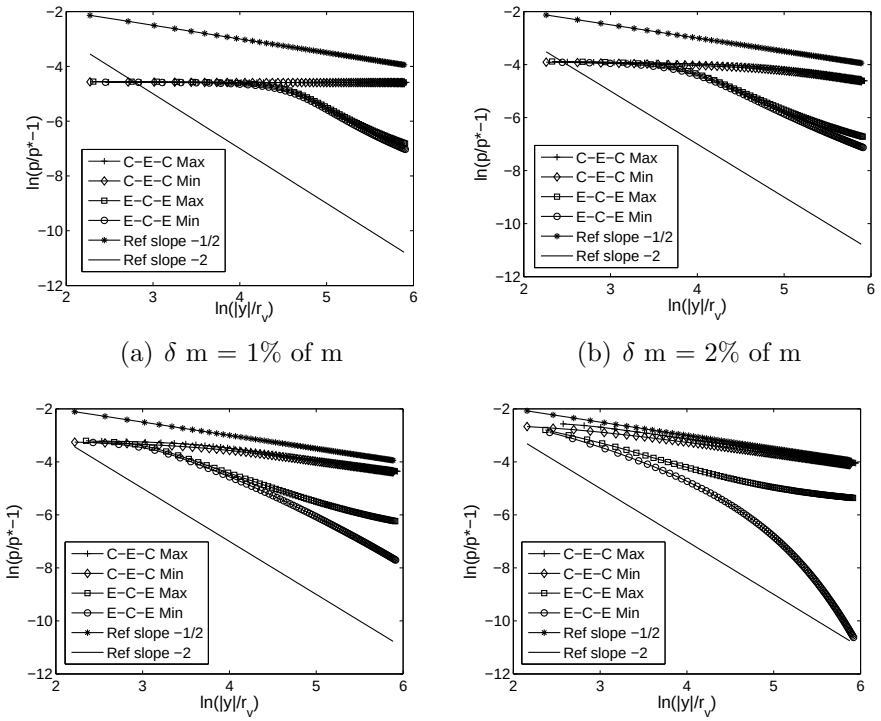

(a) δ m = 1% of m

(b) δ m = 2% of m

(c) δ m = 4% of m

(d) δ m = 8% of m

Figure 2.20: GSD results : Power law decay of the wave amplitudes with non dimensional distance using Roe's Area model for shock with m = 1.7

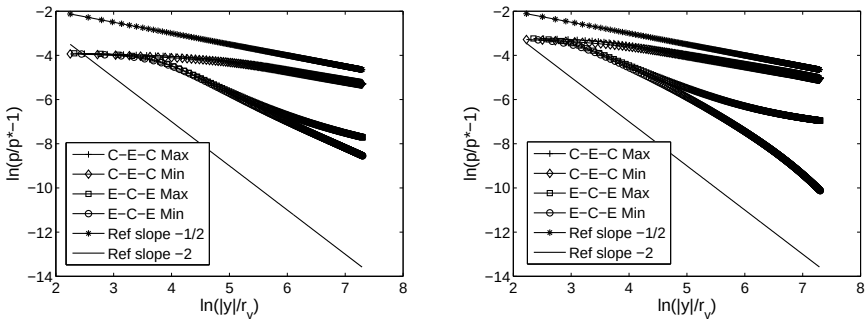

(a) δ m = 2% of m (b) δ m = 4% of m

Figure 2.21: GSD results : Power law decay of the wave amplitudes with non dimensional distance using Roe's Area model for shock with m = 1.7 for larger distance

while the maximum value tends toward a rate of $t^{-\frac{1}{2}}$. For the other disturbances this occurs later and has not happened yet. This is verified by plotting the solutions in figure 2.20(b) and 2.20(c) for a long range. They are shown in the figure 2.21. This behavior of the E-C-E wave is predicted in Appendix C.

With the increasing amplitude of the perturbation the decays get to the asymptotic limit of power law faster, this can be explained by the propagation of similar waves in a scalar case. In the case of Burger's equation for a smooth initial distribution of a scalar, say u, the initial time when the shock is formed is given by

$$t = \frac{-1}{u'(x_0)_{min}} \tag{2.27}$$

So in our case we can plausibly deduce that the time for the formation of the shock is inversely proportional to the amplitude of the disturbance. More generally, the time to reach asymptotic conditions will decrease with the increase in perturbation amplitude.

A more detailed argument being that in the simple wave approximation along either of the characteristics we have that the characteristic speed λ satisfies Burger's

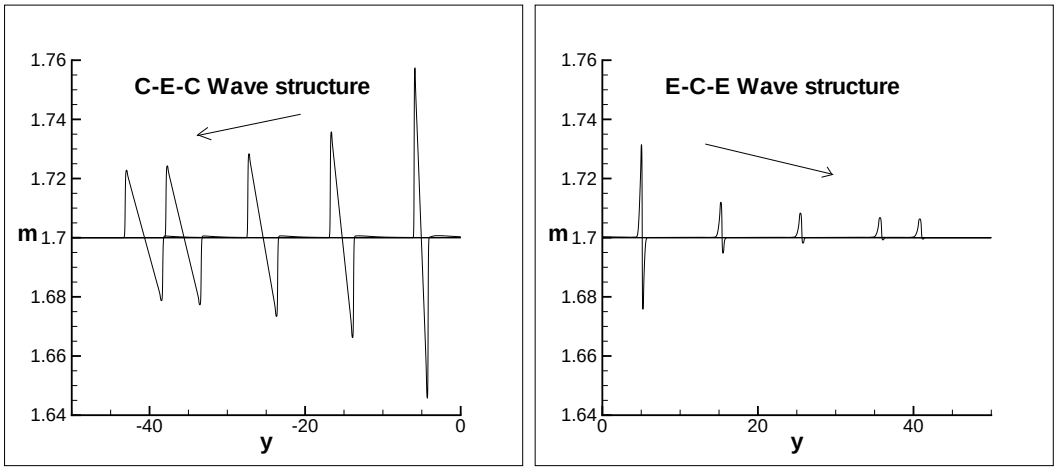

(a) Left going N waves at 5 different time intervals

(b) Right going N waves at 5 different time intervals

Figure 2.22: GSD results : At later times using Roe's Area model

equation,

$$\lambda_t \pm \lambda\lambda_\xi = 0 \tag{2.28}$$

so that the quantity λ will behave exactly like the Burger's solution in the smooth region. The wave-speed λ is a function in m so the above equation can be further reduced to

$$m_t \pm \lambda m_\xi = 0 \tag{2.29}$$

Though the above argument is valid only when the solution domain m is smooth, for a first order approximation of considering shock-shock as compression waves the argument for the time for the formation of the asymptotic decay is valid.

In order to compare the three Area-Mach relationships the wave structures obtained from all the three models are plotted in figures 2.22, 2.23 and 2.24. For Prasad's and Whitham's model the minimum of the E-C-E wave decays much earlier. However the three models do give roughly similar results, and it is hard to say on this basis whether any of them is best. We have chosen to use Roe's model because of its ability to match the exact wave speeds.

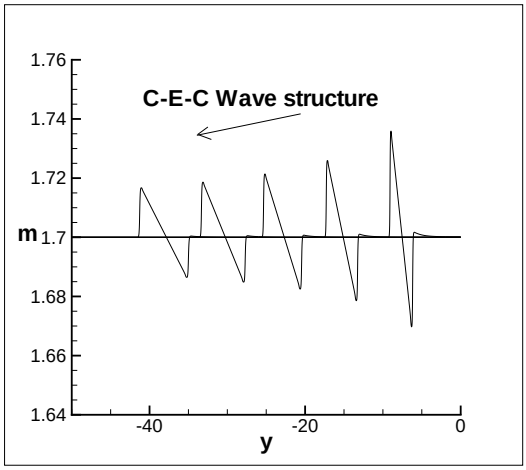

(a) Left going N waves at 5 different time intervals

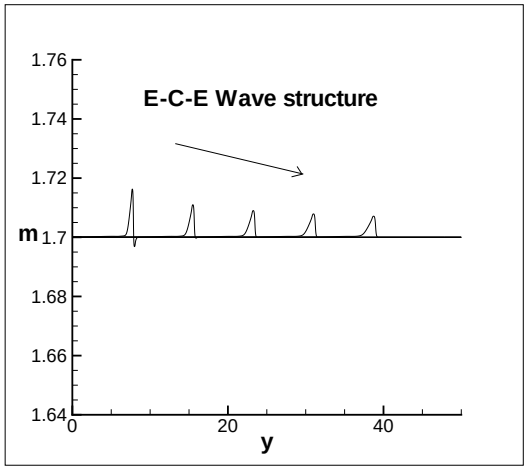

(b) Right going N waves at 5 different time intervals

Figure 2.23: GSD results : At later times using Whitham's Area model

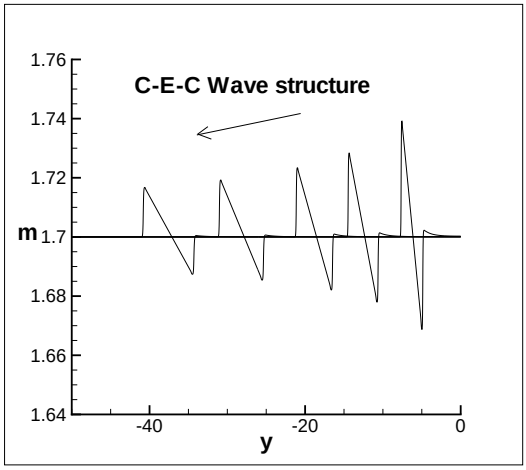

(a) Left going N waves at 5 different time intervals

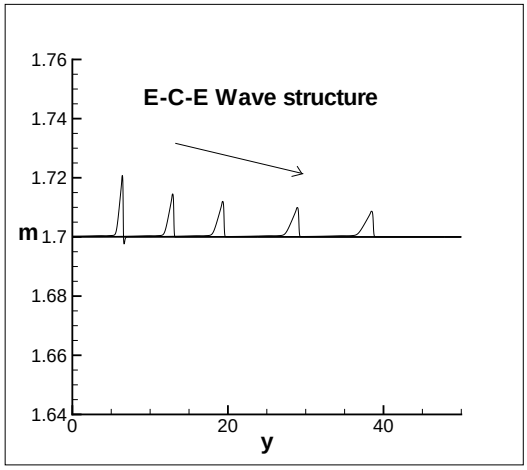

(b) Right going N waves at 5 different time intervals

Figure 2.24: GSD results : At later times using Prasad's Area model

2.9 Interaction with multiple vortices

We see from DNS studies of SBLI [22](figure 1.4) that there are multiple vortices which interact with the oblique shock at its foot. This translates into a normal shock with each vortex reaching it at different time and at different locations.

The main information is that with a single shock vortex interaction two waves of different nature are generated and in an oblique shock when the post shock state is supersonic both the waves would travel along the same direction from the point of interaction. One wave would travel faster with the speed of $m_t + c$ and the other being $m_t - c$ where the m_t represents the tangential velocity of the flow field across the shock and c being the wave-speed.

For an oblique shock the point of interaction of the multiple vortices remains the same and there are both fast and slow moving waves along the shock. So with multiple vortices the waves of opposite family will interact. This interaction can be studied with the case of GSD using normal shock with two vortices interacting such that E-C-E wave of one perturbation interacts with the C-E-C wave of the other perturbation. A simple setup of having two different vortex interaction is modeled in GSD and is as shown in figure 2.25. The initial conditions are similar to that of a single shock-vortex interaction but having two perturbation separated by 40 r_v units.

We observe the waves to merely pass through retaining their nature and amplitude. With the initial perturbation of 10% of the shock strength and with same grid resolution, the waves pass each other without interacting as predicted by GSD. Though an increase in the spike of the Mach number is observed when both the waves interact with each other, a thorough attention to the study of this would be required in 3-D case where the turbulent boundary along the side walls would give out waves along the shock.

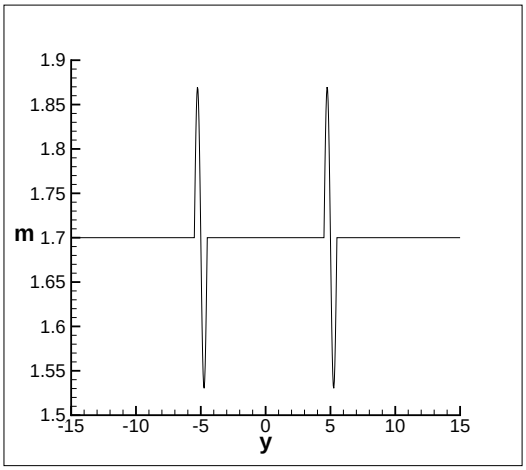

(a) Initial m distribution along the shock front depicting two vortex interacting with the shock

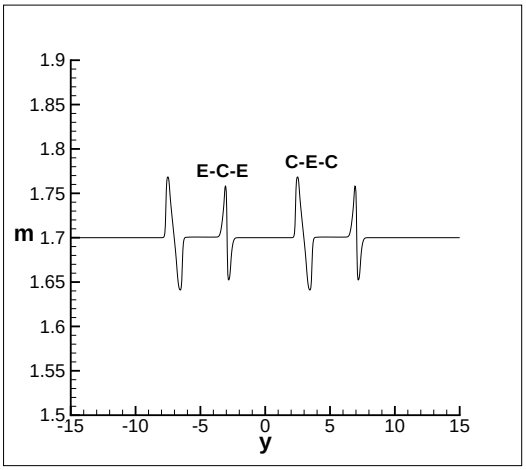

(b) m distribution showing the development of waves belonging to each vortex

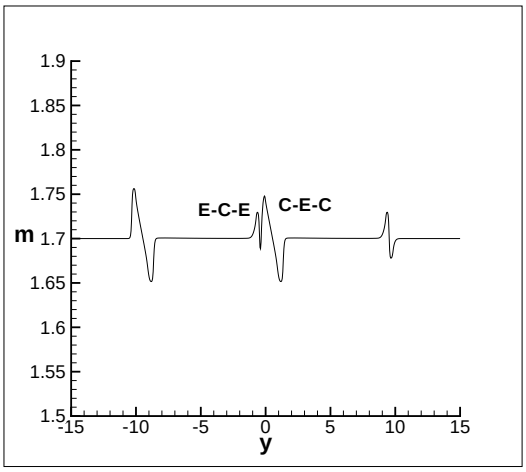

(c) m distribution with the E-C-E and C-E-C wave start interacting

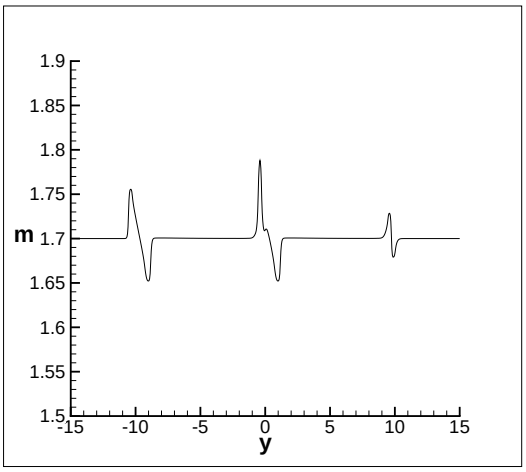

(d) m distribution with E-C-E wave merging with C-E-C wave

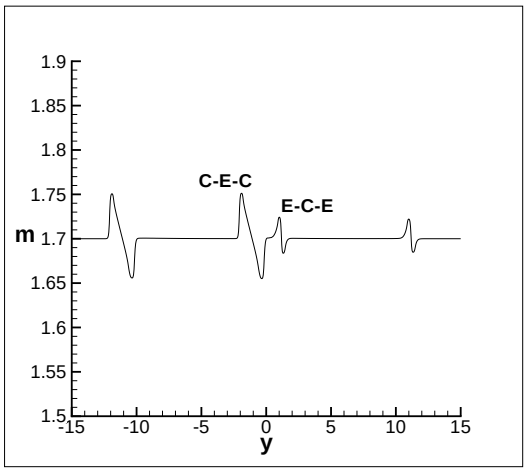

(e) m distribution after the waves have interacted

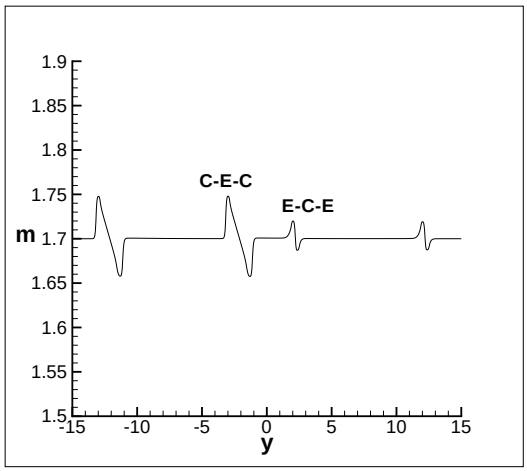

(f) m distribution at later time once the waves passes through each other retaining their nature

Figure 2.25: GSD results : Interaction of C-E-C and E-C-E waves using Roe's Area model

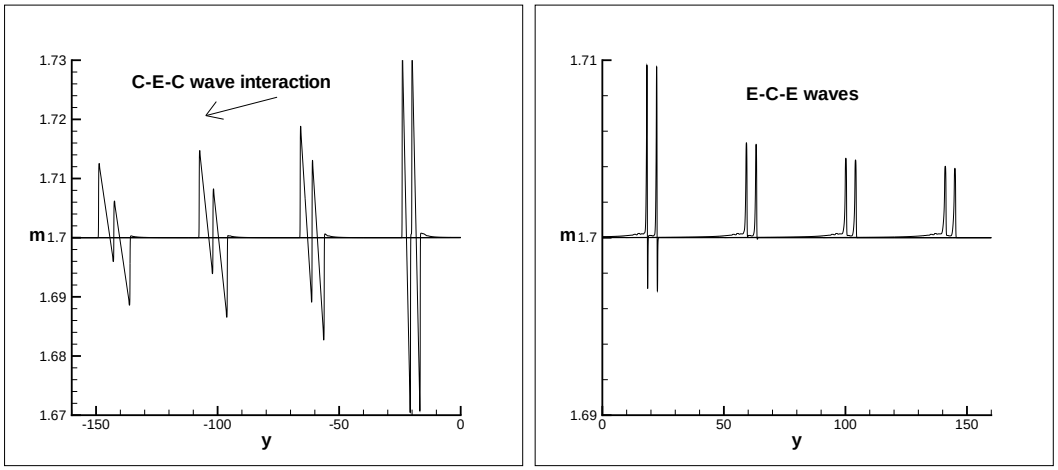

(a) Left going C-E-C wave interaction (b) Right going E-C-E waves

Figure 2.26: GSD results : Long range behavior of two vortex interaction

Long range behavior

To study the long range behavior the initial conditions are chosen similar to the previous interaction but having two perturbation separated by 16 r_v units. We observe the two left running C-E-C waves merge into each other consisting of an E-C-E wave structure in-between two compressions along the ends. The results are shown in the figure 2.26. The two compression waves at the end would decay at $t^{-\frac{1}{2}}$ where as the intermediate E-C-E wave would decay at t^{-1} if they are symmetrical otherwise the behavior is as described in Appendix C. In the long range behavior all N waves will merge to form a single N wave. The behavior of C-E-C waves explains the decay in the amplitude and frequency of oscillations shown in figure 1.3.

With this information from 2-D GSD on the nature of waves obtained and their power law decays, discussions on the results obtained from the study of shock-vortex interaction using Euler computations is done in the next chapter.

CHAPTER III

Shock-vortex Interaction

3.1 Numerical studies

On similar lines of Grasso and Pirozolli [13] and Ellzey and Henneke [10], we have performed numerical studies of the shock following interaction with a vortex. We have solved the 2D Euler equations initialized with a standing planar shock and a point vortex placed in the upstream flow field on a rectangular cartesian domain. We used vortices with two different velocity profiles. This was done to check that qualitative features of the flow did not depend on the details of the vortex structure. The two velocity profiles considered are given as follows

Vortex I - Rankine vortex A Rankine vortex consists of an inner core with solid body rotation 3.1 and an outer region 3.2

$$v_\theta = \frac{v_{max} r}{r_v}, \quad 0 < r < r_v \tag{3.1}$$

$$v_\theta = Ar + \frac{B}{r}, \quad r_v < r < r_o \tag{3.2}$$

The constants A and B in 3.2 are computed such that the velocity matches v_{max} at r_v and is zero at r_o. The overall circulation of the vortex is zero and the pressure field is specified such that pressure gradient provides the centripetal force. The density was

taken to be constant.

$$\frac{dP}{dr} = \frac{\rho v_\theta^2}{r} \tag{3.3}$$

Vortex II - Isentropic vortex A isentropic vortex was chosen such the the velocity field and the pressure field given by

$$u(x,y) = -\frac{K\bar{y}e^{\frac{\alpha(1-\bar{r^2})}{2}}}{2\pi} \tag{3.4}$$

$$v(x,y) = \frac{K\bar{x}e^{\frac{\alpha(1-\bar{r^2})}{2}}}{2\pi} \tag{3.5}$$

$$\frac{P}{P_\infty} = (1 - \frac{K^2(\gamma-1)e^{\alpha(1-\bar{r^2})}}{8\pi^2\alpha a_\infty})^{\frac{\gamma}{\gamma-1}} \tag{3.6}$$

$$\frac{\rho}{\rho_\infty} = (\frac{P}{P_\infty})^{\frac{1}{\gamma}} \tag{3.7}$$

with K relating to vortex perturbation strength and α the parameter deciding the rate of decay of the velocity to the far field value,a_∞ the free stream speed of sound and P_∞ representing the free stream pressure. The two velocity profiles are shown in the figure 3.1. Rankine vortex with two different outer vortex radius r_o are also used to study the effect of different interaction time in the results considered.

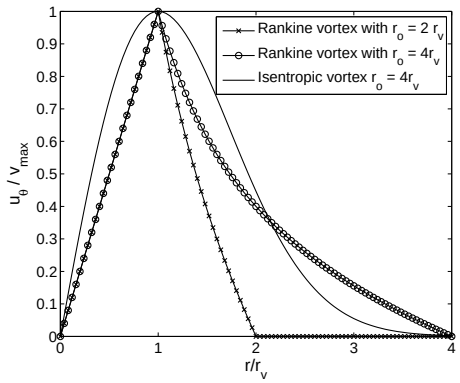

Figure 3.1: Tangential velocity profiles for both the composite and isentropic vortex

The schematic setup of the computational domain is given in figure 3.2. The vortex

core is defined as the inner part of the vortex where the velocity reaches maximum v_{max}. This radius r_v is taken to be the reference length. A square cartesian mesh of 250x750 cells is set up with a stationary shock located halfway between the two long vertical sides along the y-axis. Initially the vortex is placed at a distance of $6r_v$ units away from the normal shock. The vortex gets convected with the freestream and then interacts with the shock. All the computations are done using dimensionless variables and the speed of sound and pressure are taken to be unity along upstream. The strength of the shock is given by the upstream Mach number M_s. The vortex strength is given by the Mach number M_v which is the ratio of the maximum vortex velocity v_{max} to the freestream sound speed. 25 cells are taken inside the vortex core for grid convergence(though the results are not quite grid converged we are confident that refining the grids will not affect our conclusions).

The 2D Euler equations are solved using Hancock predictor corrector time stepping method [12] and Roe's linearized Riemann solver [29] for computation of the fluxes, using double min-mod limiter for reconstruction. The time-step is chosen so the that CFL number lies between 0.3 to 0.5. Non Reflective boundary conditions are employed all along the boundaries. Solution is computed till the time when the perturbation along the shock leaves the domain. The vortex leaves the subsonic part of the domain much earlier than the computational time considered. The shock is aligned along the y axis and the vortex center lies along the x axis with vortex moving from left to right.

The fluid properties are extracted at 5 cells downstream of the initial shock along line AB shown in figure 3.2, to observe the changes in shock strength(since capturing the exact shock shape change and its strength from the results is tedious because of the finite number of cells the shock occupies in the numerical computation). The pressure signal and the change in the flow angle are monitored along the line AB.

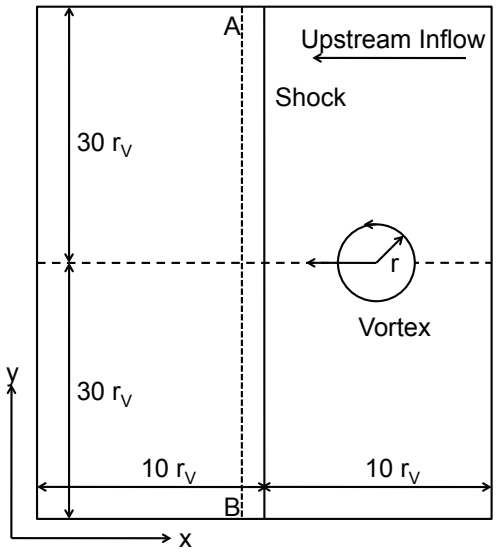

Figure 3.2: Computational domain for the shock vortex interaction.

3.2 Discussion on Numerical errors

In the computational experiments consider the impact of numerical errors on the measurements we are making especially on the wave propagation.

- Finite volume computation is prone to numerical dissipation and it needs to be quantified based on the grid resolution and the CFL condition. A mesh of 50 cells per unit dimension along AB and the CFL number for the computation between 0.3 and 0.6 is chosen to reduce the effect of numerical viscosity. Predicting a moving vortex involves convective errors and numerical dissipation. It is based on the grid resolution inside the vortex core. The same resolution is adapted as in [13] and 25 cells per vortex core is considered for both vortex types. The Rankine vortex diffuses more than the isentropic vortex for the same resolution because of the presence of discontinuity in the velocity profile(fig 3.3(b)). The enstrophy of the vortex was measured by convecting the vortex in the free stream for 20 r_v units(fig 3.3).

- The effect of boundary conditions along the sub-sonic part of the flow, though

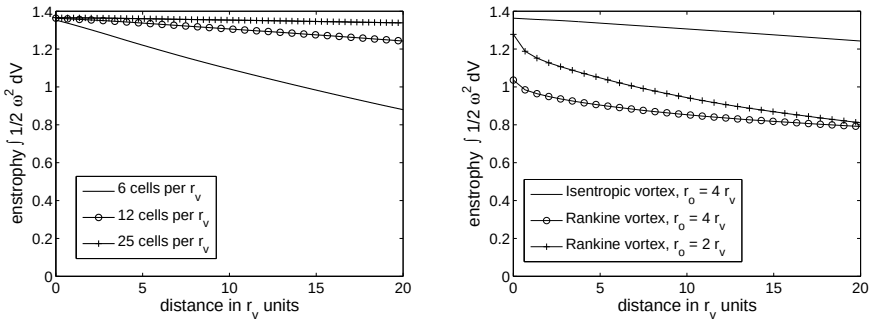

(a) Isentropic vortex with different grid resolution

(b) Comparison of vortex diffusion for the chosen grid resolution of 12 cells per r_v

Figure 3.3: Plot of enstrophy to measure numerical dissipation of the vortex

we have taken non reflective boundary conditions there are still some waves that are transmitted back to the flow domain as the vortex passes out of the domain. We have compared the solutions in terms of the decay rates of the waves by increasing the sub-sonic part of the domain to $20r_v$ units and found the decay rates to be unaffected.

- Capturing stationary shocks numerically involves the well known carbuncle phenomenon [26]. These are numerical instability of the shocks occurring at higher Mach numbers. In our experiments the shocks with strengths $M_s = 1.7$ and 2.0 give rise to spurious oscillations in the flowfield over time. These oscillations pose restriction on the space time domain till which the wave propagation can be monitored. To compensate for it, dissipation of 15% and 25%($M_s =$ 1.7 and 2.0 respectively) of the maximum acoustic wave speed is added to the flux coming from the wave speed pertaining to the contact discontinuity in the y direction[21]. This reduces the noise occurring in the measurement of the pressure signal because of carbuncle and delays its appearance in the computed solution.

- The pressure signal was monitored 5 cells downstream of the undisturbed shock position. The pressure signal was monitored over a set of cell locations away

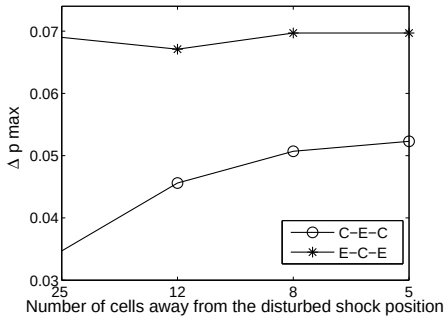

Figure 3.4: Pressure convergence with moving AB closer to the undisturbed shock position

from the undisturbed shock position. To measure the decay rates, amplitude of the waves were measured $6r_v$ units away both above and below the point of shock vortex interaction along AB. The location of AB, 5 cells downstream was chosen based on the convergence of the maximum pressure captured along AB. The maximum of the C-E-C and the E-C-E wave observed(with respect to the undisturbed downstream pressure) by changing the monitor location AB is plotted for the case of $M_s = 1.4$ and $M_v = 0.4$ in figure 3.4.

3.3 Results and Discussion

3.3.1 Short times

Here we compare our results with those of Grasso and Pirozolli [13] who observed the near field behavior of the interactions and labeled them as

- weak interaction - one that leaves the shock front smooth
- strong interaction - one that develops kink along the shock. The nature of the kink is further classified as
  - Regular reflection
  - Mach reflection

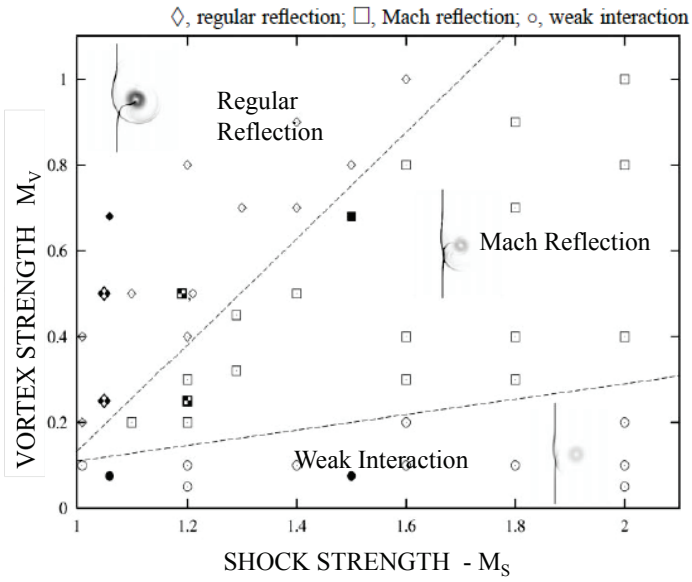

Figure 3.5: Shock vortex interaction map[13]. Hollow symbols, Grasso and Pirozolli [13]; filled symbols ,Ellzey *etal*. [10]; half-filled symbols, Inoue and Hattori [15]

The parameters of the problem are the vortex Mach number (M_v) and the shock strength(M_s). The detailed structure of the flow field downstream of the shock are described in [13] as well as [15]. When the shock interacts with a vortex, the interaction shows a complex structure consisting of both reflected and diffracted shocks. The diffraction occurs to the half of the shock which gets pushed upstream and the reflection occurs to the half of the shock which is pushed downstream. Their classification is based on shock distortion in the near field and the topology for the classification of interaction is given in figure 3.5. Our interactions have not been indicated in the figure but do span all the three regions of the shock-vortex interaction map.

Our Observation

In our computations we have considered an anti clockwise rotating vortex so that the top half of the vortex pushes the shock downstream and the other half of the vortex pulls it upstream. In the interaction, pressure field is symmetrical on the top and bottom half of the vortex whereas the velocity fields are not so, the top half

aiding the velocity upstream with the bottom half opposing the upstream velocity. The interaction being non linear causes two different kinds of disturbance to propagate along the shock. The disturbance caused by the interaction travels along the shock both upwards and downwards from the region of interaction.

The strength of the shock is related to the pressure disturbance monitored along the line AB shown in figure 3.2 and the shock shape change is observed by the change in the flow angle.

After the initial period of interaction there was little visible distortion of the shock in the contour plots. This may have misled some authors into assuming that the waves decay too rapidly to need consideration. We observe two different wave structures(pressure signal along AB) propagating along the shock. A wave system comprising compression-expansion-compression (C-E-C) propagates in one direction, and a system comprising expansion-compression-expansion (E-C-E) in the other. The shock undergoes either regular reflection or Mach reflection along the half of the shock that pushes the shock downstream which carries the E-C-E wave structure and the shock exhibits diffraction along the half that is pulled upstream by the vortex which carries the C-E-C wave structure.

We calculated a variety of cases and studied them both from the viewpoint of near field shock distortion and far field wave propagation. The near field study is simply to confirm our calculations by verifying that they conform to the classifications of Grasso and Pirozolli [13]. We now present results for a few of these interactions.

3.3.2 Case 1 : Weak shock with $M_s = 1.05$

First for the case of a normal weak shock with strength of $M_s = 1.05$ is subjected to vortices with three different strengths of $M_v = 0.1$, 0.5 and 1.0. Both types of vortices are used. Two Rankine vortices with $r_o = 2r_v$ and $r_o = 4r_v$ are considered. For vortices with $r_o = 4r_v$, the vortex hits the shock at t = 0.4762 units.

The vortex pushes the top half of the shock and pulls the bottom half of the shock giving quite a smooth perturbation for weak vortex strength $M_v = 0.1$(refer figure 3.6). When the vortex strength is increased to $M_v = 0.5$ the structure of shock undergoes a different pattern as can be seen in figure 3.7. The crossed shocks above the vortex were described in [13] as a regular reflection pattern. The same pattern is observed for $M_v = 1.0$. Qualitatively similar results are observed for both types of vortices and also for both the composite vortices considered. The results for isentropic vortex is presented unless otherwise stated. The near field shock distortions conform to the classifications of Grasso and Pirozolli [13].

The nature of the waves at a later time for these three different vortex strengths is shown in figure 3.8 and 3.9. In every case the pattern of C-E-C and E-C-E waves develops, although not so cleanly for stronger vortices. The histories of the wave amplitudes are shown in figure 3.10. The change in pressure signal downstream(Δp) is normalized with the pressure difference observed between the freestream and the vortex core(Δp_v). The decay of the waves are plotted with reference decay slope between $t^{(-1/2)}$ and $t^{(-2)}$. The flow angle shows similar behavior as the one followed by the pressure signal(figure 3.8).

Although the features of the waves correspond quite closely to the predictions of the simple theories, most of the decay rates are roughly proportional to t^{-1} or even t^{-2} rather than $t^{\frac{-1}{2}}$. In these cases the waves decay quite quickly.

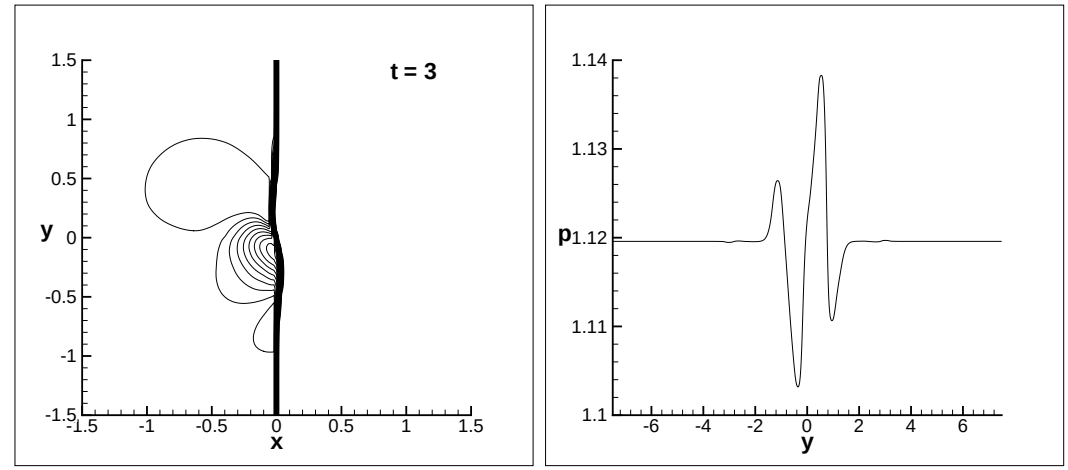

(a) (b)

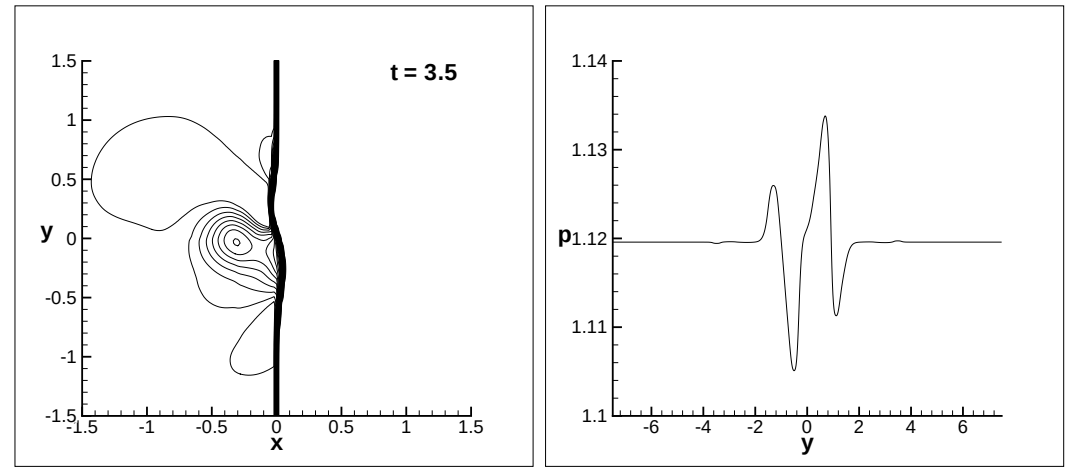

(c) (d)

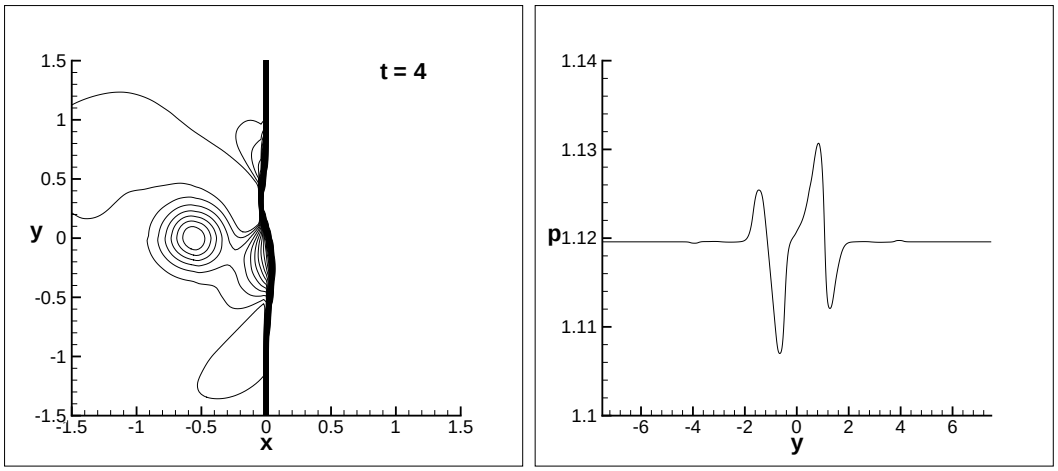

(e) (f)

Figure 3.6: Weak Interaction : Time evolution of the pressure field showing the change in the shock structure for $M_s = 1.05$ and $M_v = 0.1$ with Contour levels - 24 levels from 1.05 to 1.117 in the left side and the monitored pressure signal on the right

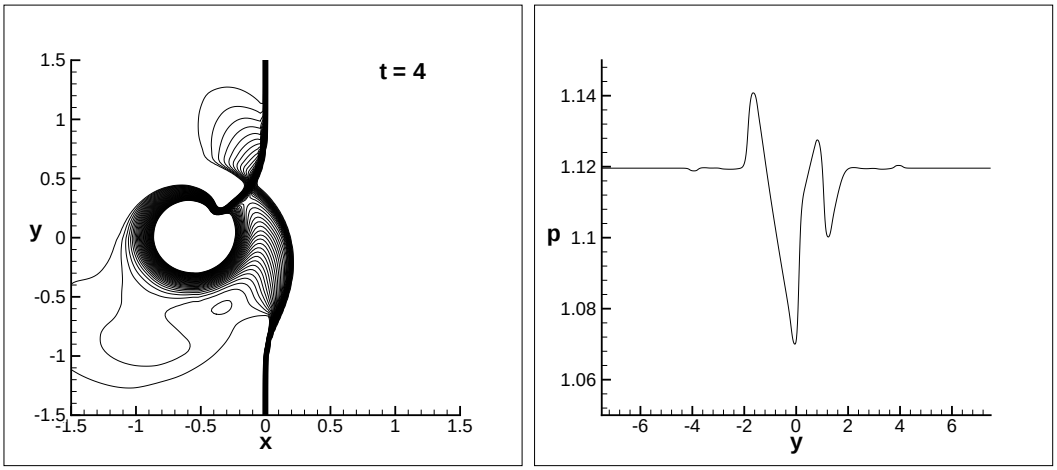

(a) (b)

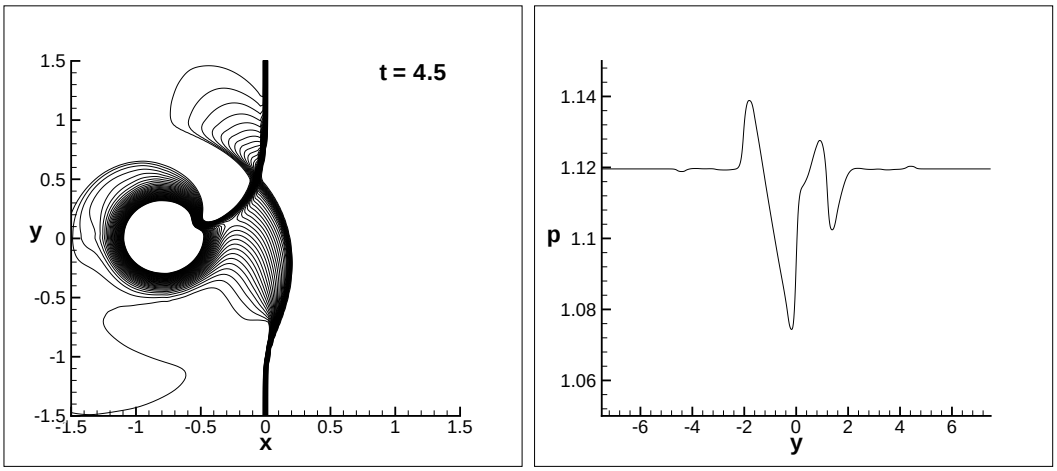

(c) (d)

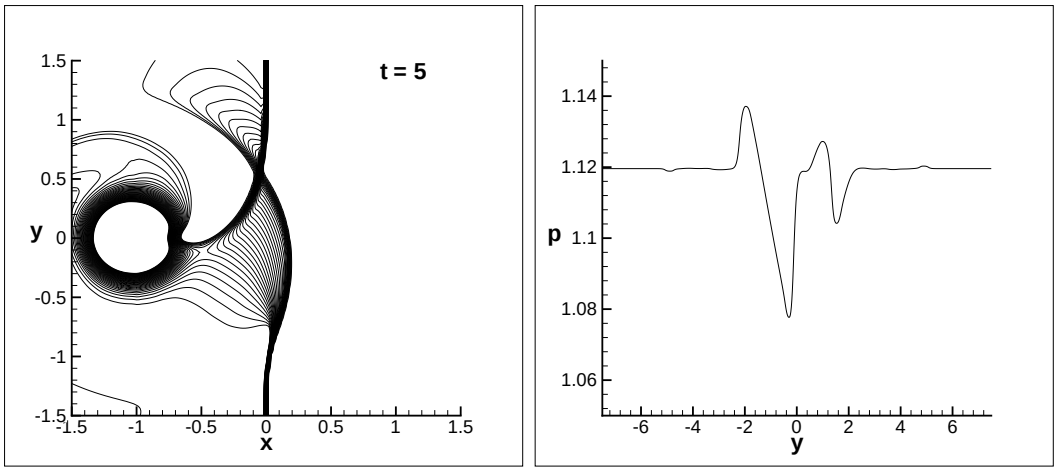

(e) (f)

Figure 3.7: Time evolution of the pressure field showing Regular reflection pattern in the shock structure for $M_s = 1.05$ and $M_v = 0.5$, Contour levels - 36 levels from 1.01 to 1.117.The plots on the right side indicate the pressure signal monitored

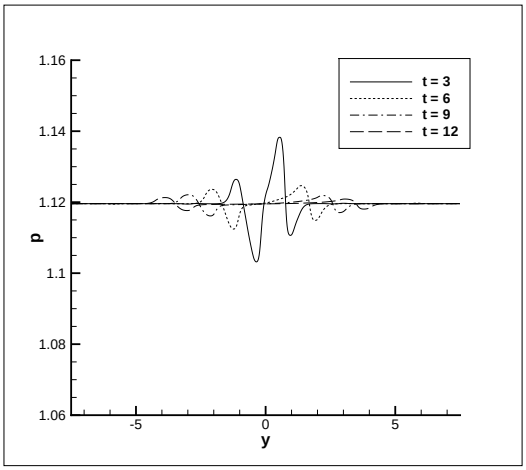

(a) snapshot of the pressure signal at various time intervals for $M_v = 0.1$

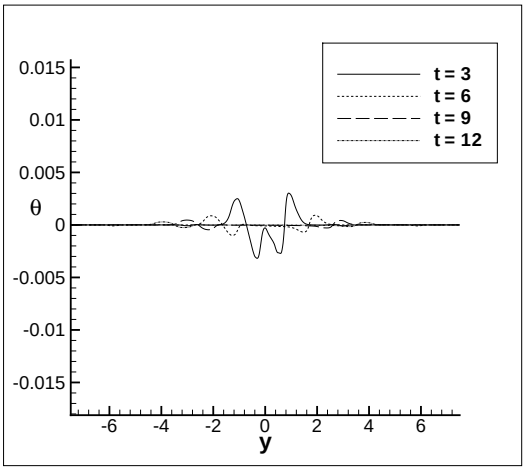

(b) snapshot of flow angle at various time intervals for $M_v = 0.1$

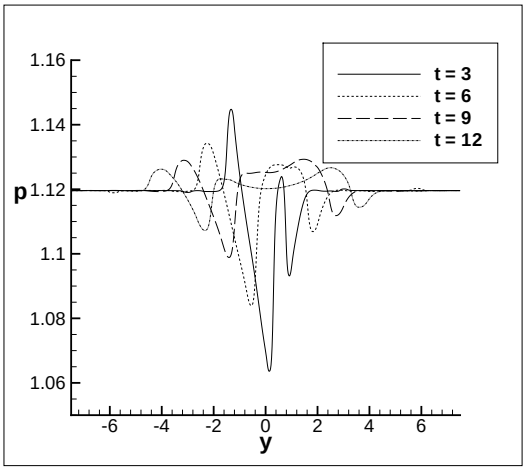

(c) snapshot of the pressure signal at various time intervals $M_v = 0.5$

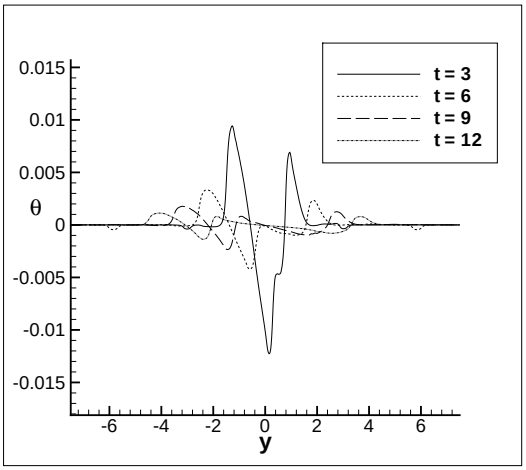

(d) snapshot of flow angle at various time intervals $M_v = 0.5$

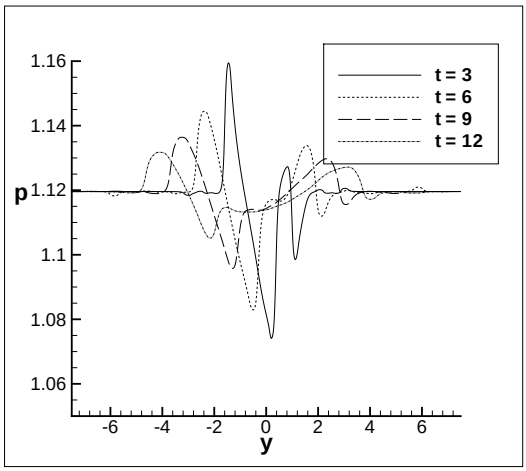

(e) snapshot of the pressure signal at various time intervals $M_v = 1.0$

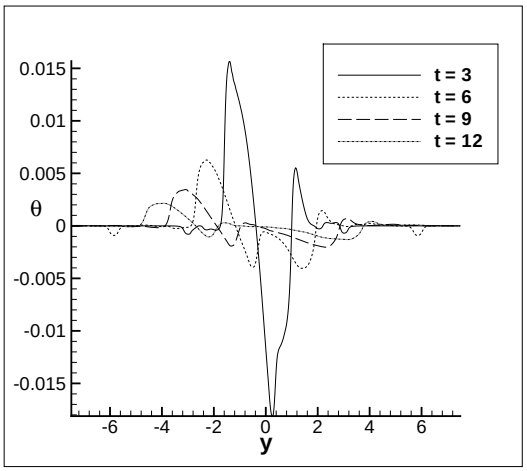

(f) snapshot of flow angle at various time intervals $M_v = 1.0$

Figure 3.8: Pressure disturbance and flow angle change monitored along AB for shock strength $M_s = 1.05$

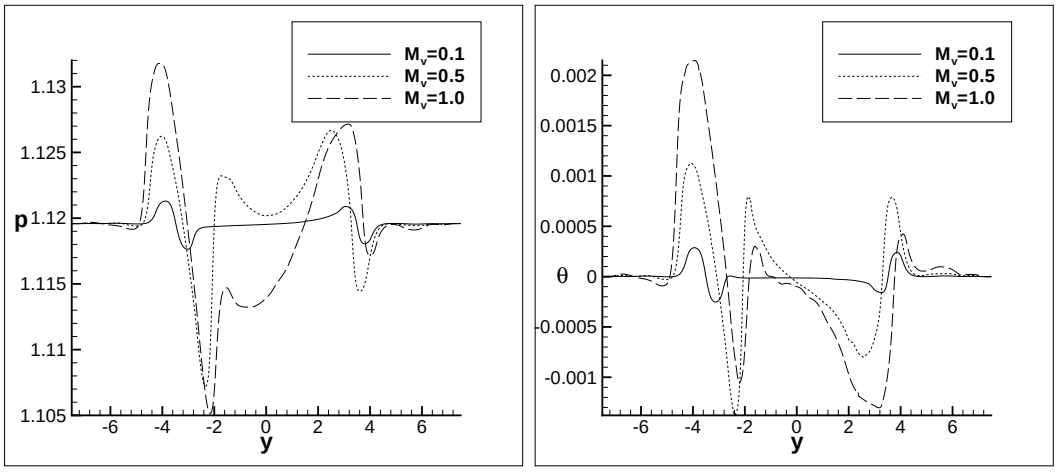

(a) snapshot of the pressure signal with varying vortex strengths

(b) snapshot of flow angle with varying vortex strengths

Figure 3.9: Pressure disturbance and flow angle change monitored along AB for shock strength $M_s = 1.05$ and vortex strengths $M_v = 0.1$, 0.5 and 1.0 after t = 12 units.

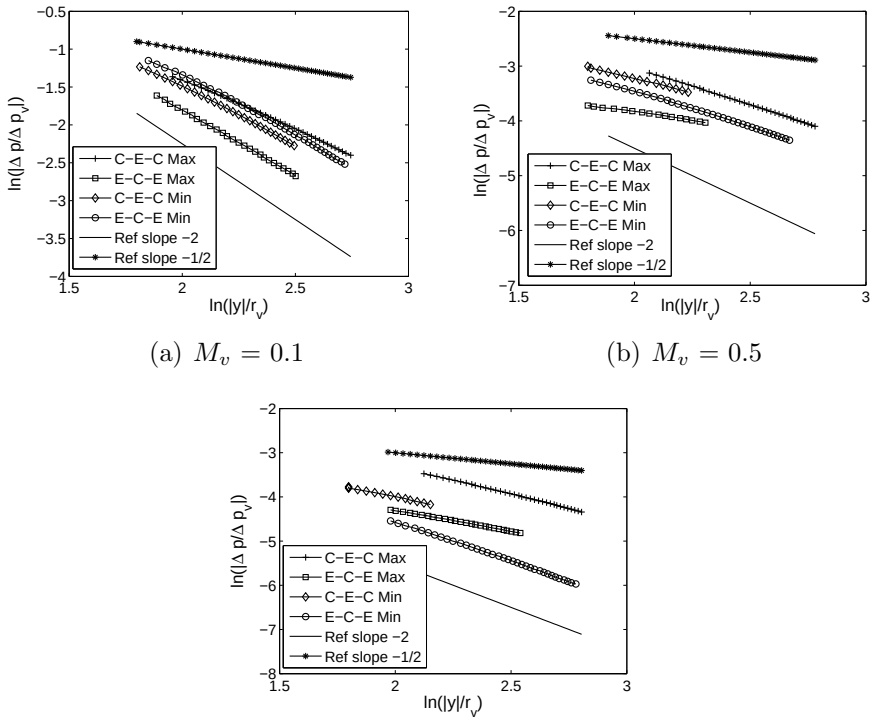

(a) $M_v = 0.1$

(b) $M_v = 0.5$

(c) $M_v = 1.0$

Figure 3.10: Power law decay of amplitudes of the pressure signal for $M_s = 1.05$.

3.3.3 Case 2 : $M_s = 1.4$

Here a normal shock with strength of $M_s = 1.4$ is subjected to both type of vortices with four different strengths of $M_v = 0.1$, 0.2,0.4 and 0.8. For the isentropic vortex and composite vortex with $r_o = 4r_v$ the interaction starts at t = 0.357 units.

Weak interaction is observed for $M_v = 0.1$ and 0.2. When the vortex strength is increased to $M_v = 0.8$ the structure of shock undergoes a pattern of Regular reflection as observed for $M_s = 1.05$, but at later times the Regular reflection transitions to Mach reflection pattern. Only Mach reflection is observed for $M_v = 0.4$. This is shown in the figures 3.11 and 3.12. Qualitatively similar results are observed for both types of vortices and also for both the composite vortices considered. The near field shock distortions conform to the classifications of Grasso and Pirozolli [13].

Irrespective of whether the shock undergoes Regular reflection or Mach reflection formation of C-E-C and E-C-E wave structures are observed. The decay rates are roughly proportional to t^{-1} or even t^{-2} rather than $t^{\frac{-1}{2}}$. In these cases also the waves decay quite quickly.

A similar results were obtained for shock with strength $M_s = 1.2$ and are not presented.

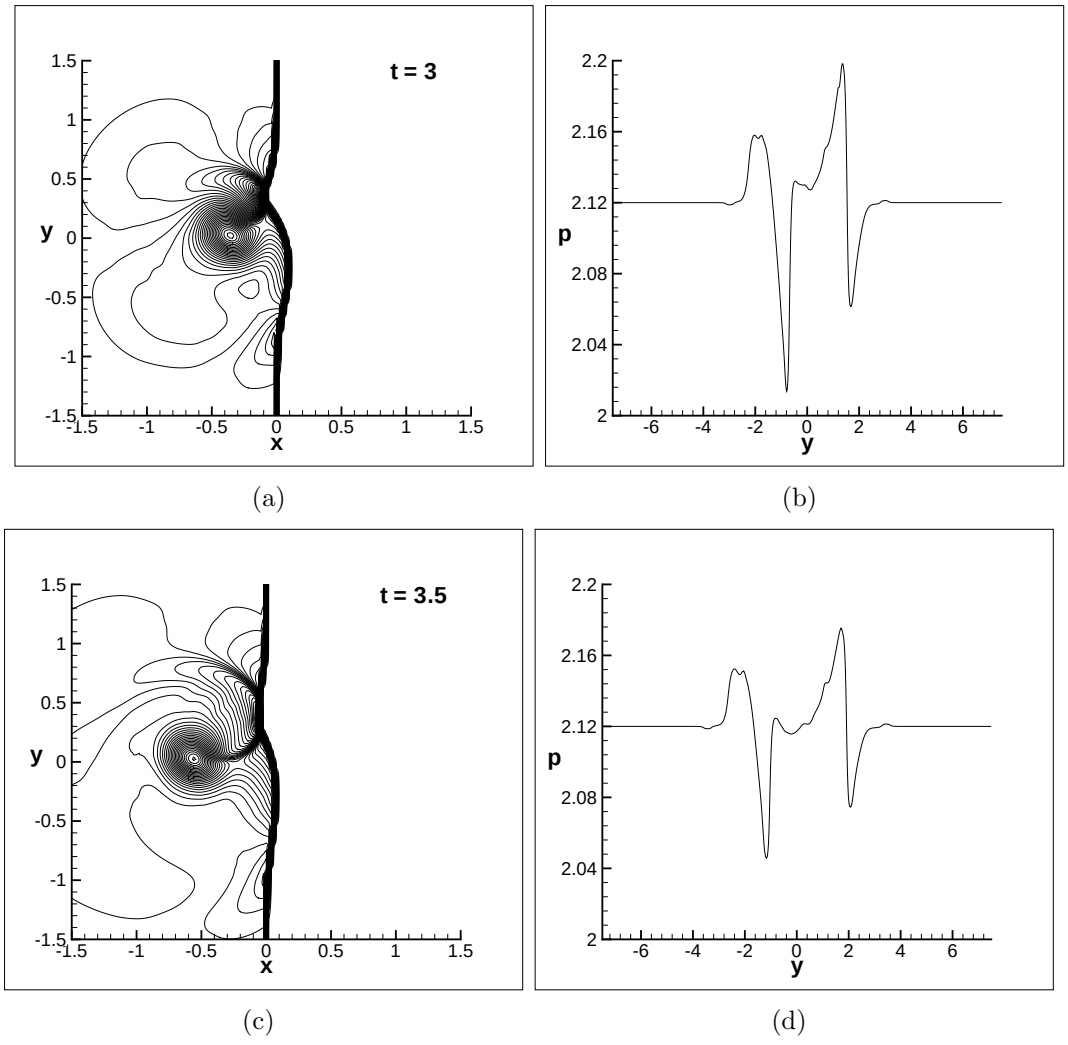

Figure 3.11: Time evolution of the pressure field showing Mach Reflection in the shock structure for $M_s = 1.4$ and $M_v = 0.4$, Contour levels - 64 levels from 1.01 to 2.76. The plots on the right side indicate the pressure signal monitored

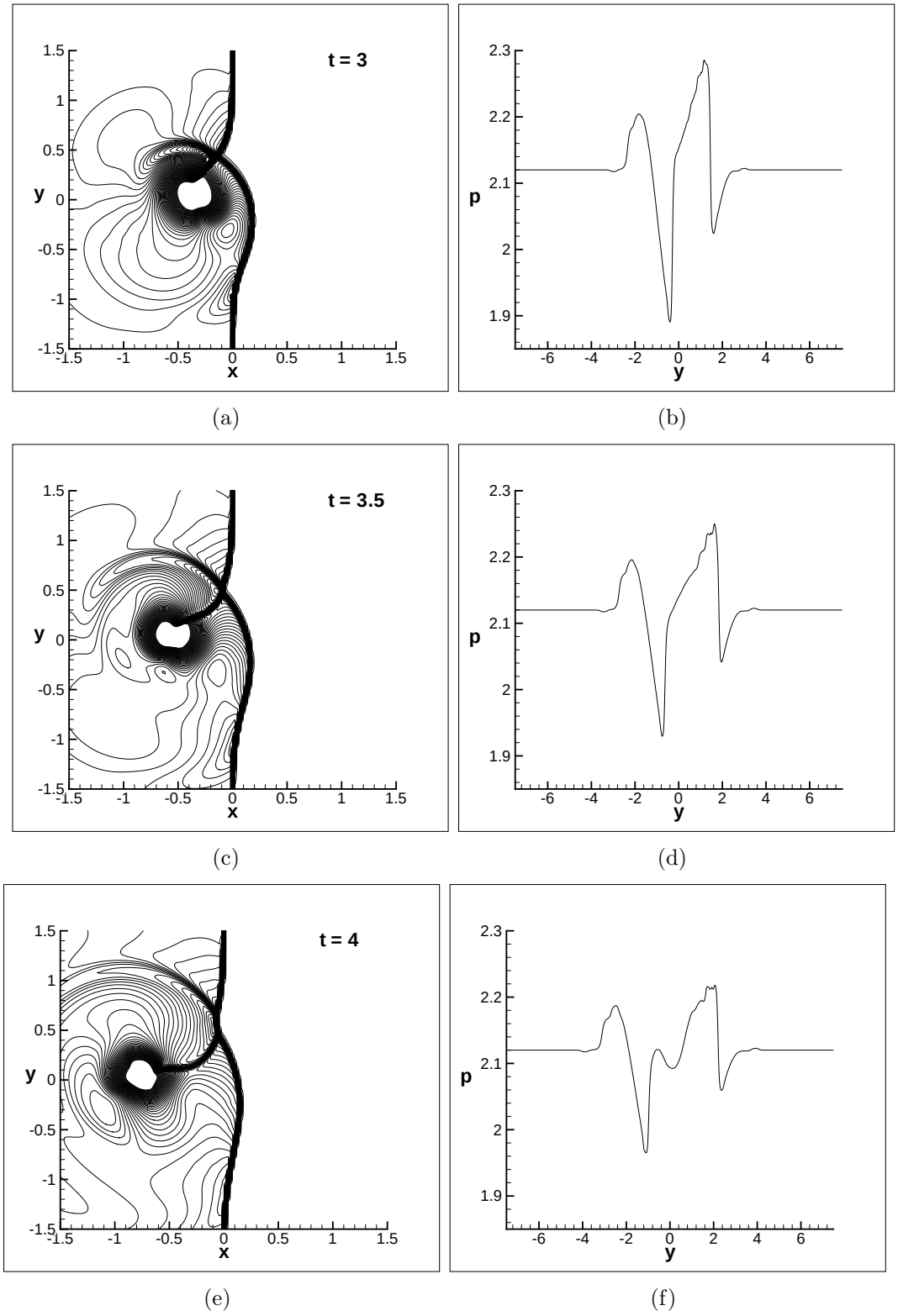

Figure 3.12: Time evolution of the pressure field showing transition from Regular reflection to Mach reflection in the shock structure for $M_s = 1.4$ and $M_v = 0.8$, Contour levels - 64 levels from 1.01 to 2.94. The plots on the right side indicate the pressure signal monitored

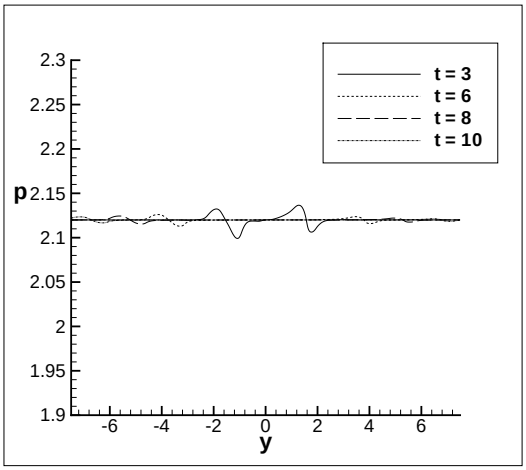

(a) snapshot of the pressure signal at various time intervals for $M_v = 0.1$

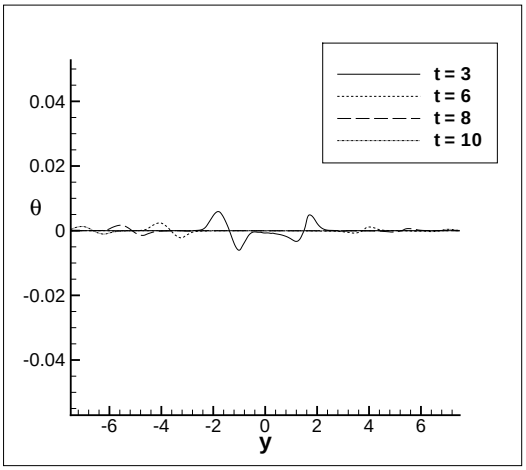

(b) snapshot of flow angle at various time intervals for $M_v = 0.1$

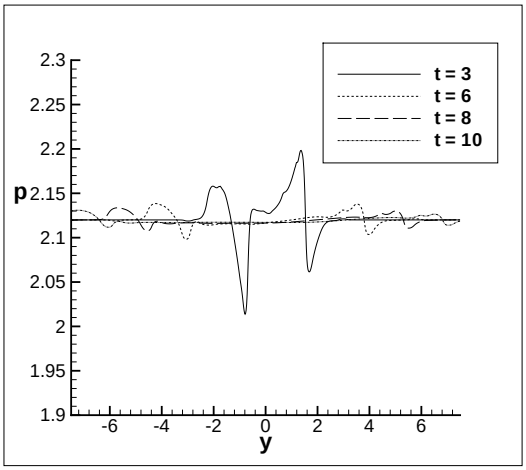

(c) snapshot of the pressure signal at various time intervals $M_v = 0.4$

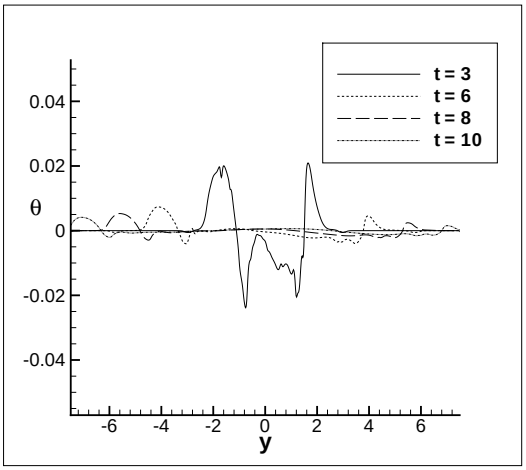

(d) snapshot of flow angle at various time intervals $M_v = 0.4$

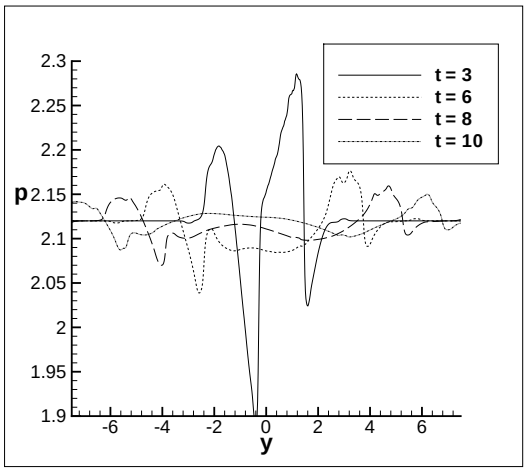

(e) snapshot of the pressure signal at various time intervals $M_v = 0.8$

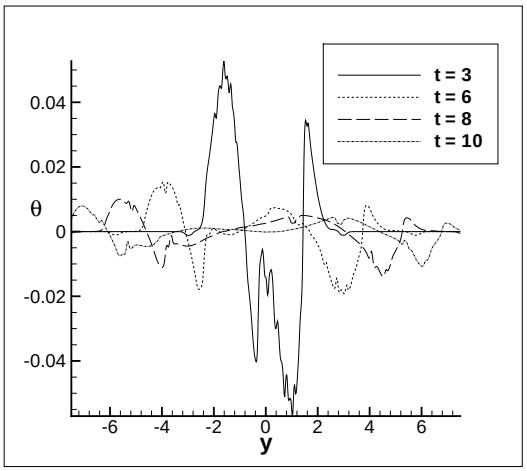

(f) snapshot of flow angle at various time intervals $M_v = 0.8$

Figure 3.13: Pressure disturbance and change in flow angle measured along AB for shock strength $M_s = 1.4$

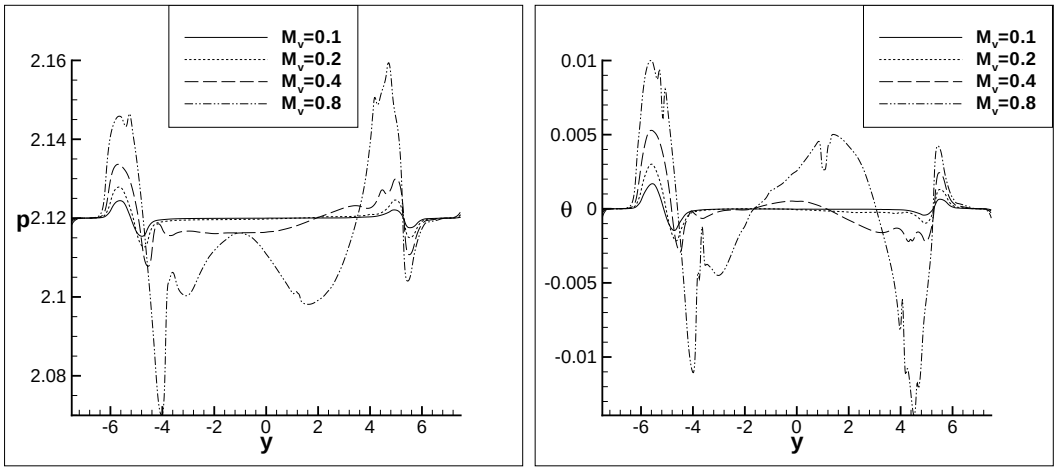

(a) snapshot of the pressure signal with varying vortex strengths

(b) snapshot of flow angle with varying vortex strengths

Figure 3.14: Pressure disturbance and change in flow angle measured along AB for shock strength $M_s = 1.4$ and vortex strengths $M_v = 0.1$, 0.2, 0.4 and 0.8 after t = 8 units

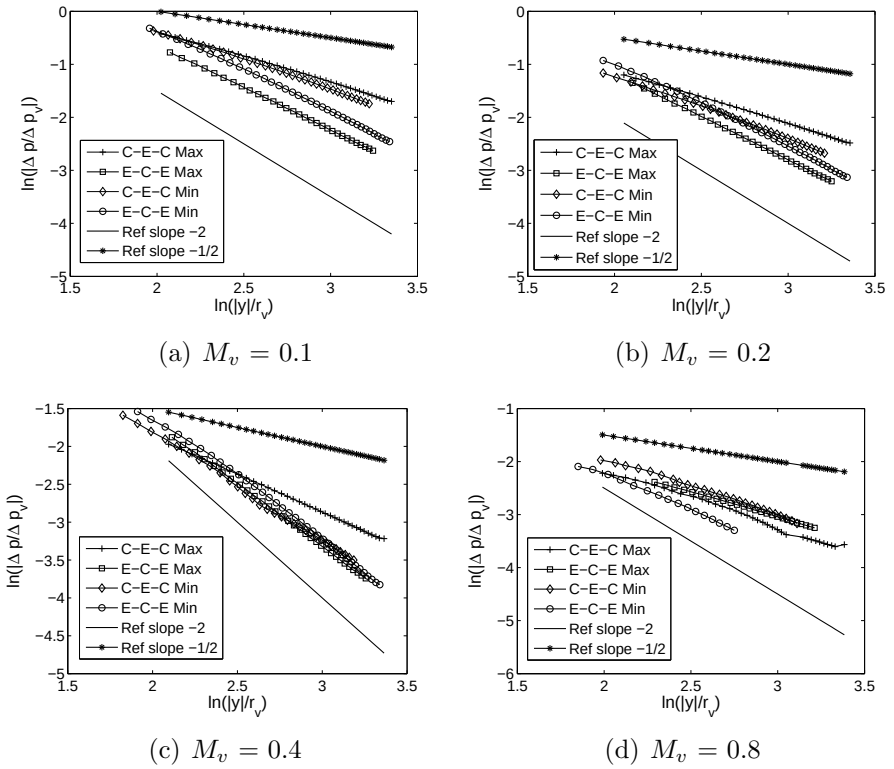

(a) $M_v = 0.1$

(b) $M_v = 0.2$

(c) $M_v = 0.4$

(d) $M_v = 0.8$

Figure 3.15: Power law decay of amplitudes of the pressure signal for $M_s = 1.4$.

3.3.4 Case 4 : $M_s = 1.7$

Again the same two types of vortices are used with four different strengths of $M_v = 0.1$, 0.2,0.4 and 0.8. Two composite vortices with different outer radii $r_o = 2r_v$ and $r_o = 4r_v$ are also considered. The upstream vortex interaction starts at t = 0.294 units for the isentropic vortex and composite vortex with $r_o = 4r_v$.

The interactions considered here come under weak interaction and Mach reflection with no regular reflection of the shock observed. This again follows the classification of Grasso and Pirozolli [13].

The pressure signal with varying vortex strengths for all the vortices are plotted in figures 3.17,3.18 and 3.19. The isentropic vortex and the composite vortex with same outer radius show almost similar wave structure. The C-E-C wave type shows a transition to the classical N wave whereas for the composite vortex with lesser outer radii a more clear N wave type pattern is observed. This is because more information is distributed along the shock because of higher interaction time in case of isentropic and composite vortex of the same outer radius. We can see qualitatively similar results for both types of vortices and also for both the composite vortices considered revealing the same nature of waves for any vortex structure. The decay profiles for composite vortex with $r_o = 2r_v$ shows a smooth decay and thus plotted.

The power law decay profiles indicate the decay of the C-E-C waves to follow closer to $t^{-1/2}$ for all the vortex strengths considered. For the case of isentropic vortex the C-E-C waves reaches the asymptotic limit and then starts decaying at $t^{-1/2}$.

The E-C-E waves decay at a faster rate of t^{-2} for lower vortex strengths. With increasing vortex strengths they show a shift towards slower decay as seen in figures 3.20 and 3.21.

The waves show slower decay rates of $t^{\frac{-1}{2}}$ especially for the C-E-C wave type for all the vortex strengths and E-C-E wave type for higher vortex strengths agreeing well with the predictions of GSD theory.

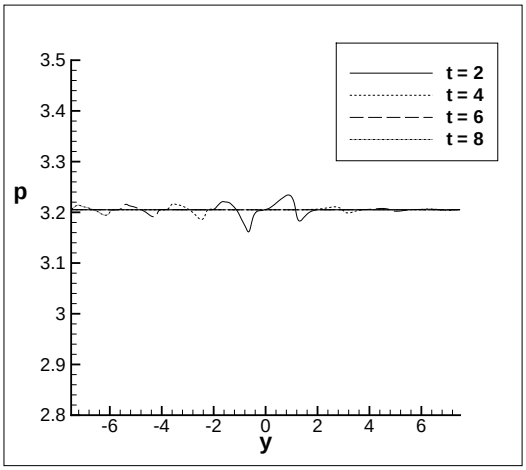

(a) snapshot of the pressure signal at various time intervals for $M_v = 0.1$

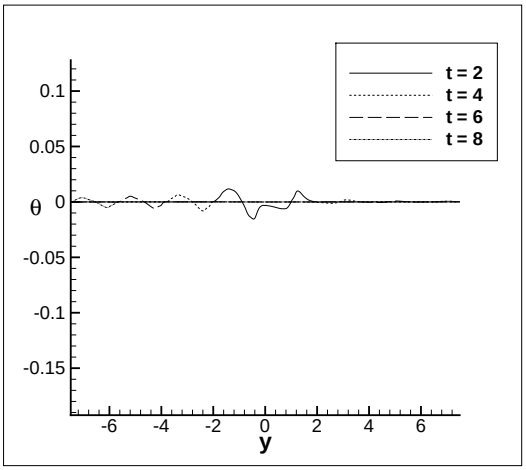

(b) snapshot of flow angle at various time intervals for $M_v = 0.1$

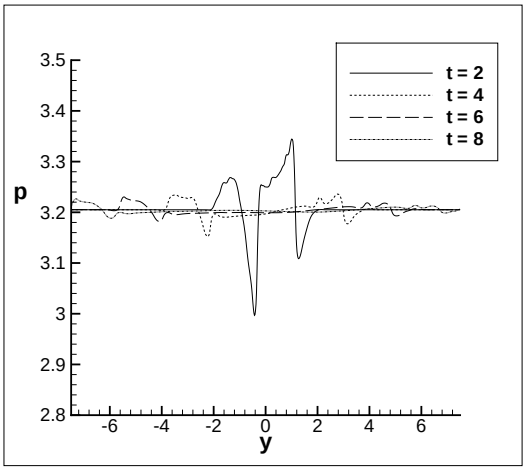

(c) snapshot of the pressure signal at various time intervals $M_v = 0.4$

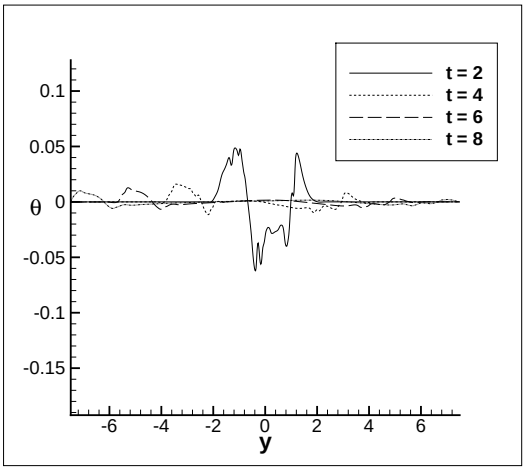

(d) snapshot of flow angle at various time intervals $M_v = 0.4$

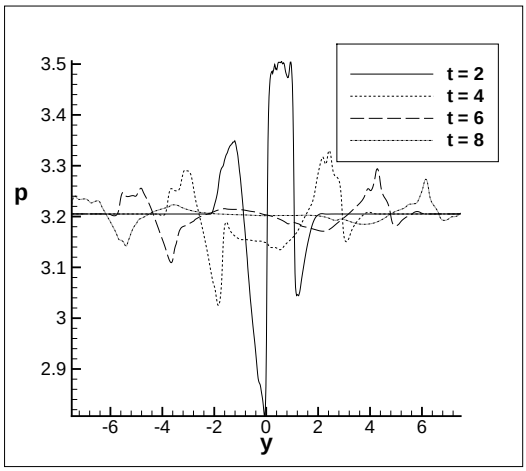

(e) snapshot of the pressure signal at various time intervals $M_v = 0.8$

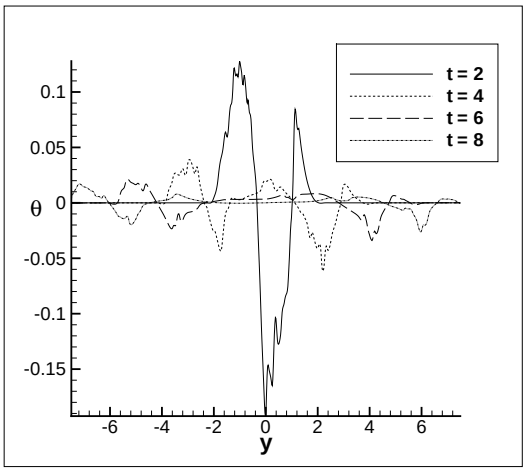

(f) snapshot of flow angle at various time intervals $M_v = 0.8$

Figure 3.16: Pressure disturbance and change in flow angle measured along AB for shock strength $M_s = 1.7$ and interaction with an isentropic vortex

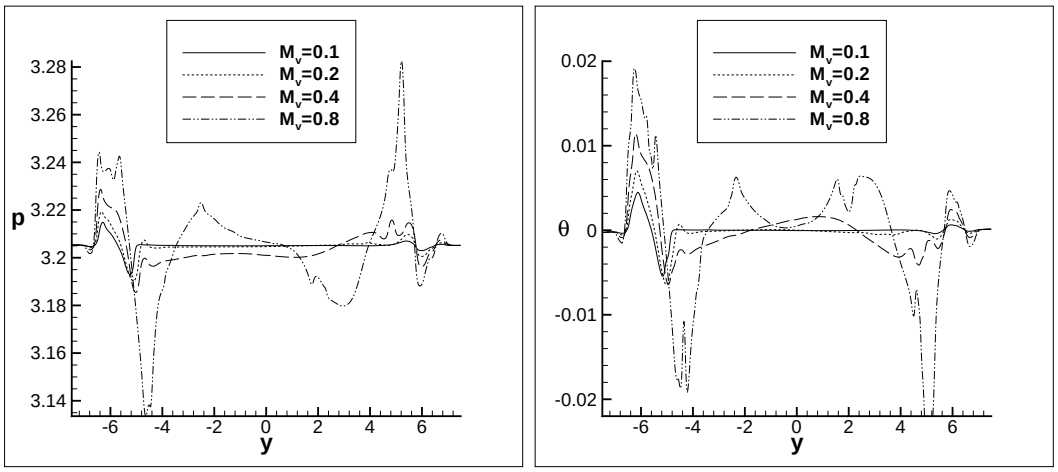

(a) snapshot of the pressure signal with varying vortex strengths

(b) snapshot of flow angle with varying vortex strengths

Figure 3.17: Pressure disturbance and change in flow angle measured along AB for shock strength $M_s = 1.7$ and vortex strengths $M_v = 0.1$, 0.2, 0.4 and 0.8 after t = 7 units

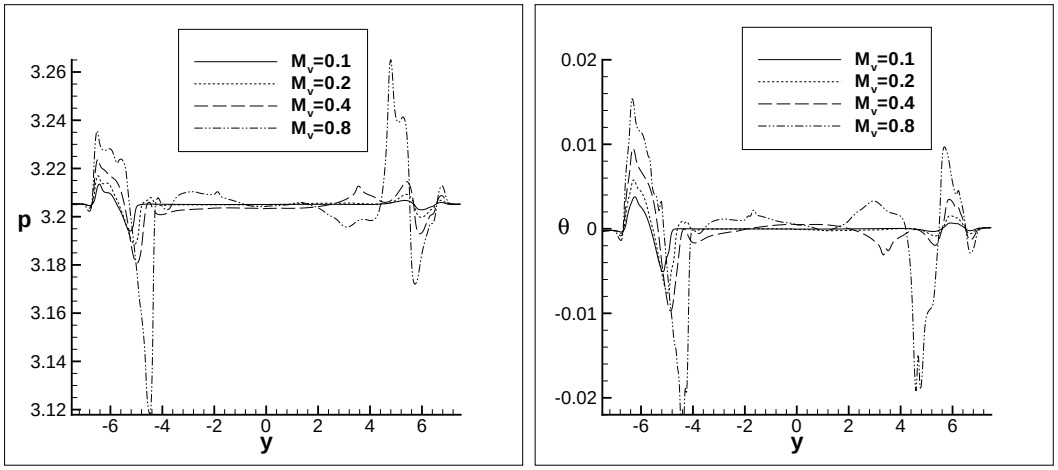

(a) snapshot of the pressure signal with varying vortex strengths

(b) snapshot of flow angle with varying vortex strengths

Figure 3.18: Pressure disturbance and change in flow angle measured along AB for shock strength $M_s = 1.7$ and composite vortex with strengths $M_v = 0.1$, 0.2, 0.4 and 0.8 and with $r_o = 4r_v$ after t = 7 units

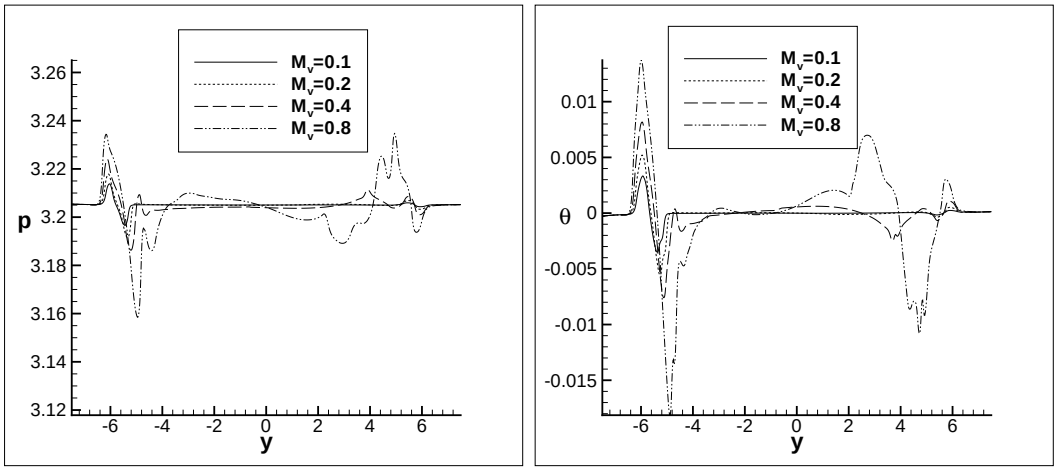

(a) snapshot of the pressure signal with varying vortex strengths

(b) snapshot of flow angle with varying vortex strengths

Figure 3.19: Pressure disturbance and change in flow angle measured along AB for shock strength $M_s = 1.7$ and composite vortex with $r_o = 2r_v$ and strengths $M_v = 0.1$, 0.2, 0.4 and 0.8 at t = 7 units

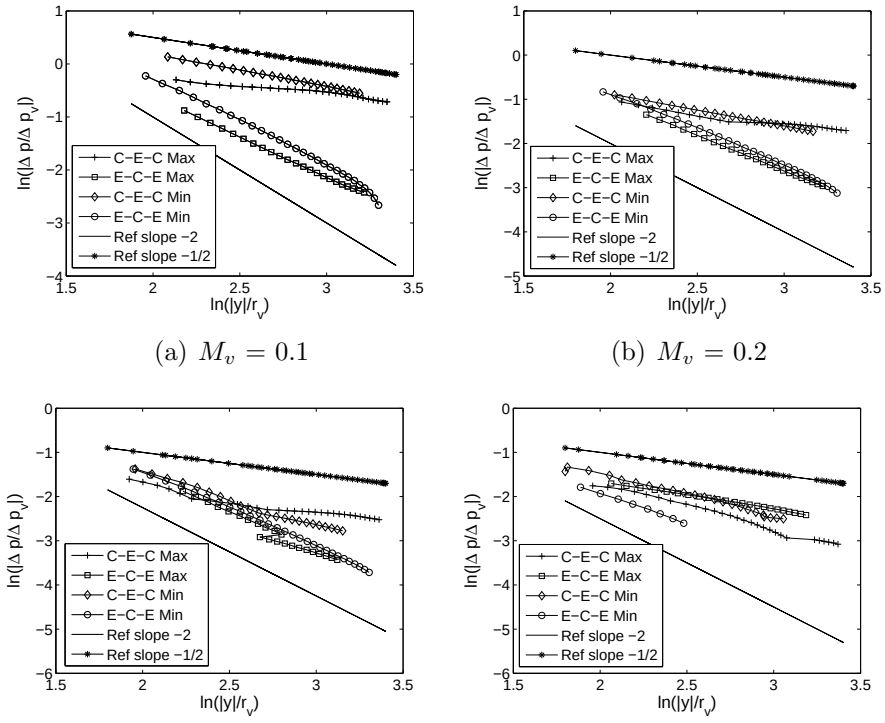

(a) $M_v = 0.1$

(b) $M_v = 0.2$

(c) $M_v = 0.4$

(d) $M_v = 0.8$

Figure 3.20: Power law decay of amplitudes of the pressure signal for $M_s = 1.7$ for an isentropic vortex

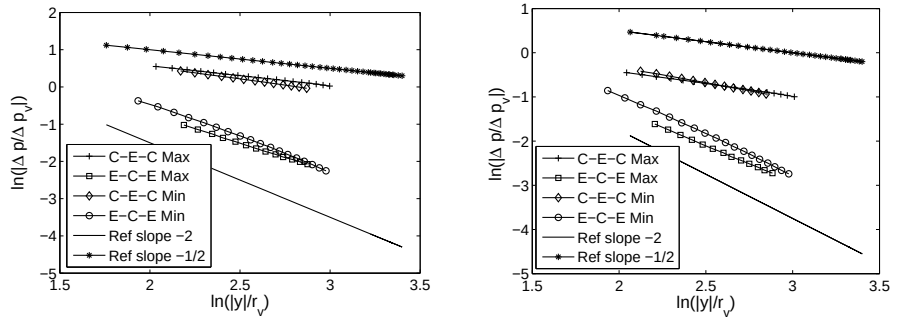

(a) $M_v = 0.1$ (b) $M_v = 0.2$

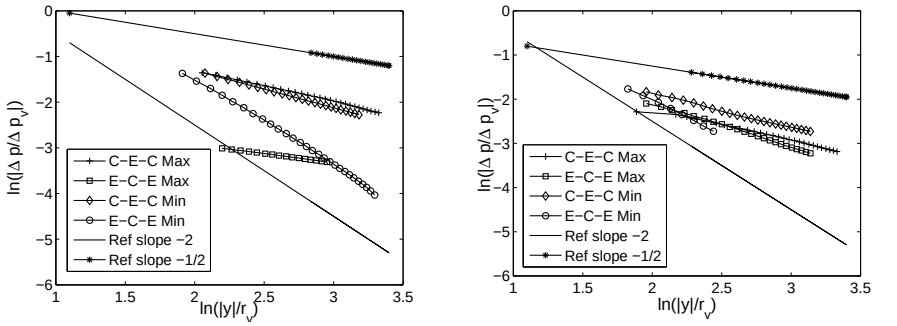

(c) $M_v = 0.4$ (d) $M_v = 0.8$

Figure 3.21: Power law decay of amplitudes of the pressure signal for $M_s = 1.7$ for a composite vortex with $r_o = 2r_v$ showing a more smooth decay

3.3.5 Case 5 : $M_s = 2.0$

Again the same two types of vortices are used with four different strengths of M_v = 0.1, 0.2,0.4 and 0.8. The upstream vortex interaction starts at t = 0.25 units. Noise because of the carbuncle instability appears at later time in some of the computed solutions.

The interactions considered here come under weak interaction and Mach reflection with no regular reflection of the shock observed. This again follows the classification of Grasso and Pirozolli [13]. Since they follow a similar trend as observed for $M_s = 2.0$ no contour plots are presented.

Qualitatively similar results are observed for both types of vortices and also for both the composite vortices considered.

For weak vortices the C-E-C wave undergoes still the formation of the N wave and within the computational domain considered they have not reached the asymptotic decay of $t^{\frac{-1}{2}}$.

The E-C-E waves decay closer to t^{-2} for weak vortices and show shift in decay towards $t^{\frac{-1}{2}}$ with increasing vortex strengths. They agree closely with the predictions of GSD.

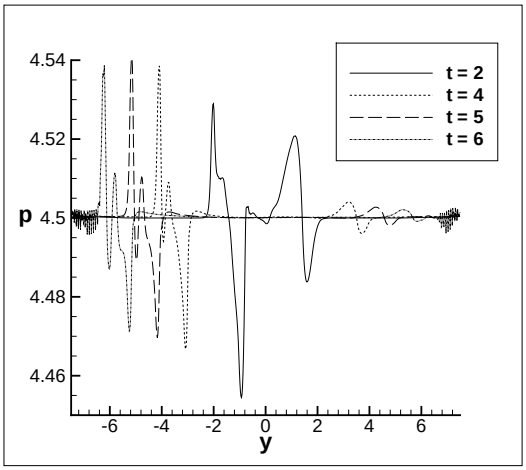

(a) snapshot of the pressure signal at various time intervals for $M_v = 0.1$

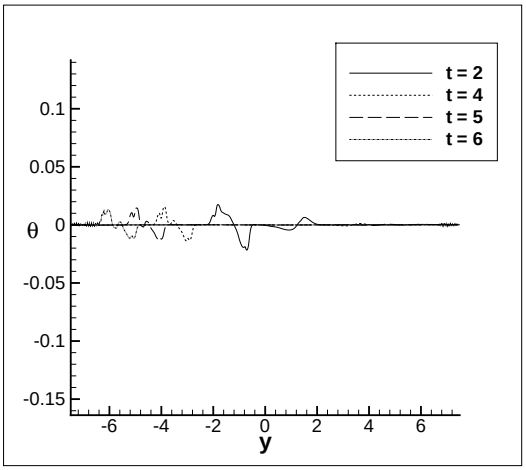

(b) snapshot of flow angle at various time intervals for $M_v = 0.1$

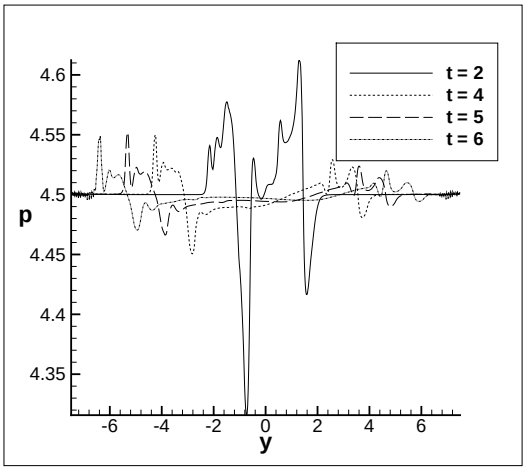

(c) snapshot of the pressure signal at various time intervals $M_v = 0.4$

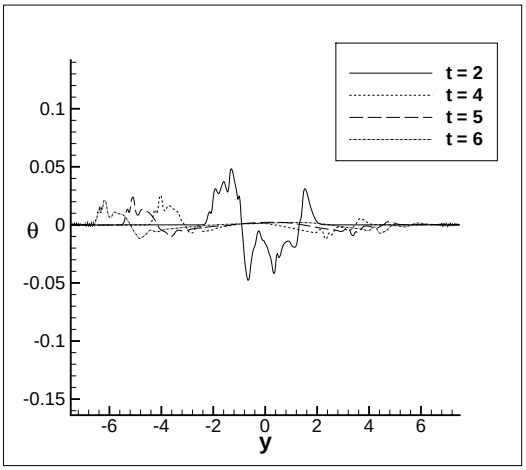

(d) snapshot of flow angle at various time intervals $M_v = 0.4$

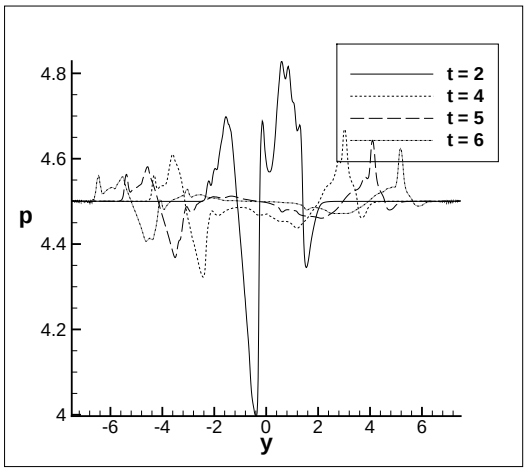

(e) snapshot of the pressure signal at various time intervals $M_v = 0.8$

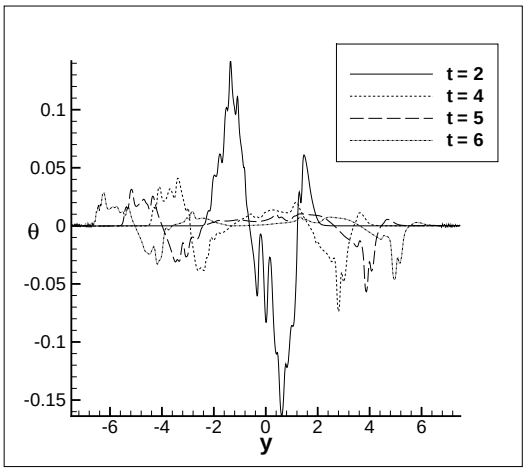

(f) snapshot of flow angle at various time intervals $M_v = 0.8$

Figure 3.22: Pressure disturbance and change in the flow angle measured along AB for shock strength $M_s = 2.0$

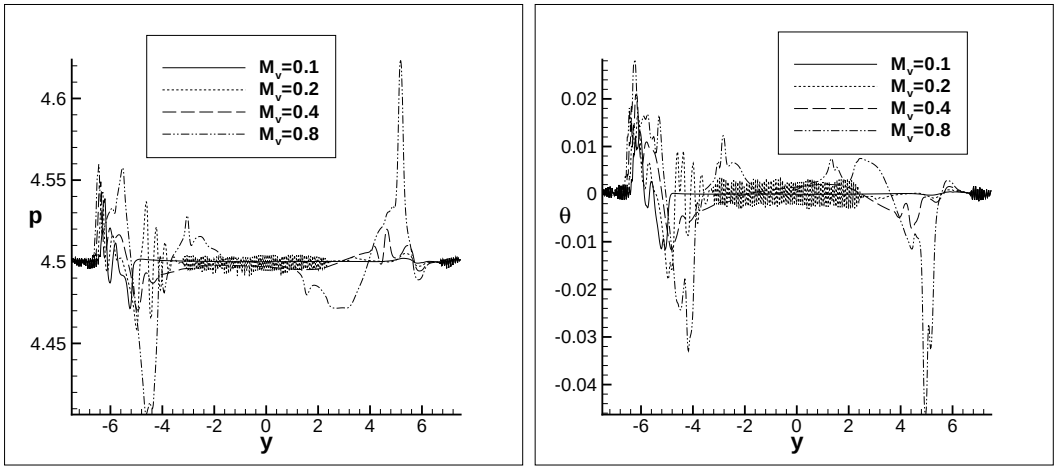

(a) snapshot of the pressure signal with varying vortex strengths

(b) snapshot of flow angle with varying vortex strengths

Figure 3.23: Pressure disturbance and change in flow angle measured along AB for shock strength $M_s = 2.0$ and vortex strengths $M_v = 0.1$, 0.2, 0.4 and 0.8 after t = 6 units. The noise present is because of the presence of carbuncle instability

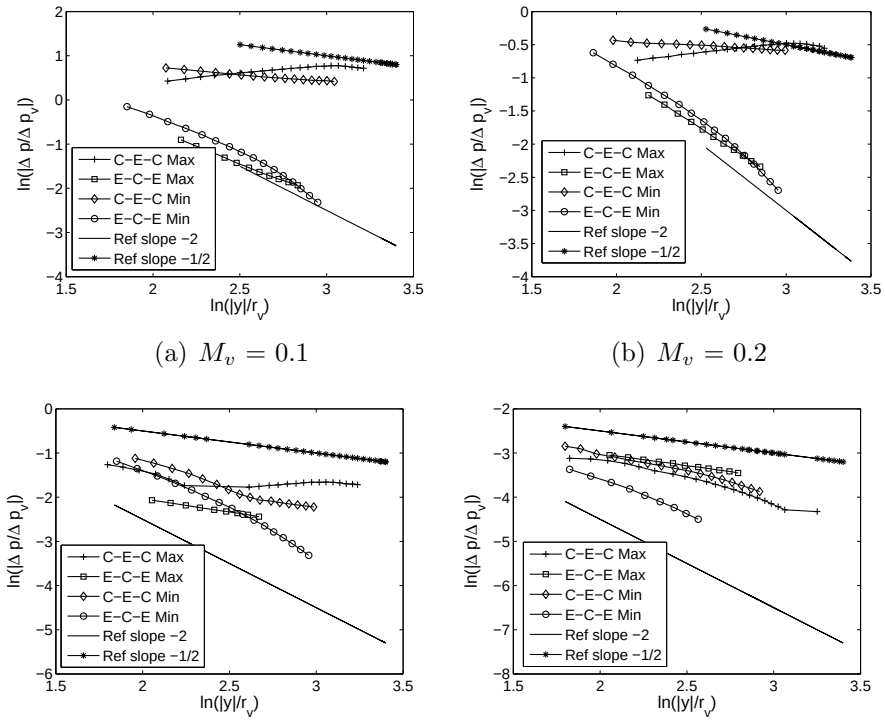

(a) $M_v = 0.1$

(b) $M_v = 0.2$

(c) $M_v = 0.4$

(d) $M_v = 0.8$

Figure 3.24: Power law decay of amplitudes of the pressure signal for $M_s = 2.0$ for an isentropic vortex.

3.4 Decay rates

We observe from the set of numerical shock-vortex experiments

- With the increasing shock Mach number the difference between the fastest and the slowest decay rates increases. The fastest decay approaches a power law decay slope of -2.0 for all vortex strengths and the slowest rate approaches -0.5 and it is apparently less for weak vortices - strong shock configuration
- For weaker shocks there is less difference between the fast and the slow decay rates and it is seen that for all the vortex strengths considered they decay closer to the the power law slope of -1.0. The decay slightly shift towards slower rates with increasing vortex strengths.
- For strong shocks and weak vortices there are cases that decay little if at all within the computational domain and we suppose they have not reached the asymptotic state and that they will decay eventually. This behavior was also observed in the predictions of GSD

3.5 Classification of the interactions

Grasso and Pirozolli classified shock vortex interaction on the basis of shock topology shortly after the encounter. Each type of interaction occurred in a certain region of the plane(refer figure 3.5). We found that a classification based on the decay rates of the waves yielded a different division of the plane. We classified the interactions as

- Fast decay
- Slow decay

though the distinction is not very clear, as it also depends on how symmetrically the waves are generated at the time of the interaction. The slow decay occurs for higher shock Mach numbers and becomes slowest with weaker vortices.

The amplitude of the C-E-C waves depends on the shock strength M_s and increases uniformly with increase in the vortex strength M_v whereas the amplitude of the E-C-E wave in particular seems to depend mainly on the vortex strength M_v. Our observations do not correlate well with the distinction as made in [13] for weak and strong interaction with the relevant parameter being $\frac{M_v}{M_s-1}$, whereas our parameter for the distinction between the fast and the slow rates of decay seems to be related by the parameter $M_s + \frac{M_v}{2}$.

3.6 Details from DNS on vortex strengths and validation of the computation

The motivation of our study on the shock and vortex interaction comes from the DNS studies revealing the interaction of the the discrete vortices along the foot of the shock. To quantify the strength of the vortices and the values which we have chosen in our study, we can do a simple non-dimensional study relating to the circulation of the separation bubble at the foot and relating it to the circulation around each vortices. The circulation around the bubble should be similar whether its boundary is continuous or formed with discrete vortices. A schematic setup is shown in the figure 3.25

Let Γ be the circulation around the entire bubble then

$$\begin{aligned} \Gamma &= U_e L = \Gamma_v N = 2\pi r_c M_v a_e N \\ \frac{M_v}{M_e} &= \frac{s}{2\pi r_c} \approx 0.5 \end{aligned} \tag{3.8}$$

with U_e being the speed of the free-stream, a_e being the speed of sound, L being the reference length say the length of the bubble with N the number of vortices, Γ_v the circulation around each vortex, r_c the radius of each vortex and s the distance between each vortex.

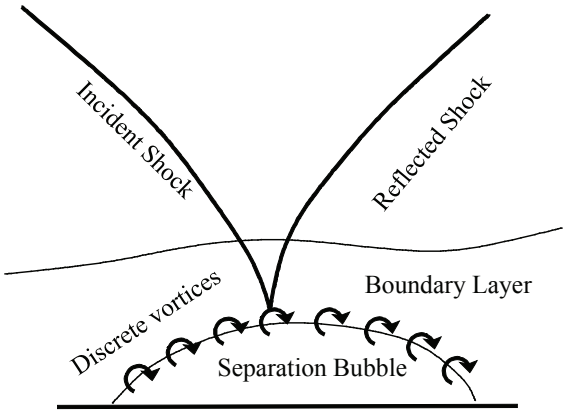

Figure 3.25: Schematic setup of discrete vortices in the boundary layer of SBLI

The RMS fluctuation of the results from DNS are shown in figure 3.26, courtesy Sergio Pirozolli for sharing their DNS data and the plot with us. In the region traversed by the vortices, the rms fluctuation in Mach number is about 0.35 and since the maximum fluctuation will be much more than the ones shown in the plot, our value of the vortex strengths seem to be in the range of interest.

Another validation of our experiments was done by Professor Farhad Jaberi from Michigan state university with his graduate student computing the wave propagation for the case of $M_s = 1.7$ and the vortex strength of $M_v = 0.4$. They considered a fine mesh of 1500x1500 cells and used a fifth order scheme for the same setup. The numerical Schlieren of their experiment is shown in the figure 3.27 with the measured pressure signal in figure 3.28, and the decay rates are shown in the figure 3.29.

Their results show the same nature of C-E-C as well as the E-C-E waves being generated and the decay of their maximum being closer to $t^{\frac{-1}{2}}$. The quantitative difference between our results and their is in the amplitude of the E-C-E wave which is higher for their case and this could be possibly because of the lesser numerical dissipation that they have in their code.

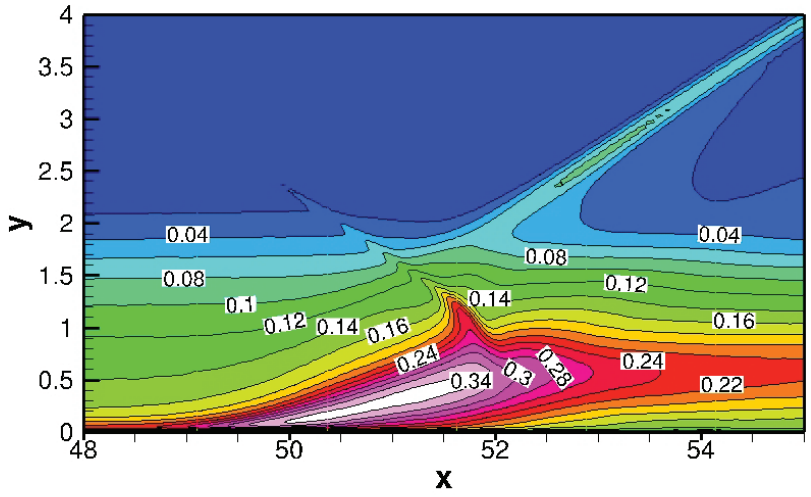

Figure 3.26: Contour of fluctuation in Mach number from DNS results of SWBLI along the foot of the shock. Courtesy Sergio Pirozolli

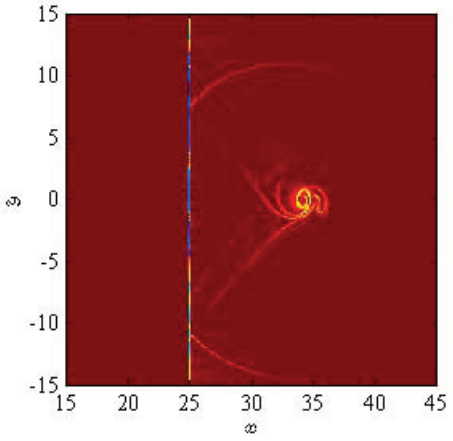

Figure 3.27: Numerical Schlieren of shock-vortex interaction with $M_s = 1.7$ and $M_v = 0.4$

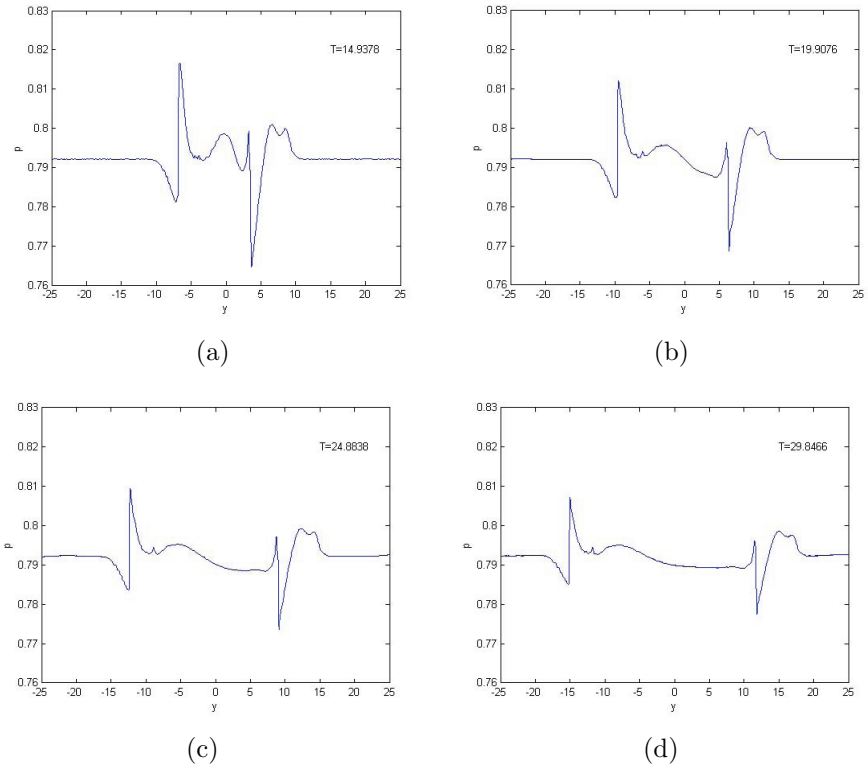

Figure 3.28: Wave structure in the pressure signal observed for shock-vortex interaction with $M_s = 1.7$ and $M_v = 0.4$ at different times

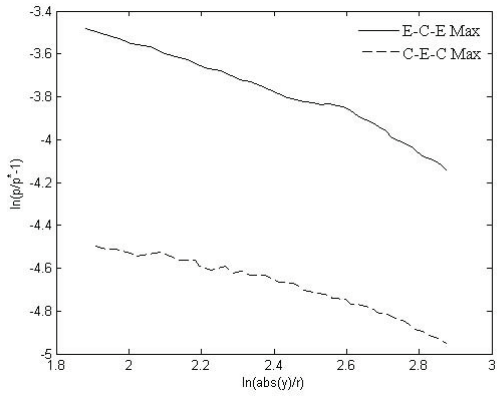

Figure 3.29: Power law decay for shock-vortex interaction with $M_s = 1.7$ and $M_v = 0.4$, p* represents the pressure downstream of the undisturbed shock

3.7 Inference from both Geometrical shock dynamcs(GSD) and Euler computations

The inferences we obtain from the study of shock vortex interaction using both Euler computation as well from the GSD model are listed as follows

- Whenever a shock wave is perturbed disturbances propagate away from the point of perturbation along the shock
- In 2-D flows this is qualitatively well represented by GSD even at large distances
- With the passage of a vortex through a normal shock, the asymmetry of the interaction leads to two different waves of different nature one being C-E-C wave and the other E-C-E waves that propagate along the shock
- Qualitatively similar wave structures is predicted by GSD with even a simple symmetric initial condition though there is no direct correspondence with the exact strength of the shock when it is perturbed by the vortex
- In terms of the disturbance in the shape of the shock, Euler computation provides results indicating that not much of visual distortion is seen at larger distances from the point of interaction of the vortex
- The wave decay as predicted by Euler computation varies between $t^{\frac{-1}{2}}$ and t^{-2}. For weak shocks the decay is t^{-1} for both the maximum and minimum of the waves indicating both the waves decay at the same rates
- The prediction by GSD in terms of the decay rate is closer to $t^{\frac{-1}{2}}$ for slowly decaying waves and t^{-2} for the fast waves indicating that GSD models well for shocks of higher strengths

Overall we conclude from the study of shock-vortex interaction both using Euler computation as well as GSD, the waves that travel along the shock do decay at large

distances and that those noises that travel along the shock would play a substantial role in studying the dynamics of shock trains. In real shock-trains there are disturbances from the side walls and thus it necessitates the development of the theory of GSD to study shock-surfaces. A three-dimensional, geometric version of GSD for shock surfaces and a numerical scheme to solve it is proposed in the next chapter.

CHAPTER IV

Shock surface propagation in 3D flows

In real shock trains at the inlets of Scramjet engines, turbulent boundary layers will be present along the side walls and will give perturbations along the shocks. The interaction is 3-D with the effect of disturbances from the side walls also. We shall here propose the extension of GSD to study the dynamics of shock surfaces. A formulation was given earlier by Whitham [38] and its numerical implementation done by Schwendeman [31] to study the stability of converging spherical and cylindrical shocks. Their equations were 3-D analogous to the supersonic potential flow. However that formulation followed the lines described for 2-D propagation into a moving freestream. This has the same unfortunate features discussed in section 2.6.1.

Here we retain the formulation of solving the governing equations in the 2-D ray-time coordinates treating it analogously to the Lagrangian approach for Godunov type methods for Euler equations[16].

4.1 Governing Equations of Geometrical shock dynamics(GSD) for Shock surfaces

We again return to the simple case of a shock moving into a stationary medium, and consider the set of surfaces $t = \text{const}$ that represent the shockwave in a sequence of locations, together with the set of lines orthogonal to these surfaces. We shall call

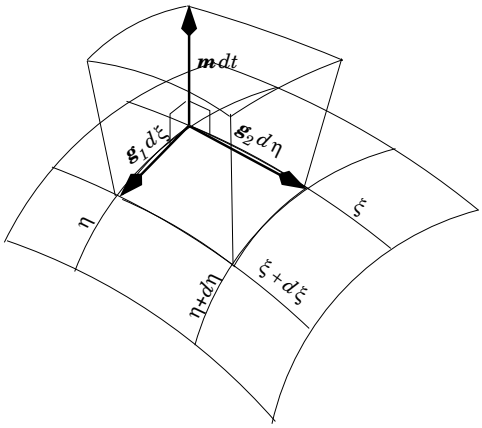

Figure 4.1: Part of the shock/ray net for a three-dimensional shock propagating into a stationary medium. If the medium is in uniform motion with velocity $\mathbf{u}_0 = a_0\mathbf{m}_0$, then the "box lid" will be displaced through a distance $\mathbf{m}_0\ d$t, and the rays will be sheared.

these as ray surfaces.

We introduce along the shock surface coordiates $\xi = \text{const}, \eta = \text{const}$, but not necessarily orthogonal to each other[1]. A computational unit comprises a small patch of shock surface, bounded by line elements $\mathbf{g}_1 d\xi, \mathbf{g}_2 d\eta$. We define $\mathbf{m}$ as a vector normal to the shock surface directed along a ray, where rays by definition are perpendicular to the shock surfaces. The magnitude of $\mathbf{m}$ is the normal Mach number. The "conservation law", which is purely geometrical here as in two dimensions, is merely that the small parallelepiped created by propagating the patch in time has a closed surface. The setup is shown in the figure 4.1

$$\partial_t(\mathbf{g}_1 \times \mathbf{g}_2) + \partial_\xi(\mathbf{g}_2 \times \mathbf{m}) + \partial_\eta(\mathbf{m} \times \mathbf{g}_1) = 0 \tag{4.1}$$

This is readily proved by noting that $\mathbf{m} = \partial_t\mathbf{x},\ \mathbf{g}_1 = \partial_\xi\mathbf{x},\ \mathbf{g}_2 = \partial_\eta\mathbf{x}$. The discrete version is that the six vectors representing normals to the six faces must sum to zero. This appears rather different from the corresponding two-dimensional equation (2.2), because it deals with the time-derivative of a vector $\mathbf{g}_1 \times \mathbf{g}_2$ that is normal to the

[1] As, of course, is not generally possible [35].

shock front, whereas (2.2) deals with the time derivative of a vector $\mathbf{g}$ that lies in the shock front. To see that they are compatible, cross (2.2) with $\mathbf{e}_z$, the unit vector perpendicular to the xy-plane.

If the normal to the shock surface is taken to be $\mathbf{n}$, then we have $\mathbf{g}_1 \times \mathbf{g}_2 = g\mathbf{n}$ where g has the dimensions of area, and also $\mathbf{m} = m\mathbf{n}$. Hence

$$\partial_t \left(\frac{g(m)}{m} \mathbf{m} \right) + \partial_\xi (\mathbf{g}_2 \times \mathbf{m}) + \partial_\eta (\mathbf{m} \times \mathbf{g}_1) = 0 \tag{4.2}$$

which simplifies to give the non-conservative evolution equations

$$\partial_t \left(\frac{g(m)}{m} \mathbf{m} \right) + \partial_\eta \mathbf{x} \times \partial_\xi \mathbf{m} - \partial_\xi \mathbf{x} \times \partial_\eta \mathbf{m} = 0 \tag{4.3}$$

These can be analyzed to find the domain of dependence by seeking plane waves $\mathbf{m} = \exp i(\omega t + k_1 \xi + k_2 \eta)$. After some algebra, the dispersion relationship turns out to be;

$$\frac{g^2 \omega^2}{m^2} = (k_1 \mathbf{g}_2 - k_2 \mathbf{g}_1) \cdot (k_1 \mathbf{g}_2 - k_2 \mathbf{g}_1)$$

The evolution of each line element follows from

$$\partial_t \mathbf{g}_\alpha = \mathbf{g}_\alpha \cdot \nabla \mathbf{m}, \qquad \alpha = 1, 2. \tag{4.4}$$

where ∇ represents the gradients in the physical space. From this pair of equations, one can derive an invariant quantity, thus

$$\partial_t (\mathbf{g}_1 \cdot \nabla \mathbf{g}_2 - \mathbf{g}_2 \cdot \nabla \mathbf{g}_1) = 0 \tag{4.5}$$

This merely states that the outline of the patch remains closed. However, we see below that it does have some numerical significance.

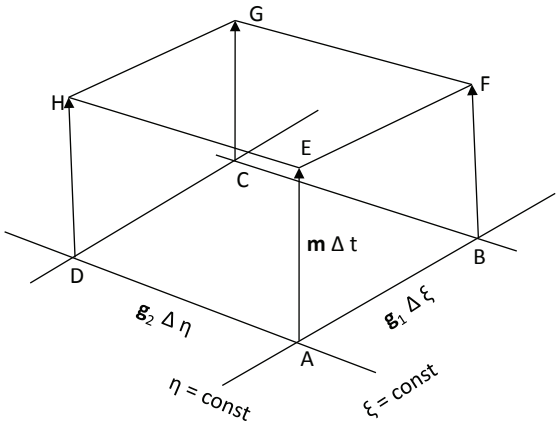

Figure 4.2: The propagation of a shock patch along rays

4.2 Numerical setup

A numerical scheme will advance from one shock surface to the next, and an obvious strategy would be to treat each computational unit as a finite volume, computing the "fluxes", $\mathbf{g}_\alpha \times \mathbf{m}$ on each of the four faces. However, that creates a slight awkwardness, because $\mathbf{g}_\alpha \times \mathbf{m}$ also represents the motion of the face by defining the vector normal to it in $\mathbf{x}$. Where four faces meet at one vertex, it is not possible for the path of the vertex to lie in all of them. This is the same difficulty that has bedevilled attempts to create Lagrangian versions of Godunov-type methods [16]. The cure is the same, to focus instead on the motion of the cell vertices (there the path lines, here the rays). The new patch is then formed simply by joining the new vertices and closure of the patch boundary is automatic. This result is the same as the one found found by Morton and Roe [20] for the acoustic wave system, where the vorticity is the invariant, and is preserved by a finite-volume scheme if and only if the fluxes are evaluated at vertices. The numerical setup and the scheme is given as follows.

Let the motion of the shock be represented by a series of surfaces, each coinciding with the shock location at a particular time t. Define a ray to be a line whose direction

is always normal to the shock surface, and hence define a ray tube as shown in the figure 4.2. Let ξ, η be an arbitrary pair of coordinates that propagate along the rays, so that we have the co-ordinate system (ξ, η, t) defined for all time along the shock surface. Here in the figure 4.2 the shock patch ABCD propagates to the closed patch EFGH along the rays.

The shock surface propagates normal to itself at speed m [2], the distance AE is for example $m\Delta t$. Defining $\mathbf{g}_1 = \partial_\xi \mathbf{x}$, then AB $= \mathbf{g}_1 \Delta\xi$ and $\mathbf{g}_2 = \partial_\eta \mathbf{x}$ and AD $= \mathbf{g}_2 \Delta\eta$. The fact that the ABFE is a closed quadrilateral (as seen from the geometrical nature of GSD for 2-D shocks) gives

$$\partial_t \mathbf{g}_1 = \partial_\xi \mathbf{m} \tag{4.6}$$

and similarly

$$\partial_t \mathbf{g}_2 = \partial_\eta \mathbf{m} \tag{4.7}$$

From the Area-Mach relation we have that

$$\frac{\partial \mathbf{m}}{\partial t} = \frac{d\mathbf{m}}{d\mathbf{A}} \frac{\partial \mathbf{A}}{\partial t} \tag{4.8}$$

where $\mathbf{A}$ represents the area vector of the shock patch or the ray tube with

$$\mathbf{A} = (\mathbf{g}_1 \times \mathbf{g}_2) d\xi d\eta = \mathbf{g} d\xi d\eta = g\mathbf{n} d\xi d\eta \tag{4.9}$$

[2] All the variables in bold represent vectors, say $\mathbf{m}$ is a vector and m its magnitude

$$
\begin{aligned}
\frac{\partial \mathbf{m}}{\partial t} &= \frac{d\mathbf{m}}{d\mathbf{A}}\frac{\partial \mathbf{A}}{\partial t} \\
&= \frac{d\mathbf{m}}{d\mathbf{g}}\frac{\partial(\mathbf{g}_1 \times \mathbf{g}_2)}{\partial t} \\
&= \frac{d\mathbf{m}}{d\mathbf{g}}(\partial_t \mathbf{g}_1 \times \mathbf{g}_2 + \mathbf{g}_1 \times \partial_t \mathbf{g}_2) \\
&= \frac{d\mathbf{m}}{d\mathbf{g}}(\mathbf{g}_1 \times \partial_t \mathbf{g}_2 - \mathbf{g}_2 \times \partial_t \mathbf{g}_1) \\
&= \frac{d\mathbf{m}}{d\mathbf{g}}(\mathbf{g}_1 \times \partial_\eta \mathbf{m} - \mathbf{g}_2 \times \partial_\xi \mathbf{m}) \qquad (4.10)
\end{aligned}
$$

with $\frac{d\mathbf{m}}{d\mathbf{g}}$ representing the Jacobian and writing it in terms of the components of $\mathbf{m}$ and $\mathbf{g}$ we have [3]

$$
\begin{pmatrix}
\partial_{g_1} m_1 & \partial_{g_2} m_1 & \partial_{g_3} m_1 \\
\partial_{g_1} m_2 & \partial_{g_2} m_2 & \partial_{g_3} m_2 \\
\partial_{g_1} m_3 & \partial_{g_2} m_3 & \partial_{g_3} m_3
\end{pmatrix}
$$

$$
m_i = m(\sqrt{g_1^2 + g_2^2 + g_3^2})\frac{g_i}{\sqrt{g_1^2 + g_2^2 + g_3^2}} = m(g)\frac{g_i}{g} \qquad (4.11)
$$

$$
\begin{aligned}
\frac{\partial m_i}{\partial g_i} &= \frac{\partial m}{\partial g}\frac{g_i^2}{g^2} + \frac{m}{g}(1 - \frac{g_i^2}{g^2}) \\
\frac{\partial m_i}{\partial g_j} &= \frac{g_i g_j}{g^2}(\frac{\partial m}{\partial g} - \frac{m}{g}), \quad i \neq j \qquad (4.12)
\end{aligned}
$$

Note the difference in the Jacobian's between the 2-D GSD case where $\mathbf{m}$ and $\mathbf{g}$ are orthogonal to each other whereas in 3-D case they are in the same direction. This is a consequence of the definition of the area vector of the shock segment in 2-D and 3-D space.

[3] These are the components of $\mathbf{m} = m\mathbf{n}$ and $\mathbf{g} = g\mathbf{n}$ with 3 components, this is not to be confused with $\mathbf{g}_1$ and $\mathbf{g}_2$ which are vectors representing the lines along the shock surface

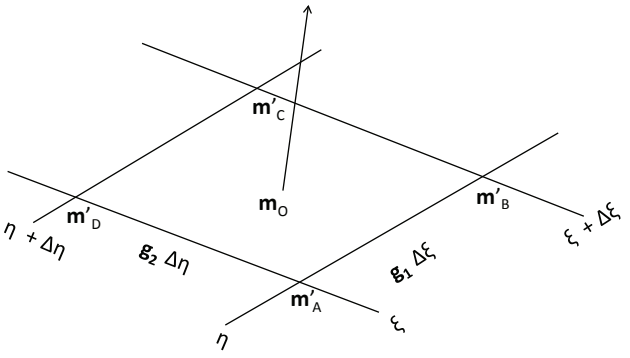

Figure 4.3: Numerical setup of a shock patch at an instant t

Scheme

There are some choice of storage locations for the variables $\mathbf{g}_1, \mathbf{g}_2$ and $\mathbf{m}$. The most natural one seems to be that of defining the average values of $\mathbf{g}_1, \mathbf{g}_2$ along the lines ξ and η respectively and defining $\mathbf{m}$ along the cell center as shown in the figure 4.3 As stated above we have $\mathbf{m}_o$ at the cell center and $\mathbf{g}_1, \mathbf{g}_2$ at one of the edges as shown.The predictor corrector scheme based on rotated Richtmyer method [28] can be used to get the updates. Averaging $\mathbf{m}$ to the vertices[4] from the cells adjacent to it

$$\mathbf{m}_0^{'} = \mu_\xi \mu_\eta \mathbf{m}_0 \tag{4.13}$$

where μ is an averaging operator and δ is the difference operator(will be used later). Thus at time t the cell centered average of $\mathbf{m}$ values are distributed along the vertices A,B,C and D as shown.

[4] $\mathbf{m}$ denotes the value at the cell center and $\mathbf{m}$' represents the value at the vertices unless otherwise stated

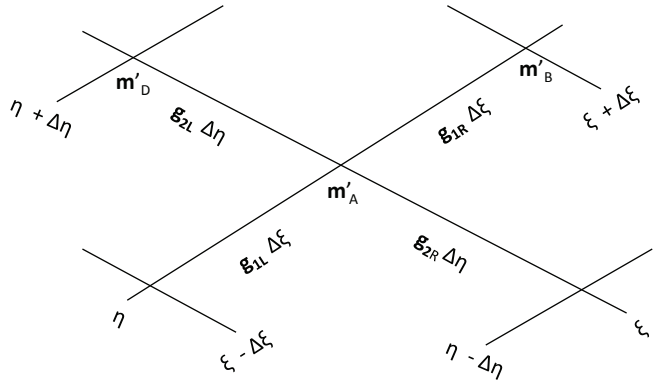

Figure 4.4: Nodal setup

Predictor-step

In the predictor step the edges are updated using the relation

$$\mathbf{g}_1^{1/2} = \mathbf{g}_1 + \frac{\Delta t}{2}\delta_\xi \mathbf{m}'_0 = \mathbf{g}_1 + \frac{\Delta t}{2}(\mathbf{m}'_B - \mathbf{m}'_A) \tag{4.14}$$

$$\mathbf{g}_2^{1/2} = \mathbf{g}_2 + \frac{\Delta t}{2}\delta_\eta \mathbf{m}'_0 = \mathbf{g}_2 + \frac{\Delta t}{2}(\mathbf{m}'_D - \mathbf{m}'_A) \tag{4.15}$$

and the edges by the relation(the set up is shown in figure 4.4)

$$\mathbf{m}'_A{}^{1/2} = \mathbf{m}'_A + \overline{\frac{d\mathbf{m}}{d\mathbf{g}}}\frac{\Delta t}{2}(\mu_\xi \mathbf{g}_1 \times \mu_\xi \delta_\eta \mathbf{m} - \mu_\eta \mathbf{g}_2 \times \mu_\eta \delta_\xi \mathbf{m}) \tag{4.16}$$

where the average of $\mathbf{g}_1$ and $\mathbf{g}_2$ comes from the left and right values as indicated in the figure 4.4). The indication of as L and R to the values of $\mathbf{g}_1$ and $\mathbf{g}_2$ is to represent the adjacent locations with respect the nodal $\mathbf{m}$. The difference operators is operated on the cell center values of $\mathbf{m}$ and then averaged to get the derivative of $\mathbf{m}$ along the node. The average of the Jacobian follows a similar rule to that of the 2-D numerical setup 2.10. The value of $\mathbf{m}$ and $\mathbf{A}$ for the adjacent four cells are averaged to the

vertex and the Jacobian is obtained for that average value.

Corrector-step

Using the predicted data to update for full Δt we can first update the line segments

$$\mathbf{g}_1^1 = \mathbf{g}_1 + \Delta t \frac{(\mathbf{m}'_B - \mathbf{m}'_A)}{\Delta \xi} \tag{4.17}$$

$$\mathbf{g}_2^1 = \mathbf{g}_2 + \Delta t \frac{(\mathbf{m}'_D - \mathbf{m}'_A)}{\Delta \eta} \tag{4.18}$$

The value of $\mathbf{m}$ along the cell can be obtained either using the relation 4.16 along the cell averaged values or either from the Area-Mach relation.

Since we know the propagation speed and direction of Mach number along the nodes from the predictor step we could propagate the solution in the physical space and thus obtain the physical area of the new cell or the shock patch at the next time step. This new area of the shock patch could also be obtained using 4.17 and 4.18. In a simpler sense the step on the updates of $\mathbf{g}_1$ and $\mathbf{g}_2$ could be done once the position of the new shock at the next time interval is known. That is, all we require is the update based on the equation 4.16.

In order to calculate propagation into a moving medium, similar to the 2-D setup it is only necessary to add the solution in the physical space to the velocity of the free-stream say $(m_0, 0, 0)$.

4.3 3D Test Cases

4.3.1 A Riemann problem

To verify the numerical scheme we consider a 1-D case. Consider the case of a moving planar shock which has a uniform distribution of Mach strong along one ray coordinate and a jump along the other ray coordinate. The boundary conditions are

taken to be non-reflecting(zero-gradient)conditions so that the waves that leave the boundary are not reflected back. This problem setup is not more physical but taken for mathematical convenience to see how well the numerical scheme does in capturing the shock-shock and the expansion along the shock. The shock surface is of 10×10 units in the $y-z$ plane, propagating along the positive $x-axis$ with a Mach strength of 1.5 along the bottom half and then with the Mach strength of 1.35 along the top half of the shock. This is more of a 2-D problem with jump in Mach number along a normal shock. A structured mesh along the $\xi - \eta$ plane is considered with 100×100 cells.

The solution in the $\xi - \eta$ plane for the distribution of shock strength m is given in figure 4.5 and 4.6. As can be seen with the initial data there are development of two different waves with the expansion wave going to the left and a shock-shock going towards the right. The proposed numerical scheme is second order accurate scheme and produces oscillations while predicting the shock-shock structure as cane be seen in figure 4.6.

The shock surface in the physical space is shown in figure with the contour of Mach number distribution along in the figure 4.7.

4.3.2 Modeling of shock - vortex ring interaction

The previous case was helpful in studying the numerical scheme from a simple Riemann problem pertaining to the equations of GSD. Now to understand the 3-D effects along the shock surface an IVP is modeled. Similar to the case of having a shock interacting with a vortex in 2-D flows here we model the shock getting perturbed by its interaction with a vortex ring. Numerical studies of this setup is found in the works of Takayama *etal.* [11] and experimental results for the interaction of a spherical shock with a vortex ring has been done by Minota [18].

Consider a plane stationary shock which interacts with a vortex ring that passes

through the shock. Analogous to the case of shock-vortex interaction being modeled as IVP in Mach distribution for 2-D flows here the shock-vortex ring interaction is modeled as an IVP in Mach distribution along the shock surface with a periodic perturbation in the radial direction.

Consider a standing shock surface of 10×10 units in the $y - z$ plane with Mach strength of 1.5. A sinusoidal perturbation along radial direction in Mach strength of 0.1 amplitude is given along a ring with inner radius of 1 units and outer radius of 2 units. A structured mesh along the $\xi - \eta$ plane is considered with 100×100 cells.

The contour of the Mach strength along the shock surface is plotted in figure 4.8. We observe two waves one moving radially inward and the other moving outward. When the inner moving wave collapses it gives rise to new maxima and minima of the shock strength. For the above case considered the maximum shock strength obtained is 2.04 and 1.31. Since we have a scheme which predicts oscillations it is still not clear whether the waves that are found in-between the outward going wave and the inward going waves are due to numerical oscillations and also the peaks being obtained along the center are because of the interaction of those oscillations.

Note on the Numerical scheme

The numerical scheme is of second order accurate with half time stepping and gives oscillations while trying to compute shock-shocks. The only equation that we would like to solve is to advance the shock-patch given by the equation 4.16 and once we know the shock-position other parameters can be computed. Compare this with the 2-D GSD equation 2.10 for the update of the flux. The difference is that the solution at the predictor step is reconstructed and then limited to avoid oscillations near the discontinuities. A similar procedure needs to be followed to restrict the oscillations especially near the shock-shocks, but in 2-D GSD we have the non-conservation form of the equations which could be implemented using a Hancock scheme with the

variables to be reconstructed being the ray angle and the Mach number of the shock. The numerical method implemented for 3-D GSD needs to be augmented with some limiter mechanism and this is left as a future work.

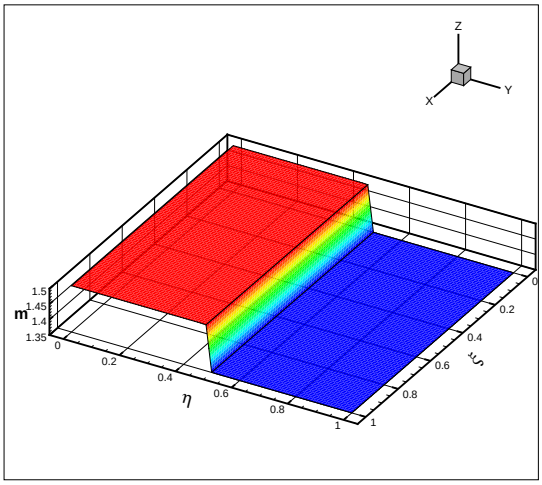

(a) Initial m distribution along the shock surface having a jump in the strength along one ray coordinate

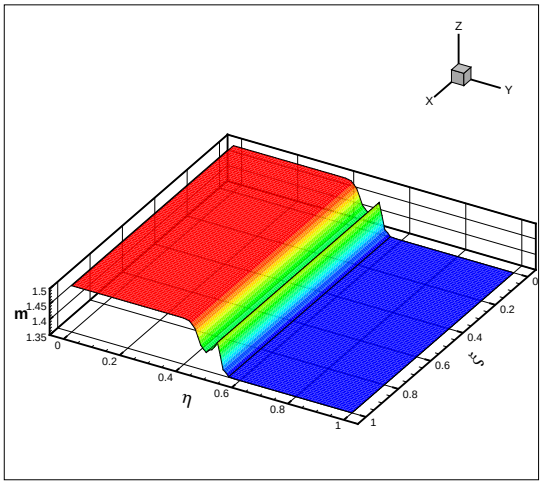

(b) m distribution along the shock surface after t = 0.625 units

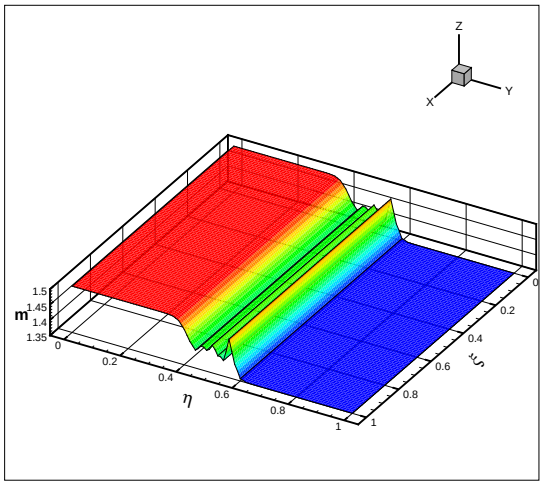

(c) m distribution along the shock surface after t = 1.25 units

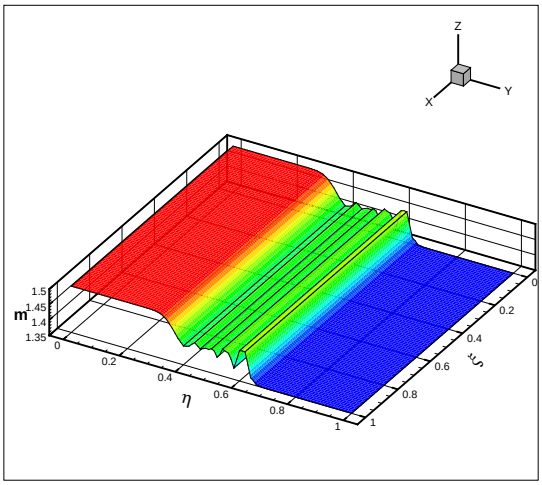

(d) m distribution along the shock surface after t = 1.875 units

Figure 4.5: GSD results: Riemann problem with left running expansion wave along the shock surface and a right running shock-shock

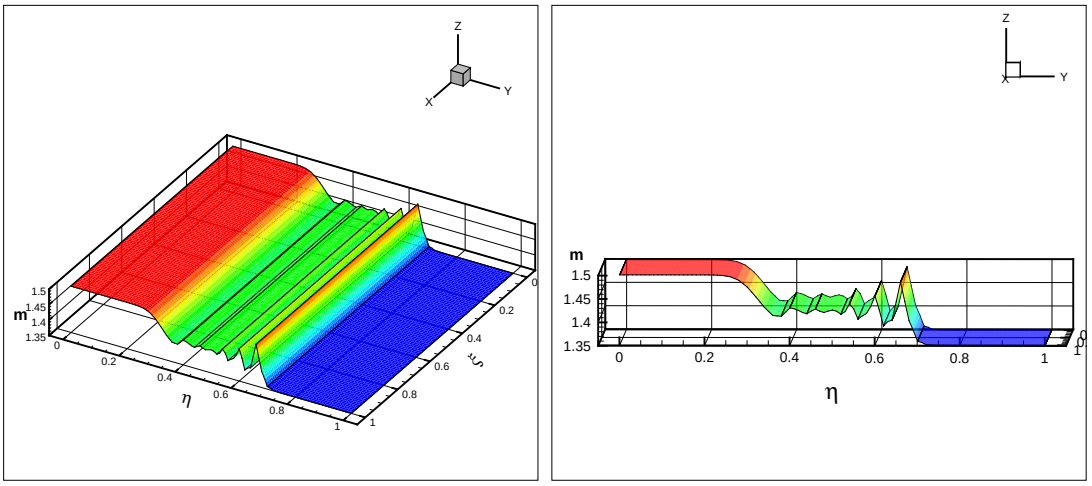

(a) m distribution along the shock surface after t = 2.5 units

(b) m distribution along the shock surface after t = 2.5 units in a different view

Figure 4.6: Riemann problem with left running expansion wave along the shock surface and a right running shock-shock showing well resolved expansion but oscillations along shock-shock

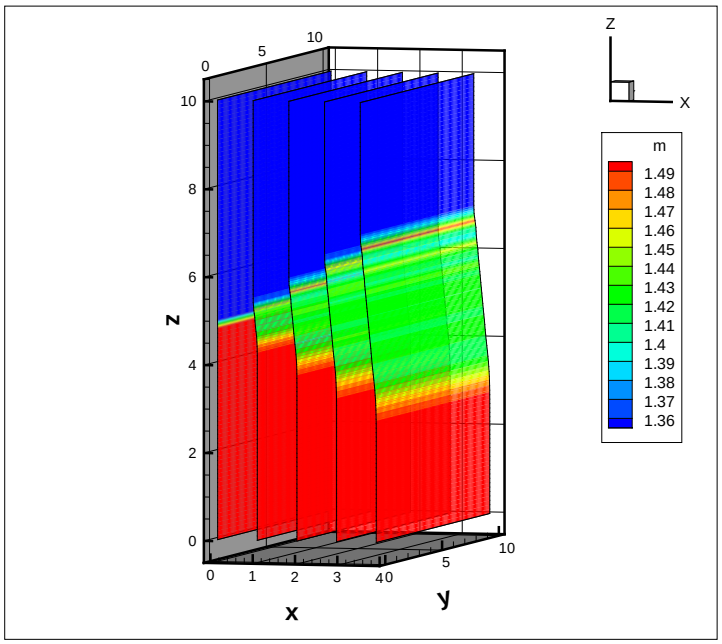

Figure 4.7: Shock surface propagating along the positive x axis. Shock surface at t = 0, 0.625,1.25,1.875 and 2.5 units

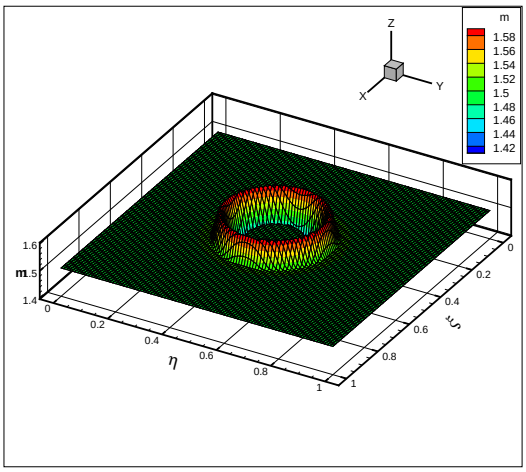

(a) Initial m distribution along the shock surface having a jump in the strength along one ray coordinate

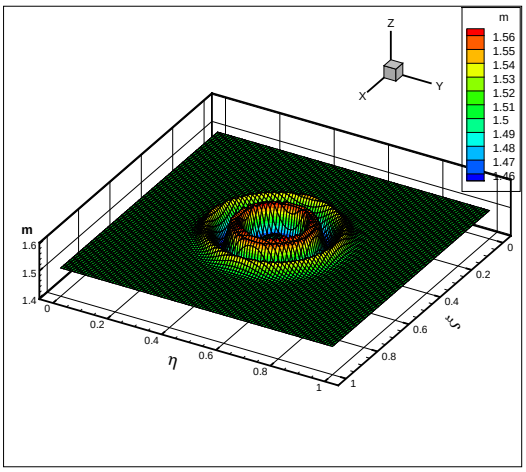

(b) m distribution along the shock surface after t = 0.625 units

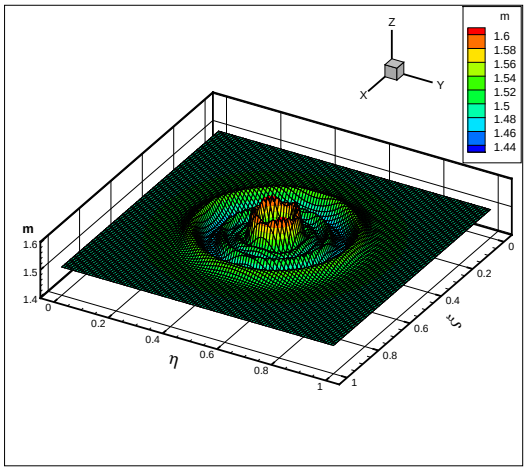

(c) m distribution along the shock surface after t = 1.25 units

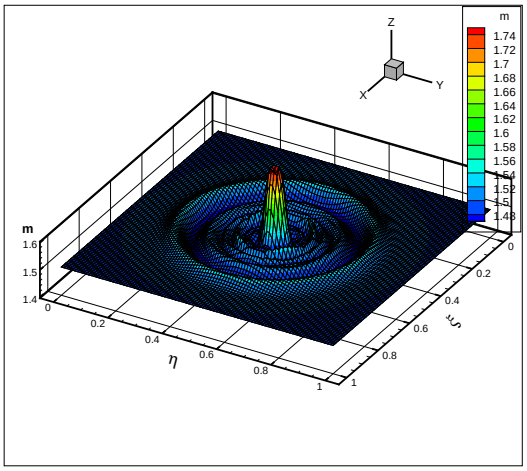

(d) m distribution along the shock surface after t = 1.875 units

Figure 4.8: GSD results: Solution to vortex-ring interaction using GSD showing waves going radial direction

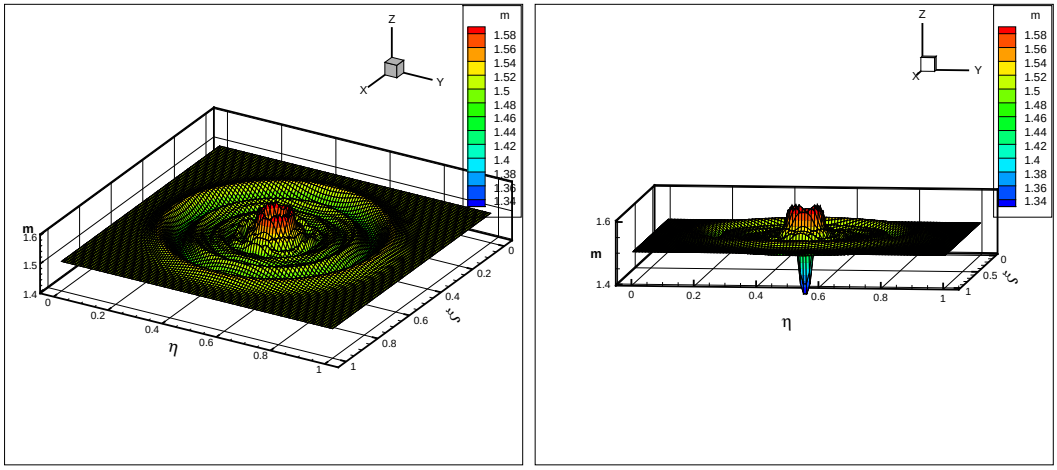

(a) m distribution along the shock surface after t = 2.5 units

(b) m distribution along the shock surface after t = 2.5 units in a different view showing the minimum

Figure 4.9: Vortex-ring solution showing waves in the radial direction at a later time showing the maximum and the minimum

CHAPTER V

Conclusions and Future work

Based on our studies and the results we summarize the observations. When shocks are perturbed they send out disturbances that propagate along them. In 2-D flows this is well predicted by the theory of GSD even at large distances. The theory of shock dynamics with a good numerical implementation, displays intricate detail in the long-time behavior of shock-waves.

In 2-D flows when a shock is perturbed by a vortex, the asymmetry of the interaction leads to waves of different character being sent in each direction. The wave structures are identified and classified as C-E-C and E-C-E type. They are present in Euler computations and are also predicted by GSD. The long range behavior of each wave type is similar to solutions of Burger's equation and their wave decay. Typically C-E-C wave type undergoes a decay of $t^{-\frac{1}{2}}$ once it reaches the asymptotic limit. The behavior of E-C-E wave is complicated when the wave type is not symmetrical.

Shock with lower strengths predict the decay of t^{-1} for both the wave types from Euler computations. The predictions of GSD are qualitatively correct when the shock is strong. In Euler computation of such cases we always observe at least one family of waves that decay at $t^{-\frac{1}{2}}$. This indicates that noise propagation may play an important role in studying shock trains. The interaction of waves of opposite family occurs when oblique shock interacts with multiple vortices at the same point of interaction.

However, our observation for a shock interacting with two vortices reveals that a C-E-C wave and an E-C-E wave, they pass through each other essentially unchanged.

These results about the wave decay reveal that in the SBLI problem, the disturbances along the shock may travel larger distances. The side walls along the inlet of scramjet engines may give additional disturbances and could explain some of the occurring instabilities. An extension of GSD to predict shock propagation in 3-D flows is implemented with scheme predicting numerical oscillations. A 3-D limiter for the proposed scheme and its implementation to study shock trains at engine inlets is left for future work.

APPENDICES

APPENDIX A

Area Mach Model 1

Whitham's Model

Consider a shock propagating down a tube of slowly varying cross section $A(x)$ varying as a function of x. The flow for $x < 0$ is uniform with constant cross sectional area A_0 and for $x > 0$ the cross sectional area is varying slowly with the condition $\frac{|A(x)-A_0|}{A_0} << 1$. The average quasi one dimensional equations of the inviscid compressible flow are

$$\partial_t \rho + u\partial_x \rho + \rho \partial_x u + \rho u \frac{A'(x)}{A(x)} = 0 \tag{A.1}$$

$$\partial_t u + u\partial_x u + \frac{\partial_x p}{\rho} = 0 \tag{A.2}$$

$$\partial_t p + u\partial_x p - a^2(\partial_t \rho + u\partial_x \rho) = 0 \tag{A.3}$$

with ρ, p, u, a denoting the density, pressure, particle velocity and local sound speed. Sound speed is defined by $a^2 = (\frac{\partial p}{\partial \rho})_S = \frac{\gamma p}{\rho}$ with S being the entropy of the particle. The assumption is that the shock propagates into a uniform medium at rest, characterized by a density ρ_0, pressure p_0 and sound speed a_0.

Let U define the speed of the shock and M define the Mach number of the shock so that $M = \frac{U}{a_0}$. From the classic Rankine Hugoniot relations across the shock we can write

$$u = \frac{2a_0}{\gamma+1}(M - \frac{1}{M}) \tag{A.4}$$

$$p = \frac{\rho_0 a_0^2}{\gamma(\gamma+1)}(2\gamma M^2 - (\gamma-1)) \tag{A.5}$$

$$\rho = \frac{\rho_0(\gamma+1)M^2}{(\gamma-1)M^2+2} \tag{A.6}$$

The sound speed can be given as

$$a = \frac{a_0\mu(2\gamma M^2 - (\gamma-1))}{(\gamma+1)M} \tag{A.7}$$

$$\mu^2 = \frac{(\gamma-1)M^2+2}{2\gamma M^2 - (\gamma-1)} \tag{A.8}$$

In the problem set up we have at large distance behind $x = 0$ the downstream state characterized by sound speed, density and particle velocity defined by a_1, p_1 and u_1 respectively. In order to obtain the solution of the quasi 1-D Euler equation for the region $x > 0$ we can linearize the equations A.1 about the initial uniform state in $x < 0$ as the tube is slowly varying. The linearized equations are given as

$$\partial_t\rho + u_1\partial_x\rho + \rho_1\partial_x u + \rho_1 u_1\frac{A'(x)}{A(x)} = 0 \tag{A.9}$$

$$\partial_t u + u_1\partial_x u + \frac{\partial_x p}{\rho_1} = 0 \tag{A.10}$$

$$\partial_t p + u_1\partial_x p - a_1^2(\partial_t\rho + u_1\partial_x\rho) = 0 \tag{A.11}$$

where ρ, p, u and $A'(x)$ represent $\rho - \rho_1, p - p_1, u - u_1$ and $(A(x) - A_0)'$. So from the problem set up we know that along the $u_1 + a_1$ characteristics the invariants do not

change. Writing the characteristic form of the equation

$$(\partial_t + (u_1 + a_1)\partial_x)(p + \rho_1 a_1 u) + \rho_1 a_1^2 u_1 \frac{A'(x)}{A_0} = 0 \tag{A.12}$$

along $\frac{dx}{dt} = u_1 + a_1$ which can be integrated to give

$$(p - p_1) + \rho_1 a_1 (u - u_1) = \frac{-\rho_1 a_1^2 u_1}{u_1 + a1} \frac{A(x) - A_0}{A_0} \tag{A.13}$$

Denoting M_0 as the strength of the shock when its moving in the uniform part of the tube for $x < 0$ and M being the strength when it has moved some distance along the tube of varying cross section then we can write

$$p - p_1 = \frac{dp}{dM}|_{M_0}(M - M_0) \tag{A.14}$$

$$u - u_1 = \frac{du}{dM}|_{M_0}(M - M_0) \tag{A.15}$$

Now $\rho_1, p_1, u1, a_1$ can be written as a function of M_0 from the Rankine Hugoniot jump relations across the shock for the uniform conditions behind the shock which after simplification gives the relation

$$\frac{A(x) - A_0}{A_0} = -g(M_0)(M - M_0) \tag{A.16}$$

with

$$g(M) = \frac{M}{M^2 - 1}(1 + \frac{2}{\gamma + 1}\frac{1 - \mu^2}{\mu})(1 + 2\mu + \frac{1}{M^2}) \tag{A.17}$$

The above equation for the Area change is written in the discrete sense, but assuming the change to be continuous give the relation

$$\frac{1}{A}\frac{dA}{dM} = -g(M) \tag{A.18}$$

which can be integrated to get the Area-Mach relation, which is

$$Af(z) = constant$$

where

$$f(z) = z^{\frac{1}{\gamma}}(z-1)(z+\frac{\gamma-1}{\gamma+1})^{-\frac{1}{2}}[\frac{1+R}{1-R}]^{\sqrt{\frac{\gamma}{2(\gamma-1)}}}(\frac{R-(\frac{\gamma-1}{2\gamma})^{\frac{1}{2}}}{R+(\frac{\gamma-1}{2\gamma})^{\frac{1}{2}}})$$
$$\times \exp[(\frac{2}{\gamma-1})^{\frac{1}{2}}\tan^{-1}\frac{2\gamma^{\frac{1}{2}}R}{\gamma-1}]$$

$$R = [1+\frac{\gamma+1}{(\gamma-1)z}]^{\frac{-1}{2}}; \quad z = \frac{2\gamma}{\gamma+1}m^2 - \frac{\gamma-1}{\gamma+1} \tag{A.19}$$

APPENDIX B

Area Mach Model 2

Closure Equations from Prasad for Curved Weak shocks

The system of equations given by Prasad et.al [19] to close the Area Mach relations is based on considering the information of the gradients behind the shock. The detailed derivation is available in [19]. Again reiterating the geometric conservation law

$$(Gsin\theta)_t + (Mcos\theta)_\xi = 0 \tag{B.1}$$

$$(Gcos\theta)_t - (Msin\theta)_\xi = 0 \tag{B.2}$$

where θ representing the ray angle with respect to a fixed reference axis, M being the strength of the shock and G being the metric along the shock. The closure between G and M comes by considering the gradient N behind the shock so that N is a measure of the rate of steepening of the non linear waves behind the shock.

$$(G(M-1)^2)_t + 2G(M-1)^2N = 0 \tag{B.3}$$

$$(G(M-1)^4N^{-2})_t = 0 \tag{B.4}$$

This set of equations has not been used in our simulations of GSD.

Closure relation used in this work

For weak non linear wavefronts the governing equations was derived in a polytropic gas by writing the wave propagation equation along the ray coordinates and assuming weak shock assumption which provides the governing equations and closure between G and M. The governing equations are still the same B.2 as indicated above but now the closure between G and M is given by

$$G(M) = \frac{f(\xi)}{(M-1)^{-2}\exp^{2(M-1)}} \tag{B.5}$$

where $f(\xi)$ is determined from the distribution of the intensity of M on the initial wavefront. The detailed derivation is given in Chapter 6 of Prasad [24]. Since this formulation doesn't involve the gradient N behind the shock, we have used equation B.5 for simplicity in our computations.

APPENDIX C

Behavior of E-C-E wave

Dynamics of E-C-E wave

Consider an initial data to the Burger's equation for a scalar u as shown in the figure C.1. Defining the initial data

$$u_L = M(1 + \frac{x}{d_L}), \quad u_R = -N(1 - \frac{x}{d_R}) \tag{C.1}$$

and $u(x,t) = 0$ outside of $x\epsilon[-d_L, d_R]$ If each part of the solution evolves independently then we can write the solution in the smooth region

$$u_L(x,t) = \frac{M(d_L + x)}{d_L + Mt}, \quad u_R(x,t) = \frac{-N(d_R - x)}{d_R + Nt} \tag{C.2}$$

A shock will form along the path defined by

$$\frac{dx_S}{dt} = \frac{u_L + u_R}{2} \tag{C.3}$$

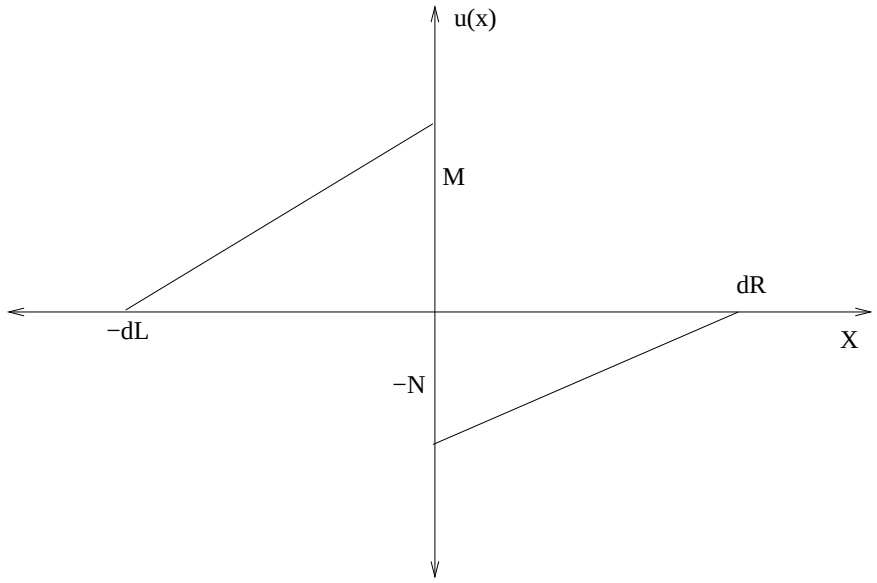

Figure C.1: Initial data for a generic E-C-E wave

which can be integrated with the initial condition, $x(0) = 0$ to give

$$x_S(t) = \frac{\sqrt{(d_L + Mt)(d_R + Nt)}(N + M)\sqrt{d_L d_R} - (N + M)d_L d_R - MN(d_L + d_R)t}{Md_R - Nd_L} \tag{C.4}$$

Let us call the maximum and the minimum of the wave amplitudes $u_M(t)$ and $u_N(t)$ respectively, then by inserting the value of x_S in C.2 we get

$$u_M(t) = \frac{M}{Md_R - Nd_L}[(M + N)\sqrt{d_L d_R \frac{d_R + Nt}{d_L + Mt}} - N(d_L + d_R)] \tag{C.5}$$

$$u_N(t) = -\frac{N}{Md_R - Nd_L}[(M + N)\sqrt{d_L d_R \frac{d_L + Mt}{d_R + Nt}} - M(d_L + d_R)] \tag{C.6}$$

The total jump is given by $u_M(t) + u_N(t)$ in a much simpler form

$$u_M(t) + u_N(t) = \frac{(M + N)\sqrt{d_L d_R}}{\sqrt{(d_L + Mt)(d_R + Nt)}} \tag{C.7}$$

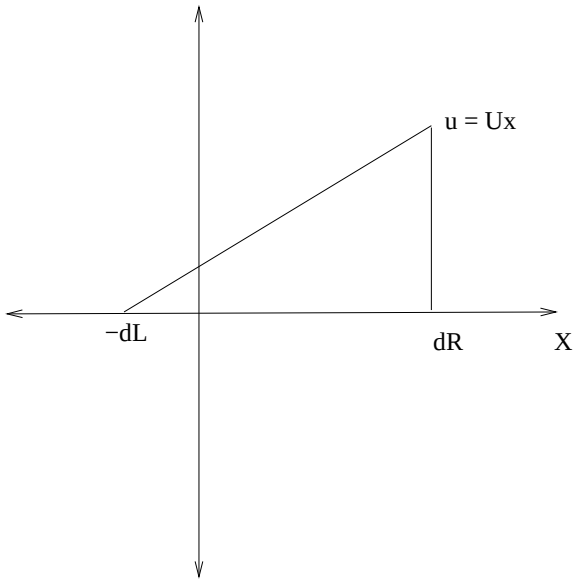

Figure C.2: IVP after the shock eats the right running expansion

These values decay at the rate t^{-1}. All of this is under the assumption that the shock is sandwiched between both the expansion waves so that the shock does not leave the interval $(-d_L, d_R)$. Suppose that if the shock reaches the right boundary i.e $x_S = d_R$ then we have two roots for t with

$$t_B = \begin{cases} -\frac{d_R}{N} & < 0 \\ \frac{d_R}{M}\frac{Md_R+2Md_L+Nd_L}{Md_L-Nd_R} & \end{cases}$$

The first root is non physical and for the second root the numerator is positive, so that $t_B > 0$ if the expression $Md_L - Nd_R > 0$. This quantity is the initial integral of the solution and hence the integral for all time. The result is that if $I_O = Md_L - Nd_R > 0$ then the shock eventually reaches(crosses) the right boundary otherwise the shock eventually would reaches(crosses) the left boundary. This is not the same as the condition as $M > N$ that the shock initially moves towards the right.

Consider when the shock reaches the right boundary then we have new IVP with the data as shown in figure C.2 where $Ux = \frac{I_O}{d_L+d_R}$ by conservation and thus

$$u(x,t) = \frac{(x+d_L)I_O}{(d_L+d_R)^2 + I_O t} \tag{C.8}$$

leading to the subsequent behavior of the shock is described by

$$\begin{aligned} x_S(t) &= d_R + (d_R+d_L)\sqrt{(d_L+d_R)^2 - I_O(t-t_B)} \\ u_S(t) &= \frac{I_O}{\sqrt{(d_L+d_R)^2 - I_O(t-t_B)}} \end{aligned} \tag{C.9}$$

So the shock will reach one boundary at a finite time(unless $I_O = 0$) and from then onward one peak amplitude of u (either the maximum or the minimum) is zero, and the other decays like $t^{-\frac{1}{2}}$. We can distinguish two "asymptotic" phases. As we have seen that the remaining peak decays like $t^{-\frac{1}{2}}$, just before the shock reaches $x = d_R$, say we have $u_M(t) >> u_N(t)$ so that

$$u_M(t) \approx u_M(t) + u_N(t) = \frac{(M+N)\sqrt{d_L d_R}}{\sqrt{(d_L+Mt)(d_R+Nt)}} \tag{C.10}$$

and the decay during this stage is like t^{-1}. We can also expand for small t,

$$\begin{aligned} \frac{u_M(t)}{M} &= 1 - \frac{1}{2}\frac{(M+N)t}{d_L} \\ \frac{u_N(t)}{N} &= 1 - \frac{1}{2}\frac{(M+N)t}{d_R} \end{aligned} \tag{C.11}$$

So initially both the peaks decay at a similar rate.

BIBLIOGRAPHY

BIBLIOGRAPHY

[1] E. A. Pimonov A. A. Zheltovodov and D. Knight Doyle. Numerical modeling of vortex/shock wave interaction and its transformation by localized energy deposition. *Shock Waves*, 17:273–290, 2007.

[2] P. D. Lax A. Harten and B. van Leer. On Upstream Differencing and Godunov-Type Schemes for Hyperbolic Conservation Laws. *SIAM Review*, 25:35–61, 1983.

[3] N.T. Clemens B. Ganapathisubramani and D.S. Dolling. Effects of upstream boundary layer on the unsteadiness of shock-induced separation. *Journal of Fluid Mechanics*, 585:369–394, 2007.

[4] S. Baskar and P. Prasad. Riemann problem for kinematical conservation laws and geometrical features of nonlinear wavefronts. *IMA Journal of Applied Mathematics*, 69:391–419, 2004.

[5] J. P. Best. A generalisation of the theory of shock dynamics. *Shock Waves*, 1:251, 1991.

[6] J. P. Best. Accounting for transverse flow in the theory of geometrical shock dynamics. *Proc. Roy. Soc. Lond. Ser. A*, 442:585, 1993.

[7] M. G. Briscoe and A. A. Kovitz. Experimental and theoritical study of the stability of plane shock waves reflected normally from perturbed flat walls. *Journal of Fluid Mechanics*, 31:529–546, 1968.

[8] R.F. Chisnell. A note on Whitham's Rule. *Journal of Fluid Mechanics*, 22:103, 1965.

[9] D. Dolling. Fifty years of shock wave boundary layer interaction research: what next? *AIAA*, 39:15171531, 2001.

[10] J.L Ellzey and M.R Henneke. The interaction of a shock with a vortex : Shock distortion and the production of acoustic waves. *Physics of Fluids*, 7:172–184, 1995.

[11] A. Sakuraic F. Takayamaa, Y. Ishiib and T. Kambe. Self-intensification in shock wave and vortex interaction. *Fluid Dynamics Research*, 12.

[12] B. van Leer G. D. van Albada and Jr. W. W. Roberts. A comparative study of computational methods in cosmic gas dynamics. *Astronomy and Astrophysics*, 108:76–84, 1982.

[13] Francesco Grasso and Sergio Pirozolli. Shock-Wave-Vortex Interactions : Shock and Vortex deformation and sound production. *Theoritical and Computational Fluid Mechanics*, 13:421–456, 2000.

[14] C .Hirsch. *Computational methods for internal and external flows.* Wiley.

[15] O. Inoue and Y. Hattori. Sound generation by shock-vortex interactions. *Journal of Fluid Mechanics*, 380:81–116, 1999.

[16] Pierre-Henri Maire, Rémi Abgrall, Jérôme Breil, and Jean Ovadia. A Cell-Centered Lagrangian Scheme for Two-Dimensional Compressible Flow Problems. *SIAM J. Sci. Comput.*, 29.

[17] V. P. Maslov. Propagation of shockwaves in an isentropic non-vioscous gas. *J. Sov. Math.*, 13:119, 1980.

[18] T. Minota. Interaction of a shock wave with a high-speed vortex ring. *Fluid Dynamics Research*, 12.

[19] A. Monica and P. Prasad. Propagation of a curved weak shock. *Journal of Fluid Mechanics*, 434:119–151, 2001.

[20] K. W. Morton and P. L. Roe. Vorticity-preserving Lax-Wendroff-type schemes for the system wave equation. *SIAM J. Sci. Comput.*, 23, 2001.

[21] Hiroaki Nishikawaa and Keiichi Kitamuraa. Very simple, carbuncle-free, boundary-layer-resolving, rotated-hybrid Riemann solvers. *Journal of Computational physics*, 227:2560–2581, 2008.

[22] Sergio Pirozolli and Francesco Grasso. Direct numerical simulation of impinging shock wave/turbulent boundary layer interaction at M = 2.25. *Physics of Fluids*, 18:065113, 30 June 2006.

[23] Sergio Pirozzoli and Matteo Bernardini. Direct Numerical Simulation Database for Impinging Shock Wave/Turbulent Boundary-Layer Interaction. *AIAA*, 49.

[24] P. Prasad. *Nonlinear Hyperbolic Waves in Multi-Dimensions*. Chapman and Hall/CRC.

[25] P. Prasad. *Propagation of a Curved Shock and Nonlinear Ray Theory*. Longman.

[26] J. J. Quirk. A contribution to the great Riemann solver debate. *International Journal for Numerical Methods in Fluids*, 18.

[27] H. S. Ribner. Cylindrical sound wave generated by shock-vortex interaction. *AIAA*, 23:1708–1714, 1985.

[28] R. D. Richtmyer. A Survey of Difference Methods for Non-Steady Fluid Dynamics. *NCAR*, pages 63–2, 1962.

[29] P. L. Roe. Approximate Riemann solvers, parameter vectors, and difference schemes. *Journal of Computational physics*, 43:357–372, 1981.

[30] J.F. Debieve S. Piponniau, J.P. Dussauge and P. Dupont. A simple model for low-frequency unsteadiness in shock-induced separation. *Journal of Fluid Mechanics*, 629:87–108, 2009.

[31] D. W. Schwendeman. A new numercial method for shock wave propagation based on geometrical shock dynamics. *Proc. Roy. Soc. Lond. Ser. A*, 442:585, 1993.

[32] R. Srinivasan and P. Prasad. On the propagation of multidimensional shocks of arbitrary strength. *Proc. Indian Acad. Sci., (Math. Sci.)*, 94:27, 1985.

[33] L. Ting. Transmission of singularities through a shock wave and the sound generation. *Physics of Fluids*, 17:1518–1526, 1974.

[34] N.F. Smyth W.D. Henshaw and D.W. Schwendeman. Numerical shock propagation using geometrical shock dynamics. *Journal of Fluid Mechanics*, 171:519–545, 1986.

[35] C. E. Weatherburn. *Differential Geometry*. CUP, 1931.

[36] G.B. Whitham. *Linear and Nonlinear waves*. Wiley.

[37] G.B. Whitham. A new approach to problems of shock dynamics, Part I,Two-dimensional problems. *Journal of Fluid Mechanics*, 2:145, 1957.

[38] G.B. Whitham. A new approach to problems of shock dynamics, Part II,Three-dimensional problems. *Journal of Fluid Mechanics*, 5:369, 1959.

[39] G.B. Whitham. A note on shock dynamics in a moving medium. *Journal of Fluid Mechanics*, 31:449, 1968.

[40] M. Wu and M.P. Martin. Analysis of shock motion in shockwave and turbulent boundary layer interaction using direct numerical simulation data. *Journal of Fluid Mechanics*, 594:71–83, 2008.